Jordan Journal of Mechanical and Industrial Engineering (JJMIE)

JJMIE is a high-quality scientific journal devoted to fields of Mechanical and Industrial Engineering. It is published by The Hashemite University in corporation with the Jordanian Scientific Research Support Fund.

SUBMISSION ADDRESS:

Prof. **Mousa S. Mohsen**, Editor-in-Chief
Jordan Journal of Mechanical & Industrial Engineering,
Hashemite University,
PO Box 330127, Zarqa, 13133 , Jordan
E-mail: jjmie@hu.edu.jo

Hashemite Kingdom of Jordan

Hashemite University

Jordan Journal of Mechanical and Industrial Engineering

JJMIE

An International Peer-Reviewed Scientific Journal

http://jjmie.hu.edu.jo/

ISSN 1995-6665

Jordan Journal of Mechanical and Industrial Engineering (JJMIE)

JJMIE is a high-quality scientific journal devoted to fields of Mechanical and Industrial Engineering. It is published by The Jordanian Ministry of Higher Education and Scientific Research in corporation with the Hashemite University.

Introduction: The Editorial Board is very committed to build the Journal as one of the leading international journals in mechanical and industrial engineering sciences in the next few years. With the support of the Ministry of Higher Education and Scientific Research and Jordanian Universities, it is expected that a heavy resource to be channeled into the Journal to establish its international reputation. The Journal's reputation will be enhanced from arrangements with several organizers of international conferences in publishing selected best papers of the conference proceedings.

Aims and Scope: Jordan Journal of Mechanical and Industrial Engineering (JJMIE) is a refereed international journal to be of interest and use to all those concerned with research in various fields of, or closely related to, mechanical and industrial engineering disciplines. Jordan Journal of Mechanical and Industrial Engineering aims to provide a highly readable and valuable addition to the literature which will serve as an indispensable reference tool for years to come. The coverage of the journal includes all new theoretical and experimental findings in the fields of mechanical and industrial engineering or any closely related fields. The journal also encourages the submission of critical review articles covering advances in recent research of such fields as well as technical notes.

Guide for Authors

Manuscript Submission

High-quality submissions to this new journal are welcome now and manuscripts may be either submitted online or mail.

Online: For online submission upload one copy of the full paper including graphics and all figures at the online submission site, accessed via E-mail: jjmie@hu.edu.jo. The manuscript must be written in MS Word Format. All correspondence, including notification of the Editor's decision and requests for revision, takes place by e-mail and via the Author's homepage, removing the need for a hard-copy paper trail.

By Mail: Manuscripts (1 original and 3 copies) accompanied by a covering letter may be sent to the Editor-in-Chief. However, a copy of the original manuscript, including original figures, and the electronic files should be sent to the Editor-in-Chief. Authors should also submit electronic files on disk (one disk for text material and a separate disk for graphics), retaining a backup copy for reference and safety.

Note that contributions may be either submitted online or sent by mail. Please do NOT submit via both routes. This will cause confusion and may lead to delay in article publication. Online submission is preferred.

Submission address and contact:

Prof. **Mousa S. Mohsen**, Editor-in-Chief
Jordan Journal of Mechanical & Industrial Engineering,
Hashemite University,
PO Box 330127, Zarqa, 13115 , Jordan
E-mail: jjmie@hu.edu.jo

Types of contributions: Original research papers

Corresponding author: Clearly indicate who is responsible for correspondence at all stages of refereeing and publication, including post-publication. Ensure that telephone and fax numbers (with country and area code) are provided in addition to the e-mail address and the complete postal address. Full postal addresses must be given for all co-authors.

Original material: Submission of an article implies that the work described has not been published previously (except in the form of an abstract or as part of a published lecture or academic thesis), that it is not under consideration for publication elsewhere, that its publication is approved by all authors and that, if accepted, it will not be published elsewhere in the same form, in English or in any other language, without the written consent of the Publisher. Authors found to be deliberately contravening the submission guidelines on originality and exclusivity shall not be considered for future publication in this journal.

Supplying Final Accepted Text on Disk: If online submission is not possible: Once the paper has been accepted by the editor, an electronic version of the text should be submitted together with the final hardcopy of the manuscript. The electronic version must match the hardcopy exactly. We accept MS Word format only. Always keep a backup copy of the electronic file for reference and safety. Label the disk with your name. Electronic files can be stored on CD.

Notification: Authors will be notified of the acceptance of their paper by the editor. The Publisher will also send a notification of receipt of the paper in production.

Copyright: All authors must sign the Transfer of Copyright agreement before the article can be published. This transfer agreement enables Jordan Journal of Mechanical and Industrial Engineering to protect the copyrighted material for the authors, but does not relinquish the authors' proprietary rights. The copyright transfer covers the exclusive rights to reproduce and distribute the article, including reprints, photographic reproductions, microfilm or any other reproductions of similar nature and translations.

PDF Proofs: One set of page proofs in PDF format will be sent by e-mail to the corresponding author, to be checked for typesetting/editing. The corrections should be returned within 48 hours. No changes in, or additions to, the accepted (and subsequently edited) manuscript will be allowed at this stage. Proofreading is solely the author's responsibility. Any queries should be answered in full. Please correct factual errors only, or errors introduced by typesetting. Please note that once your paper has been proofed we publish the identical paper online as in print.

Author Benefits

Page charge: Publication in this journal is free of charge.

Free off-prints: Three journal issues of which the article appears in along with twenty-five off-prints will be supplied free of charge to the corresponding author. Corresponding authors will be given the choice to buy extra off-prints before printing of the article.

Manuscript Preparation:

General: Editors reserve the right to adjust style to certain standards of uniformity. Original manuscripts are discarded after publication unless the Publisher is asked to return original material after use. If online submission is not possible, an electronic copy of the manuscript on disk should accompany the final accepted hardcopy version. Please use MS Word for the text of your manuscript.

Structure: Follow this order when typing manuscripts: Title, Authors, Affiliations, Abstract, Keywords, Introduction, Main text, Conclusions, Acknowledgements, Appendix, References, Figure Captions, Figures and then Tables. For submission in hardcopy, do not import figures into the text - see Illustrations. For online submission, please supply figures imported into the text AND also separately as original graphics files. Collate acknowledgements in a separate section at the end of the article and do not include them on the title page, as a footnote to the title or otherwise.

Text Layout: Use double spacing and wide (3 cm) margins. Ensure that each new paragraph is clearly indicated. Present tables and figure legends on separate pages at the end of the manuscript. If possible, consult a recent issue of the journal to become familiar with layout and conventions. All footnotes (except for table and corresponding author footnotes) should be identified with superscript Arabic numbers. To conserve space, authors are requested to mark the less important parts of the paper (such as records of experimental results) for printing in smaller type. For long papers (more that 4000 words) sections which could be deleted without destroying either the sense or the continuity of the paper should be indicated as a guide for the editor. Nomenclature should conform to that most frequently used in the scientific field concerned. Number all pages consecutively; use 12 or 10 pt font size and standard fonts. If submitting in hardcopy, print the entire manuscript on one side of the paper only.

Corresponding author: Clearly indicate who is responsible for correspondence at all stages of refereeing and publication, including post-publication. The corresponding author should be identified with an asterisk and footnote. Ensure that telephone and fax numbers (with country and area code) are provided in addition to the e-mail address and the complete postal address. Full postal addresses must be given for all co-authors. Please consult a recent journal paper for style if possible.

Abstract: A self-contained abstract outlining in a single paragraph the aims, scope and conclusions of the paper must be supplied.

Keywords: Immediately after the abstract, provide a maximum of six keywords (avoid, for example, 'and', 'of'). Be sparing with abbreviations: only abbreviations firmly established in the field may be eligible.

Symbols: All Greek letters and unusual symbols should be identified by name in the margin, the first time they are used.

Units: Follow internationally accepted rules and conventions: use the international system of units (SI). If other quantities are mentioned, give their equivalent in SI.

Maths: Number consecutively any equations that have to be displayed separately from the text (if referred to explicitly in the text).

References: All publications cited in the text should be presented in a list of references following the text of the manuscript.

Text: Indicate references by number(s) in square brackets in line with the text. The actual authors can be referred to, but the reference number(s) must always be given.

List: Number the references (numbers in square brackets) in the list in the order in which they appear in the text.

Examples:

Reference to a journal publication:

[1] M.S. Mohsen, B.A. Akash, "Evaluation of domestic solar water heating system in Jordan using analytic hierarchy process". Energy Conversion & Management, Vol. 38, No. 9, 1997, 1815-1822.

Reference to a book:

[2] Strunk Jr W, White EB. The elements of style. 3rd ed. New York: Macmillan; 1979.

Reference to a conference proceeding:

[3] B. Akash, S. Odeh, S. Nijmeh, "Modeling of solar-assisted double-tube evaporator heat pump system under local climate conditions". 5th Jordanian International Mechanical Engineering Conference, Amman, Jordan, 2004.

Reference to a chapter in an edited book:

[4] Mettam GR, Adams LB. How to prepare an electronic version of your article. In: Jones BS, Smith RZ, editors. Introduction to the electronic age, New York: E-Publishing Inc; 1999, p. 281-304

Free Online Color: If, together with your accepted article, you submit usable color and black/white figures then the journal will ensure that these figures will appear in color on the journal website electronic version.

Tables: Tables should be numbered consecutively and given suitable captions and each table should begin on a new page. No vertical rules should be used. Tables should not unnecessarily duplicate results presented elsewhere in the manuscript (for example, in graphs). Footnotes to tables should be typed below the table and should be referred to by superscript lowercase letters.

JJMIE

Volume 6, Number 2, April 2012
ISSN 1995-6665

Jordan Journal of Mechanical and Industrial Engineering

PAGES	PAPERS

JJMIE

Volume 6, Number 2, April 2012
ISSN 1995-6665
Pages 110 - 118

Jordan Journal of Mechanical and Industrial Engineering

Prospects and Challenges of Small Hydropower Development in Jordan

J.O. Jaber[a,]*

[a]Faculty of Engineering Technology, Al-Balqa' Applied University, Amman, Jordan

Abstract

Jordan's energy balance is largely dominated by combustible fuels. However, the country is well endowed with solar, wind and oil shale resources, in addition to large and small-scale hydropower projects. Based on available data and the current analysis, it is believed that there are at least 6-10 candidate sites in the western part of Jordan and 2-3 locations in the eastern plateau, which could be developed as small hydro plants, with a combined potential of more than 33 MW. At present, only two sites, namely King Talal Dam and Aqaba Thermal Power Plant, have been developed to be operational from 1980's. A major barrier to starting small scale hydro power projects is an understanding of how much the scheme will cost. This paper provides also an overview of the setbacks that inhibit the smooth investment and operation of small hydropower plants in Jordan. It is estimated that installing small hydropower schemes on the most promising existing dams will generate more than 200 GWh/year of electric energy without effecting the natural environment. In addition, there are another few sites, still under study, that may be developed in the future as small hydro plants.

Keywords: Small hydropower; Pumped storage; Power generation; Renewable energy; GHG emission; Jordan

1. The Problem

Despite being adjacent to oil-rich countries, Jordan has no significant fossil resources of its own. In 2010, Jordan produced 136.4 thousand tons of oil equivalent (ktoe) of natural gas and 1.2 ktoe of crude oil, while it consumed 3,440.7 ktoe of crude oil and 2,288.7 ktoe of natural gas, which clearly illustrates that Jordan is heavily dependent on oil imports to fulfill its domestic energy needs in the transport, industrial, domestic heating, and power sectors [1]. The 2003 Iraq invasion disrupted Jordan's primary oil supply route from its eastern neighbor, which prior to the war provided the Kingdom with highly discounted crude oil via the road truck route. Since late 2003, an alternative supply from the regional market at international prices has been established; Saudi Arabia is now Jordan's primary source of imported oil, with Kuwait and the United Arab Emirates following. The completion of the first phase of the Arab Gas Pipeline in 2003 was an important milestone in reducing dependence on refined products and crude oil, allowing Egyptian natural gas to reach various power plants in Jordan, thereby reducing the local cost of power production [2]. However, and after the recent political developments in Egypt, there were several cuts and major shortages in gas supplies due to terrorist attacks against the main pipeline in the Sinai Peninsula. Supply has been cut for more than 120 days during the last year, and total gas quantities received by Jordan were less than 20% of that agreed upon [3]. But the Egyptian government agreed to substitute for the lost quantities of natural gas over a period of three years starting from 2013 depending on the technical situation at their side. However, the Government of Egypt insisted on amending the favorable pricing agreement between the two countries under which Jordan received natural gas for less than half the international market price. During the past 2-3 years, the national power generation level was critical, and sometimes felled short behind the national demand, especially during the summer season [4]. In the near future, Jordan will remain a net importer of oil and natural gas from the Arab neighboring countries, especially Saudi Arabia and Kuwait as well as electricity from Egypt, to meet peak-load and sometimes part of base-load. Thus, the current situation presents an ideal environment for development of renewables including hydropower sources, particularly small hydropower (SHP) sources whose financial and technical demands can be met by small investors from within or without the country with relative ease.

The Government of Jordan plans to promote the continued development of the country's overall energy sector to best enable it to accommodate changing market conditions, and in particular, the rapidly growing local demand for electricity and refined petroleum products. One of the primary objectives of Jordan's Energy Master Plan is to further increase private sector investment in the development of the energy sector over the next 20 years [5]. The plan was approved by the Council of Ministers in December 2004, and its 2007 updated version calls for an estimated investment of US$ 13 to 17 billion from 2007 to 2020, which would be financed by the private sector across

* Corresponding author. e-mail: jojaber@gmail.com

the downstream, electricity, natural gas, oil shale, and renewable energy. Implementation of the plan is expected to stimulate further growth in the Jordanian economy and will create a number of investment opportunities which will be structured to encourage and promote private sector participation. The plan aims to reduce the reliance on imported products from the current level of approximately 96%, with a goal for renewable energy meeting 10% of energy demand by 2020 and nuclear energy providing a significant portion of new electricity capacity by 2035. It also addresses the required investment cost from the private sector and reforms needed within the energy sector for improved market competition. As a part of this plan, Temporary Law #3 of 2010, The Renewable Energy and Energy Efficiency Law (REEL), was released in early 2010 to define Jordan's plans to introduce renewable energy generation to the local sector [6]. Primary objectives of the REEL include: (i) increasing the contribution of renewable energy to the total energy mix in Jordan; and (ii) promoting and exploiting renewable energy for environmental protection and sustainable development purposes. Rules and regulations to guide implementation of the REEL are still under development. The Government of Jordan, with the assistance of donors such as USAID, USTDA, and the World Bank, is currently in the process of further defining the required regulation and technical considerations, and is identifying potential funding sources to enable the development of these assets.

The electricity demand of in Jordan is growing rapidly at high rates, of about 7% during the last two decades, and expected to continue in the near future since the social and economic structure is still developing. Several attempts have been made by the consecutive governments to enhance the utilization of indigenous natural sources and to promote the utilization of renewable energy resources, including hydro power, in order to increase electricity production, which will help decreasing dependence on foreign energy supplies. Recently the Government of Jordan through the Ministry of Energy and Mineral Resources (MEMR) announced for interested investors in renewable energy power generation projects to submit an expression of interest before July 28, 2011, on the basis of build, own and operate (BOO). Investors were invited to express interest in developing only one type of renewable energy source and technology in this round. Received proposals were evaluated in late April 2012 and 34 companies selected as qualified investors based on financial position and experience in raising sufficient debt participation and substantial equity participation for power projects, technical capability and past experience in similar projects. MEMR is in the process of preparing memorandum of understanding (MOU) with these companies on individual basis to conduct the needed detailed feasibility studies and submit proposals, including the financial terms, to MEMR within next 24-36 months [7].

Jordan will face major challenges in trying to meet the growing energy and especially electricity, while, concurrently, developing the energy sector in a way that ensures reducing the adverse impacts on the economy, the environment and social life. Fast depleting fossils fuels and their environmental effects forces to look towards renewable sources for sustainable development. Among all renewable sources, SHP is one of the promising sources for sustainable water and energy development. The geography of Jordan supports the development of small hydro plants to enhance power generation from renewable sources. SHP development is also necessary for proper utilization of available limited water resources. The present study has been carried out as a preliminary attempt to highlight the potential of SHP plants in Jordan.

This paper is structured as follows: section 2 introduces the basic concept and technology of SHP; section 3 serves as background and reviews SHP systems. In section 4, the adopted methodology is presented and basic assumptions employed in the current investigation. A detailed argument of the potential of SHP plants and estimated installed power for most promising sites are discussed in section 5, while the following section 6 concludes main findings of his study.

2. What is Small Hydropower?

Small hydropower is a key element for sustainable development due to the following reasons [8-11]:

- SHP is a renewable source of energy: small hydropower meets the definition of renewable because it uses the energy of flowing water repeatedly generates electricity without fear of depletion.
- SHP is a cost effective and sustainable source of energy: simple and less expensive construction work and in expensive equipment are required to establish and operate small hydropower projects. The cost of electricity generation is inflation free. Also, the gestation period is short and the schemes give financial returns quickly.
- Proper utilization of water resources: various streams and rivers can safely provide energy to run a small hydro electric plant. No big water storage is required in such projects which prevents resettlement and rehabilitation of the population.
- SHP aids in conserving scarce fossil fuels: no fossil fuels and other petroleum products are required in small hydro electric project. SHP replaces the fossil-fired generation of electricity.
- Clean and non-polluting source: SHP projects are known for low carbon energy production. Small hydro is a pollution free source for electricity generation and environmental problems like GHG emissions, acid rain are not associated with it. The development of small hydro has low effect on the environment. In SHP, no big storage is formed and rehabilitation of population is not required as in case of large hydropower projects.
- Development of rural and remote areas: in remote and hilly areas, sources for development of small hydro are found in abundance. SHP development provides electricity, transportation, communication links and economy to such rural areas.
- Other uses: SHP also gives additional benefits along with power generation such as irrigation, water supply, flood prevention, fisheries and tourism.

In general, SHP schemes are classified into two main types: (i) utilizing small discharges but high heads, and (ii) utilizing large discharges but low heads. Such features have strong influence on the nature of the power station for a specific site. In high head units the discharges being small, the physical size of the plant required is also small. In the second type, as the flow rates are relatively high, the size of the generating unit and the power station is consequently quite big. Also for the latter type, proper arrangements for entry of water and its discharge are required to be made. The SHP development of the first type is usually used in mountainous regions and characterized by relatively very simple features. The civil works involved comprise a small structure to divert the flow of the water stream/river, and generally the 'run of river' water-falls is utilized. The power is generally consumed near the site of generation, but could be connected to a transmission network. In the second type, as the heads available are rather low and discharges have to be comparatively larger to be economically viable, their development can only take place on small rivers, irrigation outlets, canal falls, etc., and the power output is generally connected to the national grid via a transmission line. Another scheme that could be included here is the pumped storage, which aims to store electric energy in the form of hydraulic potential energy. Pumping typically takes place mainly during off-peak periods, when electricity demand is low and electricity prices are low. Generation takes place during peak periods, when electricity system demand is high. Pumping and generating generally follow a daily cycle but weekly or even seasonal cycling is also possible with larger plants. The benefits of such schemes to the electrical system operations are well documented in textbooks and journals [12-16]. Its flexible generation can provide both up and down regulation in the power system while its quick start capabilities make it suitable for black starts and provision of spinning and standing reserve. In terms of operational characteristics and flexibility, a gas turbine peaking plant such as open cycle gas turbine offer some similar power system operation services, but at a higher capital cost [17].

As the name implies, SHP is a smaller version of the large hydro schemes. In the open literature, there is no internationally accepted formal definition of small hydro in place as yet, though it is generally taken as a power plant having an average output of about 25 MW or less [8]. Different agencies use different upper limits for micro and mini hydro projects ranging from 0.1 MW to 2 MW for the micro and >2 MW to 50 MW for mini hydro. However, it looks that a ceiling value of 10 MW, which could be sufficient to power 10 thousand houses, or 50-60 thousand inhabitants and a community centre, based on average of 1 kW per house and a typical diversity factor, is becoming more generally accepted for mini hydro projects, especially in the European countries, i.e. The European Small Hydropower Association (ESHA). At the lower end of the scale, technology is available to utilize discharges as small as 200 l/s, heads down to 1 m, and a power output of just 0.001kW with reasonable cost. Some researchers classify very small (<5kW) units as 'pica-hydro'. According to the Indian Ministry of New and Renewable Energy (MNRE), small hydropower stations are classified as shown in Table 1: Similar classification is adopted in the UK and other countries [8,18-20]

The hydro turbines convert water pressure into mechanical shaft power that can be used to drive an electric generator. The power available is proportional to the product of head and flow rate. In a typical SHP scheme, water is taken from the stream/river by diverting it through an intake weir. The weir is a man made structure constructed across the water stream/river, which maintains a continuous flow through the intake. The water passes through a desilting tank in which the water is slowed down sufficiently for suspended particles to settle down before descending to the turbine. In medium or high-head installations, water is carried to the forebay by a canal. In low-head installations, generally, water entering the turbine directly from the weir. A pressure pipe, known as a penstock, conveys the water from the forebay to the turbine. All installations need to have a valve or gate at the top of the penstock to control the flow. The hydraulic efficiency of water turbines is high with an average of about 90% [21-23].

Table 1: Classification of small hydro power plants according to capacity & head.

Capacity (kW)	Head (m)
Micro, up to 100	Ultra low, less than 3
Mini, between 101 and 1000	Low, more than 3 up to 40
Small, more than 1000 up to 25000	Medium/high, more than 40

3. Background

Initially, hydropower was specifically used in water wheels for lifting water up from the water source, e.g. river, to a water supply network, irrigation, mills and other mechanical applications. But during the last century it became an efficient source for power generation, and the development of hydropower was usually associated with building large dams. Large number of massive barriers of concrete, rock and earth were placed across river valleys, world-wide, to create huge manmade water reservoirs. While these created a steady power supply in addition to irrigation and flood control benefits. But dams, in most cases, flooded large areas of fertile land and displaced millions of local inhabitants. In many cases rapid silting up of the dam has reduced its productivity and lifetime. There are also numerous environmental problems that can result from such major interference with stream/river flows. However, at present the exploitation of large hydro sources is mainly saturated, especially in developed countries. Further construction of large hydropower plants is often burdened with the unacceptable high investments, and/or undesirable environmental consequences. Hence, in recent years, a wide interest and activity is directed towards the utilization of energy potentials of small streams, and building SHP plants, as well as towards other natural hydropower sources, such as sea waves [24].

The small hydro energy generation is environment friendly and it is very useful for generating electricity in rural and urban areas: it is certainly the most mature application of renewable technologies. Approximately 22% of the world's power generation comes from hydropower installations, many of which are SHP plants

[25]. There is no international consensus on the definition of small hydropower. However, a capacity of up to 10 MW total is becoming the generally accepted norm in different countries [12-15]. SHP plants have found an extensive application in electricity production both in EU, USA and other countries, and deserve a special attention regarding its huge economically feasible potential. Such resource has been harnessed for more than 100 years in most of EU countries. China and India also achieved a considerable success in SHP development [8-11,26]. In China, which is the leading country worldwide in terms using SHP units, about 19 thousand micro-hydropower plants with a total installed capacity of 687 MW and a slightly higher similar number of mini-hydropower plants with a total installed capacity of 7171 MW were constructed between 1994 and 2004 [11]. Moreover, small hydropower could be harnessed at several hydraulic structures where power generation is not the main aim of the use of water [27]. These hydraulic structures are: water supply dams, irrigation canals, wastewater treatment plants, weirs, and water cooling systems in thermal power plants. For example, In Switzerland, 80 SHP plants were installed on the municipal water supply systems of the country [28]. The advantages of these systems compared to a stream/river-type hydropower plants could be summarized as follows: (i) all civil works are present which will reduce the investment cost 50%, (ii) it has a capacity factor about 85% which provides two times higher annual energy with the same installed capacity of a stream/river-type hydropower plant (iii) the generated electricity will be used in the water treatment plant and the excess electricity will be sold to the grid, (iv) there is no land acquisition and operating cost.

Within the region Turkey and Iran have good potential of hydropower. In Turkey the estimated total hydropower potential is about 433 TWh that accounts for almost 1.1% of the total hydropower potential of the world and approximately 14% of the European hydropower potential. But only 130 TWh of the total hydroelectric potential of Turkey can be used economically. In 2007 almost 18% of total annual electricity production in Turkey, which is equal to 35TWh/yr, i.e. about 27% of economical hydropower potential, was provided by hydropower plants. By the commissioning of new hydropower plants, which are under construction, 43% of the economically usable potential of the country would be exploited [20,29]. Recently the Iranian government embarked upon a joint venture with the Chinese government for establishing micro hydro plants, a number of which are at present operating at different points of the country and work is still going on to install more SHP units [30].

Although it is reported in the open literature that Asia leads the world as the biggest small hydropower generating continent, still the gap is large between available resources and the existing SHP projects. For example, India has SHP of about 15,000 MW, which is considered only a tenth of it has been tapped so far. Indonesia has an estimated SHP of 500 MW but only 5 MW has been installed and just 1 MW is being actually used. Bangladesh has a SHP of close to 10,000 MW but almost zero utilization. Other countries, including the world's fastest growing economics, India and Brazil, are putting in place increasingly ambitious plans to tap their SHP. Alongside wind energy, SHP is the fastest growing renewable energy option for electricity supplies in Canada. The European Union's new member states have only about a tenth of small hydro capacity compared to the old EU-15 nations, but plans are afoot to increase it substantially [8,9,11,18,20].

The increase in prices of fossil fuels and their impact on the environment has made hydropower a more important and attractive energy source. Of all the renewable sources of energy, water seems the best choice, and small hydropower development seems the most cost-effective and reliable energy technology to be considered for providing clean electricity generation. In particular, the key advantages that small hydro has over other renewable sources, such as wind, biomass and solar power are:

- High efficiency of between 70 and 90 %, by far the best of all energy technologies.
- High capacity factor of about 50 %, compared with 10% for solar and 30% for wind.
- High level of predictability, varying with annual rainfall patterns.
- Slow rate of change; the output power varies only gradually from day to day, but not from second to second.
- It is a long-lasting and robust technology; systems can readily be engineered to last for 50 years or more.
- It can be integrated with fishing, drinking and irrigation water projects, in order to share the costs between different beneficiaries.

Jordan has some good geographical locations with small and big potential of water resources, but small hydro development is an important step for conservation of water resources and sustainable development in the country. The possibilities and scope of enhancement of SHP in Jordan was attempted to explore in the present study. This article introduces the potential of hydropower in Jordan from the following aspects: potential, economy, environment and society as well as assesses their existing problems, and then demonstrates that Jordan must accelerate the development of such resources and other renewable projects in order to realize the sustainable development of economy, environment and society.

4. Methodology

The traditional approach in electric power generation is to have centralized plants distributing electricity through an extensive transmission and distribution networks. Distributed generation provides electric power at a site closer to the customer, eliminating the unnecessary transmission and distribution losses and costs. In addition, it can reduce emissions resulting from fossil fuel combustion, defer capital cost, and reduce maintenance and investments. The decision to develop a hydropower project is usually made on economic grounds, but other factors such as environmental, cultural and physical characteristics of the site and the costs and availability of technological and engineering solutions are also important. While the capital costs of a hydro plant installation is high, operating and maintenance costs are low, which means that a large proportion of the project's overall budget will be spent at the development stage. It is therefore important to balance the cost installation against the magnitude and speed of energy output (and its value) to evaluate whether the project is worth pursuing, and if so, to plan the subsequent budget. The viability of each hydro project is site-specific and dependent on the local characteristics. The amount of the power produced depends on water flow, hydraulic head and the efficiency of the employed device, but it should be remembered that the flow will vary through the year and hence the generated power and efficiency will change in response to this variation.

In this work, a preliminary analysis of the potential sites was undertaken for the western highland region in Jordan, including site visits, scheme layouts, and scheme costing as well as economic evaluation. Based on limited data for the studied sites, a flow duration curve was produced for each site using a tailor made computer program, specially developed for this purpose. After the average flow and head were estimated, then the scheme capacity, for each site, was projected. The capacity (power, kW) is computed using the following basic model.

$$\text{Power (kW)} = \eta_t \rho_w g Q h \eta_g \quad (1)$$

ηt the hydraulic efficiency of the turbine (%)
γw the specific weight of water (9.81 kN/m^3)
Q the discharge rate (m3/s)
H the head of water acting on the turbine (m)
ηg the efficiency of the electric generator (%)

The annual power generation E (kWh/year) of a hydropower plant is obtained from

$$E = P t \quad (2)$$

t is the operation of hours through a year

The design head of the power plant was selected as the average water level of the reservoir for a specific site. The actual electric energy generation cost is about 0.15 US $/kWh in Jordan for the year 2011; this value was used in determining the economic benefit of the hydropower plant [7]. Several studies have been carried out to analyze the costs of hydro plant development depending on the hydraulic characteristics of a given site. Due to diversification in layout/configuration of SHP plants, a number of cost equations were developed to suit the site conditions. It was found that number of contributions exists for determining the installation cost using the head and capacity as cost influencing parameter. Similarly different optimization approaches have been used and implemented to obtain the optimum investment required for installation of the plant [31-34]. It is observed that for the optimization of investment, different methods have been used carried out simple techniques; however it is recommended to use evolutionary algorithm and other new techniques for the optimization of investment. But in this study, the relationship between the overall costs of the SHP project and the hydraulic characteristics of a site is given by the following empirical models [34]:

For heads between 2-30 m

$$C\ (US\$) = 37{,}500\ (kW/h^{0.35})^{0.65} \quad (3)$$

and for heads between 30-200 m

$$C\ (US\$) = 67{,}000\ (kW/h^{0.30})^{0.60} \quad (4)$$

It is worth mentioning here that no high heads, e. g. waterfalls, are available in Jordan, and thus the empirical for high heads, Equation 4, will not be used in the current study. A computer based costing package was developed and used to estimate the capacity, annual power generation, avoided GHG emissions and total cost of each scheme excluding the transmission cost for each of the studied sites, in Jordan. The basic assumptions employed in this investigation are (i) average operating time 6000 hrs/yr, (ii) average hydraulic head for all existing dams will be taken as 15 m, and about 10 m for the proposed new dams, and (iii) turbine hydraulic efficiency is 80 %, regardless of the type of turbine, and electric generator efficiency is 90 %.

As stated previously energy and development are closely intertwined and increasing fossil fuel-based power generation contributes significantly to environmental problems on national and international levels. The power sub-sector, in Jordan, is facing problems of high electricity demand as well as regulation on gaseous emissions, in addition to security of fuel supplies, especially the imported natural gas from Egypt. Thus, it is crucial to find sustainable generation methods with high efficiency and availability. Following this criteria there are few possibilities of power generation, in Jordan, such as solar, wind, small hydropower and oil shale based power plants. Hydropower schemes can contribute with a cheap source, as well as to encourage the development of small industries across a wide range of new technologies. The energy of flowing water is a renewable and clean source of electricity. SHP systems allow achieving self-sufficiency by using the best possible scarce natural resource that is the water, as a decentralized and low-cost of energy production. In this paper the prospects of SHP, in Jordan, are presented and evaluated.

5. Potential of Small Hydro in Jordan

In Jordan, hydropower sources are limited due to the fact that the surface water resources, such as rivers and falls, are almost negligible. However, currently there are two SHP schemes. The first one is King Talal dam spanning the river Zarqa, with a rated electricity-generating capacity of about 5 MW. The other scheme is at the Aqaba thermal power station, where the hydro-turbine utilizing the available head of returning cooling seawater with a capacity of 5 MW [35]. The total amount of electricity generated, in 2010, by hydro-units was about 61 GWh, i.e. less than 0.5% of the total national electricity generation [36]. Such low ratio of utilization could be attributed to many reasons, but the most important being lacks both financial and technical capacity to develop its own conventional hydroelectricity potential. However, there is a great possibility to generate electricity, using hydropower stations, by exploiting the elevation difference between the Red and Dead Seas. The latter is the lowest region on earth with water-surface of 400 m below normal sea level. If seawater is allowed to follow from the Gulf of Aqaba into the Dead Sea through a canal/pipeline system at predetermined rates, it will produce electricity from hydropower stations and potable water from seawater desalination plants. While, this project is expected to help in establishing new economic activities, such as tourism and agriculture, it ensures supply of large amounts of highly needed electricity and water as well as the renewal of the Dead Sea water by making up the evaporated water. The latter will dictate the amount of electricity generated annually. Preliminary pre-feasibility reports showed that it is possible to build hydropower stations with a total capacity of about 800 MW, or more [37]. But the required capital investment is extremely high due to the long canal, i.e. about 200 km, and necessary infrastructure.

The work in the current study is focused in the western region, i.e. mountains region, of Jordan, where almost all water sources and/or collection systems are located. Both of the Ministry of Energy and Mineral Resources and Ministry of Water and Irrigation should strongly believe that mini-hydro or pumped storage plants and related facilities are considered as energy projects. But there are other important dimensions such as improved agriculture, cultivation, water harvesting and irrigation as well as tourism and recreation activities in the developed areas which would benefit from the additional power generation. Table 2 below summarizes capacities of existing dams, while Table 3 provide the same information for the proposed dams which are under study till now. As can be seen in Table 3 that only the hydro potential of one dam, i.e. King Talal, has been utilized to generate electricity with a rated capacity of 5 MW. It is considered as a SHP scheme.

Table 2: Average flows of existing main dams in Jordan [38].

Name / Location	Average Annual Flow (10^6 m^3/yr)		Hydropower Utilization	
	In	Out	Yes	No
Al Wahdah / Irbid	13.0	5.0		x
Al Arab / Nothern Shuonah	10.0	11.5		x
Sharhabiel / Northern Jordan Valley	5.1	5.8		x
King Talal / Jerash	92.2	92.3	x	
Wadi Shuiaib / Southern Shounah	6.1	6.3		x
Kafrain / Southern Shounah	11.3	11.3		x
Karameh / Southern Shounah	2.1	0.5		x
Tanoor / Jordan Valley	4.1	1.3		x
Waleh / Madaba	6.6	8.7		x
Mojeb / Karak	3.o	16.0		x

At present, all other existing dams are being utilized as storage reservoirs to meet water demand during the long dry summer season. But almost all of these sites are suitable to be upgraded as SHP and/or pumped storage schemes since they are located in hilly areas in the western part of the country, where annual precipitation exceeds 400 mm and may reach 600 mm with some snow in some areas. Evaluating the case of a pumped storage system for each site is very difficult at this stage, since its features and characteristics are site specific, e.g. topography, average annual flow, etc., for each site. Thus, it would be impossible in this study to assess the potential of such schemes, in Jordan, and it is recommended that future work should investigate such possibility and address the feasibility of pumped storage systems as part of the energy management plan in the country. The proposed small dams, under study by the Ministry of Water and Irrigation, listed in Table 3, may represent an opportunity for implementing SHP systems. However, most of these sites are not developed yet, and would take long leading time before seeing the light.

Table 3: Storage capacity for the proposed small dams in Jordan [38].

Name / Location	Proposed Storage Capacity (10^6 m^3)	Status as of Early 2010
Maa'in / Madaba	1.0	Under study
Lajjun / Karak	1.0	Under study
Dalaghah / Tafila	1.0	Under study
Shuthim / Tafila	1.0	Under study
Kufranjah / Ajlun	9.0	Under study
Bin Hammad	5.0	Under study
Wahidi / Maa'n	1.8	Under study
Wadi Karak / Karak	2.1	Updating studies
Bayer / Eastern desert	4.0	Completed
Jafer / Southern desert	0.5	Under construction
Rukban / North eastern desert	2.0	Completed
Khanasree / Mafraq	1.0	Under construction
Ghadaf / Central desert	0.5	Completed

The flows of main small rivers and streams, in Jordan, that may have good potential in terms of hydropower generation are shown in Table 4. These small streams could be developed in the future as SHP projects. However, the final selection of the most promising sites requires detailed and careful assessment for all of the proposed sites before the final decision of developing any of these sites. It should be stressed here that it is not the aim of this paper to design SHP schemes in Jordan; rather it provides a preliminary assessment of the potential for hydropower generation in the studied sites. All of the reported sites are located in rural areas, and thus SHP projects are an ideal energy option for these areas because of its low operational, maintenance and repair costs. Even though the cost per unit electricity from standalone hydropower plants may be higher than that from the national grid, they present a category of energy which could substantially contribute to poverty reduction in rural households. Furthermore, small hydropower development could offer a leading renewable alternative for meeting electricity demand in remote and mountainous parts of Jordan. The advantages and attractiveness of these small hydropower plants are that they can either be stand-alone or in a hybrid combination with other renewable energy sources, such as solar and/or wind farms. The latter, could be integrated with existing dams to form a pumped storage scheme. Further, advantage can be derived from association with other uses of water, e.g. water supply, irrigation, flood control, etc., which are critical to the future economic and socio-economic development of Jordan. SHP plants are not generally affected by the constraints associated with large hydro projects: they are more environmentally and ecologically acceptable. Large scale hydropower development is becoming a challenge due to environmental and socio-economic concerns, and more recently its vulnerability to changing climates. In addition, investment in large hydroelectricity generation requires substantial upfront investment capital.

Table 4: Average annual flow of main small streams in Jordan [38].

Name / Location	Average Annual Flow Rate (10^6 m^3)
Yarmook / Irbid	32
Mukhaibah / Northern Shounah	32
Zeqlab / Northern Shounah	5
Kufranjah / Ajlun	4
Zerqa / Jerash	82
Wadi Shuiaib / Southern Shounah	6
Wadi Kafrain / Southern Shounah	11
Hussban / Amman	1
Northern Wadis / Northern desert	2
Wadi Hassa / Tafila	25
Wadi Viva / Southern Jordan Valley	4
Wadi Khanzereh / Irbid	2
Bin Hmmad / Karak	8
Wadi Karak / Karak	3
Wadi Thera' / Karak	2

Worldwide, hydropower is still the most efficient way to generate electricity. Modern hydro turbines can convert as much as 90 % of the available energy into electricity while the efficiency of the best fossil fuel plant is only about 50 %, or even less. Additionally, hydropower is an outstanding source to generate electricity in all over the world and will seemingly keep on growing especially in the developing countries. The calculated hydropower potential for the existing small dams and the proposed ones is shown in Tables 5 and 6, respectively. The total potential for the first group is around 33 MW and the annual electricity production may reach 200 GWh, i.e. approximately 1.5 % of the national electricity generation in the year 2010. While the total potential of the second group is much less and estimated at only about 14 MW with possible annual electricity production of about 90 GWh. The annual income due to sales of electrical power would yield US$ 20-30 million and approximately US$ 9-13 million, following the agreed upon feed-in-tariff of between US$ 0.1-0.15 per kWh generated, for the existing and proposed dams, respectively. The expected required investment is relatively high and varies between 1,500 and 2,500 US$ per kW installed, or more in certain cases depending on the specific site. This is considered a high investment when compared with only about 1000 US$ per kW for conventional systems. This is considered as the main obstacle for harnessing the potential of SHP in Jordan. Equally important is the lack of awareness and well to develop such resources among different stakeholders, especially the concerned governmental institutions.

Table 5: Estimated hydropower generation for existing dams.

Name / Location	Estimated Hydropower Potential (kW)	Projected Energy Generation Potential (MWh/yr)
Al Wahdah / Irbid	2,500	15,000
Al Arab / Nothern Shuonah	5,750	34,500
Sharhabiel / Jordan Valley	2,900	17,400
Wadi Shuiaib / Southern Shounah	3,150	18,900
Kafrain / Southern Shounah	5,650	33,900
Karameh / Southern Shounah	250	1,500
Tanoor / Jordan Valley	650	3,900
Waleh / Madaba	4,350	2,6100
Mojeb / Karak	8,000	48,000

Table 6: Projected potential of hydropower generation for proposed dams.

Name / Location	Estimated Hydropower Potential (kW)	Projected Energy Generation Potential (MWh/yr)
Maa'in / Madaba	500	3000
Lajjun / Karak	500	3000
Dalaghah / Tafila	500	3000
Shuthim / Tafila	500	3000
Kufranjah / Ajlun	4500	27000
Bin Hammad	2500	15000
Wahidi / Maa'n	900	5400
Wadi Karak / Karak	1050	6300
Bayer / Eastern desert	2000	12000
Jafer / Southern desert	250	1500
Rukban / North eastern desert	1000	6000
Khanasree / Mafraq	500	3000
Ghadaf / Central desert	250	1500

The obvious benefits of hydropower projects in Jordan, or in any other country where hydropower potential exists, is associated with the generation of electrical power, which has the ability to both assist the sustainable economical development and increase the quality of life. Furthermore, they are labor-intensive during construction, as well as providing long term employment opportunities. Another benefit of exploiting water resources is the environmental concerns, since it is considered as clean and green energy source, releasing no harmful gas emissions as in conventional power stations. With the increasing scarcity of fossil fuel resources, the demand for greenhouse gas reduction and environmental protection all over the world, developing hydropower becomes one of the most important energy strategies. According to statistics, SO2 emissions are about 20 million tons per year, 50% of which are from thermal power [39]. The construction of these projects in Jordan would reduce fuel consumption by about 75 thousand ton/yr of heavy fuel or diesel oil, which costs between US$ 50-60 million, as well as saving at least 2,000 tons of SO2 emissions. In addition, it will help to prevent the discontinuous flow and improve ecosystem as well as reduce floodwater damage in certain locations. Based on the average weighted emission rate from the power sub-sector in Jordan [2], the avoided GHG emission would be between 80,000-100,000 tons for the case of the existing dams and for the proposed dams between 35,000-45,000 tons. Such reduction in GHG emission by using SHP schemes is inevitable and considered as CDM projects, which would yield a net annual income of between US$ 1.2-1.5 million and US$ 0.5-0.7 million for the existing and proposed dams, respectively.

As stated in the national energy strategy, the Government Jordan is committed to increase the sharing ratio of indigenous energy resources, including renewable sources and oil shale, from the current level of less than 0.5 % of the total electricity generation to reach around 10 % from the total installed capacity as outlined in the updated nation energy strategy by the year 2020 [5]. The future development of SHP, including pumped storage, projects would involve different institutions in Jordan, mainly Ministry of Energy and Mineral Resources, Ministry of Water and Irrigation, Jordan Valley Authority, etc., thus, the legal framework and institutional arrangements, e.g. public-private partnership, for the implementation of the identified small hydro projects should be studied and developed soon. Although the SHP projects will focus on power generation from small hydro units and pumped storage schemes, it should address other important issues such as better water management, irrigation, agriculture and possible tourism and recreation activities in the future. But it should be mentioned here that the Government of Jordan has not recognized the important role that mini-hydro plants can play in improving the energy situation in the country and no real effort is paid to develop those sites that have been identified in the current study. Moreover, the absence of targeted incentives for private development of small hydropower is a major barrier. SHP hydro plants are starved of funding, as conventional financiers prefer to fund large scale hydro projects. Thus, The Ministry of Energy and Mineral Resources, Ministry of Water and Irrigation, Electricity Regulatory Commission, etc., should work hard with other concerned institutions on encouraging investors in developing renewable energy projects, including SHP schemes. This will lower the costs of providing electricity as well as increasing security of supplies due to reduced imports of oil and gas as well as pollutant emissions.

The lack of local specialization to undertake feasibility studies for SHP projects, detailed studies that would include design, construction and costing of the schemes to make a meaningful impact on utilization of small hydro sites, contributes to the high costs of procuring the services, and the delays in developing such projects. Waste water treatment plants, e.g. Samra Waste Water Treatment Plant, with electricity as an add-on component are good candidates for multi-purpose projects. Such a multi-purpose project is seen to be more favorable to international financiers than pure electricity supply projects. The present legislations allow for independent power producers (IPPs) to operate in the county, therefore there is no threat to international partners willing to operate SHP plants. One of the main duties of the Ministry of Energy and Mineral Resources and the Electricity Regulatory Commission is to work with other concerned institutions on encouraging investors in developing renewable energy projects, including SHP schemes. This will lower the costs of providing electricity as well as increasing security of supplies due to reduced imports of oil and gas.

To summarize, it can be said that there are candidate sites, i.e. dams and water bodies, which warrant further detailed study and investigation. It is believed that there are at least 6-10 candidate sites in the western part of Jordan and at least 2-3 in the eastern plateau, mainly desert dams, which could be developed as SHP plants. However, further detailed technical and financial studies with certain and clear criteria are required before deciding on any of the presented sites in this study. It may be a good idea that the concerned governmental institutions seek assistance from international donors, such as World Bank, EU, GTZ, JICA, etc., in order to provide technical expertise as well as financial resources needed to develop SHP schemes and other renewable energy projects in Jordan.

6. Conclusion

Jordan is a rapidly growing country regarding its economy and population and therefore has a large and continuously increasing energy demand, and mostly meets its energy demand from imported fossil sources. However apart from petroleum and natural gas, Jordan has vast amounts of various kinds of energy resources, i.e. oil shale, solar and wind, hence it would not need to meet its energy demand through import. In addition, Jordan has a good potential of hydraulic energy but to date only small portion of this significant economical potential was used. In this paper the role of small hydroelectric power, its potential and its present status are investigated in detail for Jordan. The following concluding remarks may be drawn from this research paper:

- Although, Jordan has limited surface water resources, hydropower energy is an important energy source since it is renewable, clean, and less impactful on the environment as well as it is a cheap and domestic energy source.
- The average exploitable potential of the country is estimated at about 33 MW, for the existing dams, therefore, hydropower may possesses sufficient and suitable characteristics which would contribute in maintaining sustainable development through different means: flood control, irrigation, recreation activities as well as supply water for people’s daily life and social life.
- It is apparent that the consecutive government(s) did not recognize the important role that small hydro plants can play in improving the energy situation in the country and no real effort was paid to develop the most promising sites in the country, which have been reported in this study.
- Small hydropower development could offer a leading renewable alternative for meeting electricity demand in remote and mountainous parts of Jordan. The advantages and attractiveness of these small

hydropower plants are that they can either be stand-alone or in a hybrid combination with other renewable energy sources.

Given their high investment costs, the profitability of small hydropower plant projects is a general issue and follows the situation in the local market. But as the future cost of such systems is subject to high uncertainty, this is considered as major barrier that may hinder their utilization in Jordan.

References

[1] MEMR, Annual Report 2010, Ministry of Energy and Mineral Resources, 2011, Amman, Jordan.

[2] A. Al-Ghandoor, J.O. Jaber, I. Al-Hinti, "Assessment of energy and exergy efficiencies of power generation sub-sector in Jordan". Jordan Journal of Mechanical and Industrial Engineering, Vol. 3, 2009, 1-8.

[3] MEMR, Annual Report 2011, Ministry of Energy and Mineral Resources, 2012, Amman, Jordan.

[4] NEPCO, Annual Report 2011, National Electrical Power Company, 2010, Amman, Jordan.

[5] MEMR, Updated Master Strategy of Energy Sector in Jordan for the period (2007-2020), Ministry of Energy and Mineral Resources, 2007, Amman, Jordan.

[6] Anon, Temporary Law No. 3 for the year 2010, Renewable Energy and Energy Efficiency Law, Ministry of Energy and Mineral Resources, 2010, Amman, Jordan.

[7] Special Press Conference, Minister of Energy and Mineral Resources, Minister of Industry and Trade, and Minister of Finance, Chief of Electricity Regulatory Commission, Alghad Newspaper, Tuesday 24 April 2012, Amman, Jordan.

[8] H. Nautiyal, S.K. Singal, A. Sharma, "Small hydropower for sustainable energy development in India". Renewable and Sustainable Energy Reviews, Vol. 15, 2011, 2021-2027.

[9] A. Beluco, P.K. de Souza, A. Krenzinger, "A method to evaluate the effect of complementarity in time between hydro and solar on the performance of hybrid hydro PV generating plants". Renewable Energy, Vol. 45, 2012, 24-30.

[10] B.M. Taele, L. Mokhutsoane, L. Hapazari, "An overview of small hydropower development in Lesotho: challenges and prospects". Renewable Energy, Vol. 44, 2012, 448-452.

[11] Z. Xingang, L. Lu, L. Xiaomeng, W. Jieyu, L. Pingkuo, "A critical-analysis on the development of China hydropower". Renewable Energy, Vol. 44, 2012, 1-6.

[12] B. Dursun, B. Alboyaci, "The contribution of wind-hydro pumped storage systems in meeting Turkey's electric energy demand". Renewable and Sustainable Energy Reviews, Vol. 14, 2010, 1979-1988.

[13] H. Ibrahim, A. Ilinca, J. Perron, "Energy storage systems – characteristics and comparisons". Renewable and Sustainable Energy Reviews, Vol. 12, 2008, 1221-1250.

[14] Anon, American Society of Civil Engineers Task Committee on Pumped Storage, "Hydroelectric pumped storage technology – international experience". 1996, USA.

[15] B. Steffen, " Prospects for pumped-hydro storage in Germany". Energy Policy, Vol. 45, 2012, 420-429.

[16] Chi-Jen Yang, R.B. Jackson, "Opportunities and barriers to pumped-hydro energy storage in the United States". Renewable and Sustainable Energy Reviews, Vol. 15, 2011, 839-844.

[17] J.P. Deane, B.P. O' Gallacho' ir, E.J. Mckeogh, "Techno-economic review of existing and new pumped hydro energy storage plant". Renewable and Sustainable Energy Reviews, Vol. 14, 2010, 1293-1302.

[18] T. Abbasi, S.A. Abbasi, "Small hydro and the environmental implications of its extensive utilization". Renewable and Sustainable Energy Reviews, Vol. 15, 2011, 2134-2143.

[19] R.K. Burns, "Afghanistan: solar assets, electricity production, and rural energy factors". Renewable and Sustainable Energy Reviews, Vol. 15, 2011, 2144-2148.

[20] B. Dursun, C. Gokcol, "The role of hydroelectric power and contribution of small hydropower plants for sustainable development in Turkey". Renewable Energy, Vol. 36, 2011, 1227-1235.

[21] P.S. Nigam, "Handbook of hydroelectric engineering". 2nd edition, 2008, Roorkee: New Chand & Bros.

[22] B.S.K. Naidu, "Small hydro: highest-density, non-conventional, renewable-energy source". 1st edition, 2005, National Power Training Institute.

[23] S.K. Singal, D.K. Khatod, "Optimal installation of small hydropower plant – a review". Renewable and Sustainable Energy Reviews, Vol. 15, 2011, 3862-3869.

[24] V.D. Stevanovic, A. Gajic, L. Savic, V. Kuzmanovic, D. Arnavtovic, T. Dasic, B. Maslovaric, S. Prica, B. Milovanovic, ".

[25] H. Mohmad, H. Mokhlis, A.H. Abu Bakar, H.W. Ping, "A review on islanding operation and control for distribution network connected with small hydro power plant". Renewable and Sustainable Energy Reviews, Vol. 15, 2011, 3952-3962.

[26] A. Pascale, T. Urmee, A. Moore, "Life cycle assessment of a community hydroelectric power system in rural Thailand". Renewable Energy, Vol. 36, 2011, 2799-2808.

[27] S. Kucukali, "Municipal water supply dams as a source of small hydropower in Turkey". Renewable Energy, Vol. 35, 2010, 2001-2007.

[28] ESHA – European Small Hydropower Association, www.esha.be.

[29] O. Yuksek, M.I. Komurcu, I. Yuksel, K. Kaygusuz, "The role of hydropower meeting the electric energy demand in Turkey". Energy Policy, Vol. 34, 2006, 3093-3103.

[30] Y. Yassi, S. Hashemloo, "Improvement of the efficiency of the Agnew micro hydro turbine at part loads due to installing guide vanes mechanism". Energy Conversion and Management, Vol. 51, 2010, 1970-1975.

[31] I.L. Gordon, "Hydropower costs estimates". Journal of Water Power and Dam Construction, Vol. 35, 1983, 30-37.

[32] I.L. Gordon, C.R. Noel, "The economic limits of small and low-head hydro". Journal of Water Power and Dam Construction, Vol. 38, 1986, 23-26.

[33] B. Ogavar, P.G. Vidal, "Cost determination of the electromechanical equipment of a small hydro-power plant". Renewable Energy, Vol. 34, 2009, 6-13.

[34] G.A. Aggidis, E. Luchinskaya, R. Rothschild, D.C. Howard, "The costs of small-scale hydro power production: impact on the development of existing potential". Renewable Energy, Vol. 35, 2010, 2632-2638.

[35] J.O. Jaber, O.O. Badran, N. Abu-Shikhah, **"**Sustainable energy and environmental impact: role of renewables as clean and secure source of energy for the 21st century in Jordan". Clean Technologies and Environment Policy, Vol. 6, 2004, 174-186.

[36] ERC, Annual Report 2010, Electricity Regulatory Commission, 2011, Amman, Jordan.

[37] MWI, Jordan Red Sea Project – 2010, Ministry of Water and Irrigation 2011, Amman, Jordan.

[38] MWI, Annual Report 2010, Ministry of Water and Irrigation 2011, Amman, Jordan.

[39] V.B. Miller, A.E. Landis, L.A. Schaefer, "A bench mark for life cycle air emissions and life cycle impacts assessment of hydrokinetic energy extraction using life cycle assessment". Renewable Energy, Vol. 36, 2011, 1040-1046.

JJMIE

Volume 6, Number 2, April 2012
ISSN 1995-6665
Pages 119 -126

Jordan Journal of Mechanical and Industrial Engineering

Steering Rod Fatigue Test Bench Cam Loading Analysis

Zhong-xing Yang*[,a], Yun-fei Mai[a]

University of Shanghai for Science and Technology, Shanghai, China

Abstract

Steering rods are subject to variety kinds of loads which will eventually cause failure. Automobile manufacturers and engineers are seeking ways to test the fatigue life of the steering rods. Steering rods under periodic loads over millions of cycles will get fatigued. We here provide a fatigue test bench for steering rods which applies periodic loads to the rod with a cam loading system. Cycloid motion is chosen for the cam follower to achieve the smooth and stable kinematic performance in middle and high speed operation. The accuracy of the follower response is analyzed using dimensionless dynamic equation and the application of Matlab is introduced to solve elastodynamic equation and analyze the prime/residual vibration curve of the follower. The cam loading system is built in dynamic analysis software Adams to simulate its virtual operation performance. By calculating the velocity multiplied by acceleration of the follower over the operation period, the extent to which the inertia load from the follower affects the torque on the cam shaft will be obtained with the help of Adams/postprocessor. The force loads acting on the cam shaft can also be acquired using simulation tools. By virtual prototyping the cam loading system's performance can be foreseen before a real prototype is built. Introducing cam loading method into fatigue test is an innovative application.

Keywords: Steering rod fatigue test; Dimensionless dynamic equation; Prime/residual vibration; Inertia load; Virtual prototyping

1. Introduction

Vehicle steering rod is a rod that allows the driver to steer a vehicle by turning the steering wheel. The torque applied by the driver is taken through the steering rod to the actuator, either with a hydraulic power steering (HPS) or an electric power steering (EPS), which will eventually perform the steering action of the road wheels. Because of impacts caused by terrain conditions or loads from the road and rotation of the rod itself, the steering rod will get fatigued after millions of load cycles which will prevent it from acting swiftly and accurately and finally cause it to fail. It is necessary to test the fatigue life of a steering rod.

In a fatigue test, a rotating rod will be held on both its two ends whilst undergoing a constant periodic load acing on the body of the rod which causes periodic deformation. It is required that the body of the rod bends in opposite directions in turn over the operation time until it gradually fails under constant amplitude loads. A loading force is exerted on the rod which varies from minimum to maximum periodically whilst the rod is rotating.

Hydraulic loads can be applied as the loading force and controlled with high flexibility, however the precise action is hard to achieve because of the delay in response and the oil also has its resilience. Hydraulic loads do have their benefits in flexible programmable loading applications, but the main defect is that hydraulic loads will be affected by surplus force happening when there are deviations or interferences in signals then the actual loading curve differs largely from the desired loading force especially in high speed loading operation. Hydraulic can not apply precise action at high speed. And in some cases we will need to devise ways to eliminate the sharp cusps in its loading curve. We here discuss the use of a cam-follower mechanism in test load application.

Cams are widely used in machining centers and packaging industries where precise action and swift response is required. The loads applied in a fatigue test are standardized and are basic constant amplitude loads [1]. It is both suitable and economic to adopt a cam loading system for the test. Due to the simple structure of the loading system, the mass production cost and the weight of the whole machine are greatly reduced.

High stiffness spring can provide a heavy load which is an alternative way to replace the hydraulic loads. A cam in the loading system can convert the displacement of its follower into a load when a spring is compressed. By choosing the exact stiffness coefficient of the loading spring and the contour of the cam, a force curve against cam revolution angle will be obtained. The frequency of the load peaks is determined by adjusting the revolution speed of the cam shaft and that of the tested rod.

The systematic sketch of the test bench is shown in Figure 1 where a cam applies a load on the rotating steering rod through the loading tip that is pressed against the rod by the compressed spring. Analog signals will be collected by the sensor and sent to the signal processor where analog signals are converted to digital signals and finally the digital signals will be sent to the computer and analyzed. In this paper, we discuss the dynamic performance of the cam-follower loading system.

Because the cam shaft and the tested rod can turn at different speeds, in this case the revolution speed of the cam shaft is twice that of the rod, when the rod completes a turn of 360 degrees it receives the maximum loading

[*] Corresponding author. e-mail: fivemiles555@163.com

force from the cam loading system twice which act on the opposite cylindrical side of the rod. The loading force curve is a set of pulses with each pulse rising up reaching its peak and then falling, in a same rate of its rising, touching the bottom.

After a physical prototype of test bench is built, when required loads are applied periodically to the rotating rod, sensors mounted on the rod body can measure the deformation of the rod body and physical features of interest can be acquired. With a combination of sensors, analog-digital signal converter and processer, the data will be sent to the computer and analyzed.

We are able to test different rods on the bench and loading force can be magnified by using springs with a higher stiffness. A set of cams with different contours can be designed in preparation for other commonly practiced test curves. It is recommended to apply B-splines method to design the contour of a cam when the loading curve is unique. B-splines method can optimize the follower's motion by minimizing the peak velocity and acceleration and also the jerk by selecting key points which are liable to provide an improved follower motion. Coupled with CAD/CAM and CNC, the cam profile is easy to be designed and manufactured. The way to obtain a cam profile with improved motion is to pick key points in its velocity curve, then calculate the displacement curve by integrating the velocity curve and the acceleration or jerk curve by differentiating. When the basic motion is chosen for the follower, the curve of the cam outline can be interpolated with 3 degree polynomial functions to ensure smoothness of the curve. [2]

By switching cams or springs, we acquire a variety of cam-spring matches that can apply different loads for different test tasks. Another option for applying unique loads is to employ non-linear stiffness springs each with a required load-displacement curve. The smoothness of the follower's motion depends on the contour of the cam which is optimized by picking key points in velocity curve. If we change springs instead of the cam to match different loading curve, this can ensure equal smoothness of the follower motion for different loading curve. However a non-linear spring will greatly increase the development and production cost. Moreover the loading curves for fatigue test are generally basic periodic curves, so it is not necessary to apply special loading curves.

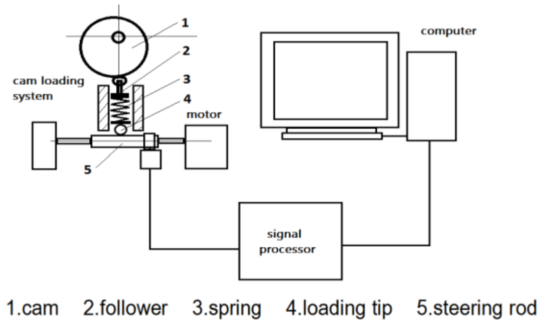

Figure 1: Test bench layout.

For linear spring, the loading force is in proportion to the follower's displacement.

The cam contour is to be designed in consideration of the dynamic performance of the follower to guarantee accurate response and also to avoid follower lift off. Kinematic features such as velocity, acceleration and the product of the two all need to be monitored because in certain applications the inertia load of the follower will have an impact on the cam shaft torque [3]. And the forces acting on the cam shaft also need to be measured for safety operation and service life. Hopefully these calculations can be done conveniently with the help of CAE and Numerical tools.

2. Cam Profile Design

The cam profile is designed according to the constant amplitude loading curve. The profile of the cam should prevent the reciprocating follower from suffering abrupt changes in velocity or acceleration. For high speed application, higher derivative of the displacement will need to be examined to prevent flexible impacts. The cycloid motion is suitable for mediate or high speed application, because it has continuous velocity and acceleration. In resent research, the third derivative of the displacement, known as jerk, is also checked for continuity when cam speed is high. Cycloid curve has many advantages in terms of less noise, vibration and wear, so cycloid curve is always chosen for high speed operation. [2]

The structure of the transmission mechanism should be as compact as possible while ensuring robustness thus saving room for other components.

On an actuate phase, pushed by the outline of the cam, the follower extrudes from its original stationary position while pressing back a spring mounted on it until reaching the farthest position in its motion. The displacement *S* of the follower with respect to the cam's angular displacement is given by Eq. (1).

$$s = \frac{h}{\phi}\varphi - \frac{h}{2\pi}\sin\left(\frac{2\pi}{\phi}\varphi\right) \tag{1}$$

Where φ represents the angular displacement of the cam; ϕ is a constant representing the actuate angle of the cam; h is the displacement made by the follower from its nearest position to the farthest position.

On a return phase, the follower is pushed by a force from the compressed spring until it returns to its original position. Then the spring resumes its original length. The displacement of the follower is given by Eq. (2).

$$s = h - \frac{h}{\phi'}\varphi + \frac{h}{2\pi}\sin\left(\frac{2\pi}{\phi'}\varphi\right) \tag{2}$$

Where ϕ' is a constant representing the return angle of the cam.

Figure 2 shows the follower's reciprocating displacement with respect to cam's angular displacement.

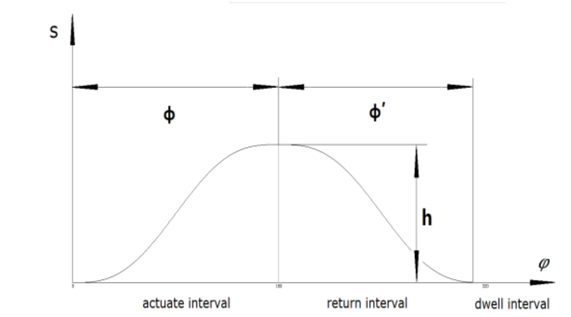

Figure 2: The follower's displacement curve.

By solving the displacement equation for higher derivatives, the follower's dynamic performance at high speed is obtained. B-splines methodology is able to plot the cam outline by polynomial interpolation and also facilitates manufacturing the cam profile with computer numerical control (CNC).

After the actuate length h is determined, the stiffness of the spring can be defined with the maximum load force value divided by h.

3. Elastodynamic Analysis

It is considered that all parts composing the mechanism are resilient and are deflected under loads.

So the follower can be seen as a high stiffness object. If the follower is compressed by high elastic load when accelerated, the deflection produces energy which is stored in the follower, and it will later release substantial energy to cancel out the spring force [4]. This excitation from the load causes transient chaotic motion in the follower and is the reason for the follower's vibration which will last till the end of the actuating period. It is necessary to evaluate the follower's response to the external excitation when the operation speed is high. The dynamic model must be built for analysis.

Within the cam loading model, the follower and the loading tip are respectively defined as objects with masses equal to m_1 and m_2. The follower receives a displacement excitation s at its upper end where it contacts the surface of the cam with contact stiffness k_1; the displacement response of the follower is y_1 measured at the other end of the follower. The follower is connected to the loading tip through a spring with stiffness k_s and preload F_p. The displacement response of the loading tip is y_2. Steering rod has revolute constraints at both of its ends and is seen as a body with one resolute degree of freedom about its longitude axis. The contact stiffness between the loading tip and the steering rod is k_2. We obtain the following Eq. (3).

$$\begin{aligned} m_1\ddot{y}_1 &= k_1(s-y_1)-k_s(y_1-y_2)-F_p \\ m_2\ddot{y}_2 &= F_p+k_s(y_1-y_2)-k_2y_2 \end{aligned} \qquad (3)$$

Equation (3) is based on the dynamic model (see Figure 3.a) which considers vibration in the loading tip. However the contact stiffness k_2 is much higher than the spring stiffness k_s and there is no external excitation from the steering rod. For simplification, we can remove m_2 from the model and focus mainly on the response of the follower (see Figure 3.b). The modified equation is given as below.

$$m_1\ddot{y}_1 = k_1(s-y_1)-F_p-k_sy_1 \qquad (3)$$

Because F_p is only considered for static deformation and we also notice that $k_1 >> k_s$, Equation. (4) is further simplified as below.

$$m_1\ddot{y}_1 + k_1y_1 = k_1s \qquad (4)$$

The contact stiffness k_1 is defined as the ratio of contact force to the follower's deformation. As the follower can be made from a variety of materials and designed into different shapes, the contact stiffness is a natural attribute once the cam and the follower are designed. By finite element analysis (FEA), the contact stiffness can be calculated.

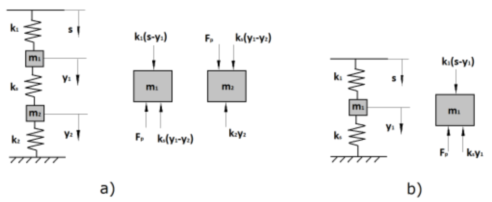

Figure 3: Dynamic model.

On the actuate phase, the follower is excited by the contact force and responses to that force with a displacement in downward direction. This is the prime vibration period of the loading operation and will last until the follower reaches the lowest position of its motion.

A dimensionless equation can be used to compare the follower's dynamic responses with different motion periods regardless of the particular features of a cam loading system [3]. It is assumed that displacement and time are expressed as unities.

With $Y=\frac{y_1}{h}$, $T=\frac{t}{t_h}$, $S=\frac{s}{h}$, $\ddot{y}_1=\frac{d^2y_1}{dt^2}=\frac{t}{{t_h}^2}Y''$, and the periodic features $\omega_n=\sqrt{\frac{k_1}{m_1}}$, $t_0=\frac{2\pi}{\omega_n}$, $\lambda=\frac{t_h}{t_0}$, where ω_n is the natural frequency of the follower and t_h represents the length of time of the actuate phase, we change Eq.(5) into a dimensionless Eq.(6) about the period ratio λ.

$$Y''+(2\pi\lambda)^2Y=(2\pi\lambda)^2S \qquad (6)$$

If substituting the actual displacement equation into Eq.(6), the response of the follower for prime vibration period is expressed as below.

$$Y'' + (2\pi\lambda)^2 Y = (2\pi\lambda)^2 (T - \frac{1}{2\pi}\sin 2\pi T) \tag{7}$$

When the cam shaft stops rotating, there is no excitation acting on the follower. The residual vibration period is on until the remaining energy in the follower dissipates out for example to be absorbed by the damping or friction. The dynamic equation to describe this period is given by Eq. (8).

$$m_1 \ddot{y}_r + k y_r = 0 \tag{8}$$

To change it into a dimensionless equation, we obtain Eq. (9).

$$Y_r'' + (2\pi\lambda)^2 Y_r = 0 \tag{9}$$

The dimensionless displacement Eq. (7) and Eq. (9) are to be solved in conjunction with the initial displacement and velocity conditions. The initial definition of velocity and acceleration need to be described according to practical conditions.

4. Inertia Load Analysis

In high cam speed operation, the follower is moving with high acceleration and velocity. The follower, the reciprocating part of the cam loading system produces inertia load on the cam shaft. Factors like the mass of the follower and the revolution speed of the cam shaft are all responsible for the inertia load. If the follower has a large mass and the operation speed is high, the inertia load will play a significant part in the cam's dynamic load. It is appreciated that the inertia load should be limited to a relatively small value compared to the working load. The magnitude of the inertia load can be deduced from a force diagram of the cam loading system (see Figure 4).

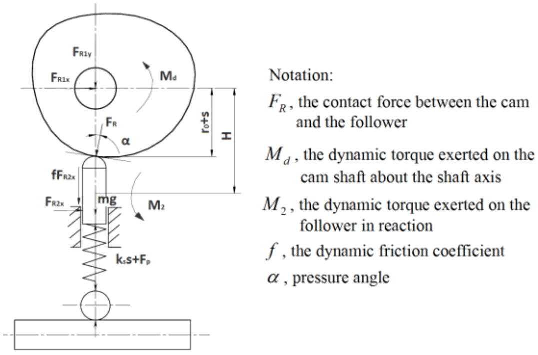

Figure 4: Force diagram.

For the follower, the equilibrium equation is expressed as:

$$\begin{aligned} &-m\ddot{s} + k_s s + F_p - \delta f F_{R2x} - mg - F_R \cos\alpha = 0 \\ &F_{R2x} - F_R \sin\alpha = 0 \\ &F_R (r_0 + s)\sin\alpha - F_{R2x} H - M_2 = 0 \end{aligned} \tag{10}$$

Where an item with subscript x implies the lateral component of the item and pressure angle is,

$$\alpha = \tan^{-1}\left[\frac{\dot{s}}{(r_0 + s)\omega}\right] \tag{11}$$

To distinguish the direction of the friction force, it is assumed that If $\dot{s} > 0$, $\delta = -1$; if $\dot{s} < 0$, $\delta = 1$. The first derivative of s indicates the velocity of the follower and positive or negative value of which implies the direction of the follower's motion.

For the cam, the equilibrium equation is:

$$\begin{aligned} &F_{R1y} - F_R \cos\alpha = 0 \\ &F_{R1x} + F_R \sin\alpha = 0 \\ &M_d + F_R (r_0 + s)\sin\alpha = 0 \end{aligned} \tag{12}$$

Where item with subscript y implies the vertical component of the item. Combining Eq. (11) and Eq. (12), the contact force F_R and the cam shaft dynamic moment load M_d are given,

$$\begin{aligned} &F_R = \frac{k_s s + F_p - mg - m\ddot{s}}{\delta f \sin\alpha + \cos\alpha} \\ &M_d = \frac{\dot{s}}{\omega}\frac{mg + m\ddot{s} - F_p - k_s s}{\delta f \tan\alpha + 1} \end{aligned} \tag{13}$$

By inspection of Eq. (13), the product of the follower's velocity and acceleration partially determines the follower's inertia load on the cam shaft torque. In designing the cam loading system, the mass of the follower, the velocity and acceleration of the follower must be carefully monitored or this will cause a fluctuation in the cam shaft torque load, even more so when the cam revolution speed is high.

5. Example of a Loading Practice

The fatigue life tests are practiced based on the loads data recorded from real road running test. The loading frequency should be higher than 5 Hz or it will have no effect on the steering fatigue life while kept away from the natural frequency of the steering rod to prevent resonant vibration. According to the data collected from the road, only load frequencies higher than 6 Hz will be applied in fatigue test [5]. Here we choose a loading frequency of 10 Hz and loading amplitude of 5000 N. Because the rod natural frequency is estimated at 50 Hz, so the loading frequency will not cause resonant vibration.

With the application of numerical and dynamic software, the loading performance can be tested virtually. As is already explained in section 2, the displacement response Eq. (7) and Eq. (9) indicate the follower's responses during prime vibration phase and residual vibration phase. The differential equations are solved using Matlab tool. Because the response behavior varies according to the period ratio λ , different response curves need to be plotted out for comparison with the theoretical response curve. The initial conditions are specified that the velocity and acceleration are both zeros at the beginning of the practice. A table is shown below indicating the parameters defined for this practice. (See section 2 for the equations of these parameters).

Table 1: Practice parameters

Items	Value
Actuate length h	$0.05m$
Loading spring stiffness k_s	$1.0\times10^5 N/m$
Peak loading force $k_s \times h$	$5.0\times10^3 N$
Actuate angle ϕ	$2.79 rad$
Cam shaft speed n	$600 RPM$
Contact stiffness k_1	$22,727,300 N/m$
Natural frequency ω_n	$3,866.8 rad/\sec$
Actuate phase period t_h	$4.4\times10^{-2}\sec$
Natural period t_0	$1.625\times10^{-3}\sec$
Period ratio λ	27

5.1. Matlab solution:

The Eq. (7) and Eq. (9) with their initial conditions are expressed in Matlab respectively as below,

y=dsolve('D2y+…*y=…*(t-sin(…)','y(0)=0','Dy(0)=0','t');

y=dsolve('D2y+…*y=0','y(1)=1','Dy(1)=0','t').

The theoretical response curve is y=t-sin(2*pi*t)/(2*pi).

The displacement curves are plotted as shown in Figure 5 (Figure 5.a represents the prime vibration period and Figure 5.b represents the residual vibration period.). By inspection of figure 5.a, we conclude that the response curve of practice loading (line 2) coincides with the theoretical response curve (line 1). For comparison, when period ratio is equal to 1, the response curve (line 3) is significantly biased from the theoretical one (line 1).

The residual vibration curve has a pattern which resembles a line of leaf shaped patches when the period ratio gets high. (see figure 5.c).

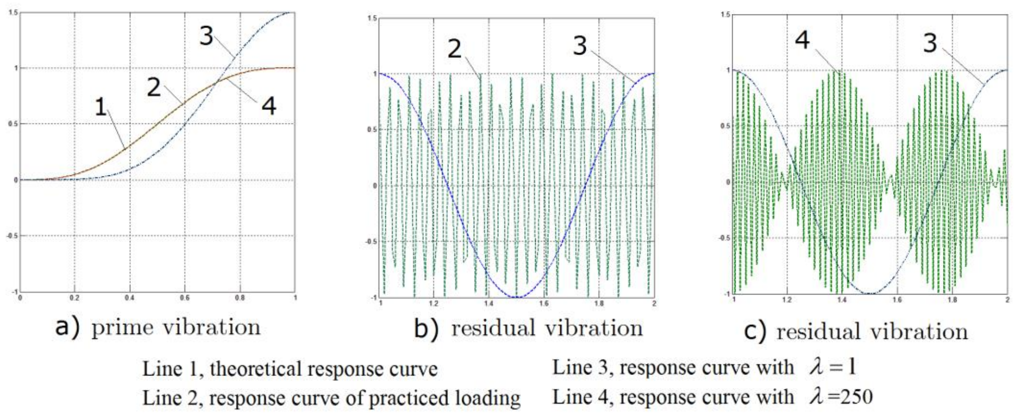

Figure 5: Displacement response curves.

5.2. Adams simulation:

5.2.1. Cam profile modeling with B-splines polynomial interpolation:

Basically, a contour of the cam requires at least 6 key points in either the actuate interval and return interval to manipulate the outline of the cam. The smooth curve to connect the key points is formed using B-splines interpolation. The polynomial interpolation equations have 3 degrees.

An arbitrary point on an interpolated curve which has (k-1=3) degrees and is manipulated with (n+1) key points can be presented as below. [2]

$$P(u) = \sum_{i=0}^{n} N_{i,k}(u)P_i \tag{14}$$

Where u is the length of interpolation, the range of which is u (0, n-k+2); $N_{i,k}(u)$ is the interpolation function; P_i is a key point. (for more details of Eq. (14) and B-splines interpolation method see reference [2])

Adams models the cam with B-splines interpolation as key points are picked in the path of the outline. This ensures the smoothness of the curve and also facilitates manufacturing with computer aided manufacturing tools. The possible optimization can be done by re-picking the key points.

Table 2 lists the key points which compose the outline of the cam at an interval of 10 degrees starting from 0 to 360 degree. Figure 6 shows the final design of the cam profile.

Table 2: Cam profile key points.

Angular displacement (°)	Radial distance from the cam basic circle (mm)	Angular displacement (°)	Radial distance from the cam basic circle (mm)
0	0	170	49.9203
10	0.0797	180	49.377
20	0.623	190	47.977
30	2.023	200	45.4577
40	4.5423	210	41.727
50	8.273	220	36.877
60	13.123	230	31.1703
70	18.8297	240	25
80	25	250	18.8297
90	31.1703	260	13.123
100	36.877	270	8.273
110	41.727	280	4.5423
120	45.4577	290	2.023
130	47.977	300	0.623
140	49.377	310	0.0797
150	49.9203	320	0
160	50	320-360	0

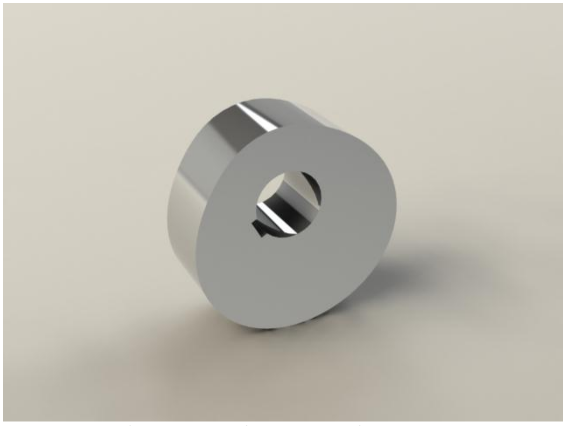

Figure 6: The final design of the cam profile.

5.2.2. Dynamic simulation:

The loading operation can be simulated in Adams to foresee its real performance. The preciseness of the simulation results relies on the correct definition of the behavior and conditions of the loading model.

A dynamic model is built as figure 7 a) shows, where the motions are defined for the cam shaft and steering rod. It is highly recommended to define the contact force as the relationship between the cam's outline and the follower's top end because if the relationship between them is defined as 2D curve-curve constraint type, the lift-off will not be simulated. All the parameters should be set as table 1 shown. A preload of 100N is applied to eliminate the tiny clearance between the cam and the follower.

The extent to which the follower's inertia load can affect the cam shaft torque is obtained by multiplying the acceleration of the follower by its velocity as discussed in Eq. (13). The product of the two characteristics is plotted by using Adams/postprocessor. As shown in figure 8 a), once the simulation is run, we can plot the velocity curve and acceleration curve, and by adding those two plots in one sheet a curve representing the velocity multiplied by acceleration over a same period of time can be plotted using Adams/postprocessor. The time when the maximum point of the product occurs and its specific value can be measured by tracking the plot. Due to the cam profile and the operation speed chosen for the simulation, the maximum value of the product is measured at 220 m^2/sec^3 , however when devided by the revolution speed and multiplied by the mass of the follower the resulting moment value is 5.25 Nm, therefore the cam shaft torque is not affected (see figure 8 b), because the peak torque measured in the loading operation is 100Nm which is much greater than 5.25 Nm caused by inertia load. In figure 8 b), the curve of the product of velocity and acceleration and the curve representing the torque are shown in one sheet. Torque curve implies the magnitude of pressure angle, for when the torque is zero the pressure angle is also zero and when the torque reaches its peak point the pressure angle also reaches its maximum value. Because the inertia torque produced by the follower is partially decided by the pressure angle, by analyzing both the product curve and the torque curve in one sheet can help to focus on the peak value in product curve which coincides with the peak torque value. When two peak values happen at the same time or very near in time, the inertia torque has its greatest effect on the operation torque. In this loading case, the effect is too limited to alter the operation torque.

If in any case the inertia load is large enough to affect the shaft torque, the speed need to be decided again. In loading operation where we have several pairs of cam-spring matches previously prepared, if the operation torque exceeds the designed torque for the shaft, this is the time to switch to a cam with a lower displacement and a matching spring with a higher stiffness. However there is no need adjusting the operation speed or switching to other cam-spring pair when the resulting torque exerted on the shaft is within the safety range. The safety loads for the cam shaft must be checked when designing the shaft. The shaft's mounting diameter and key applied to lock the cam on it should be selected based on the peak loads exerted on the body of the cam shaft. Virtual simulation facilitates the calculation of the critical load values.

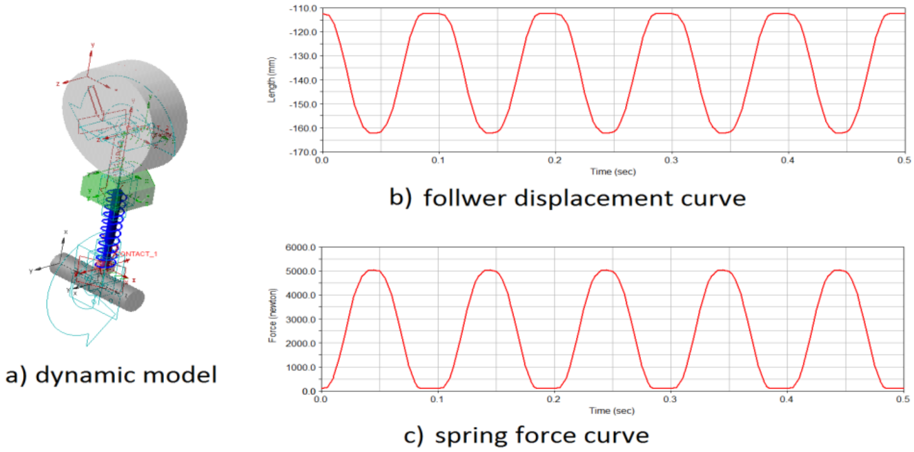

Figure 7: The Adams model of loading system.

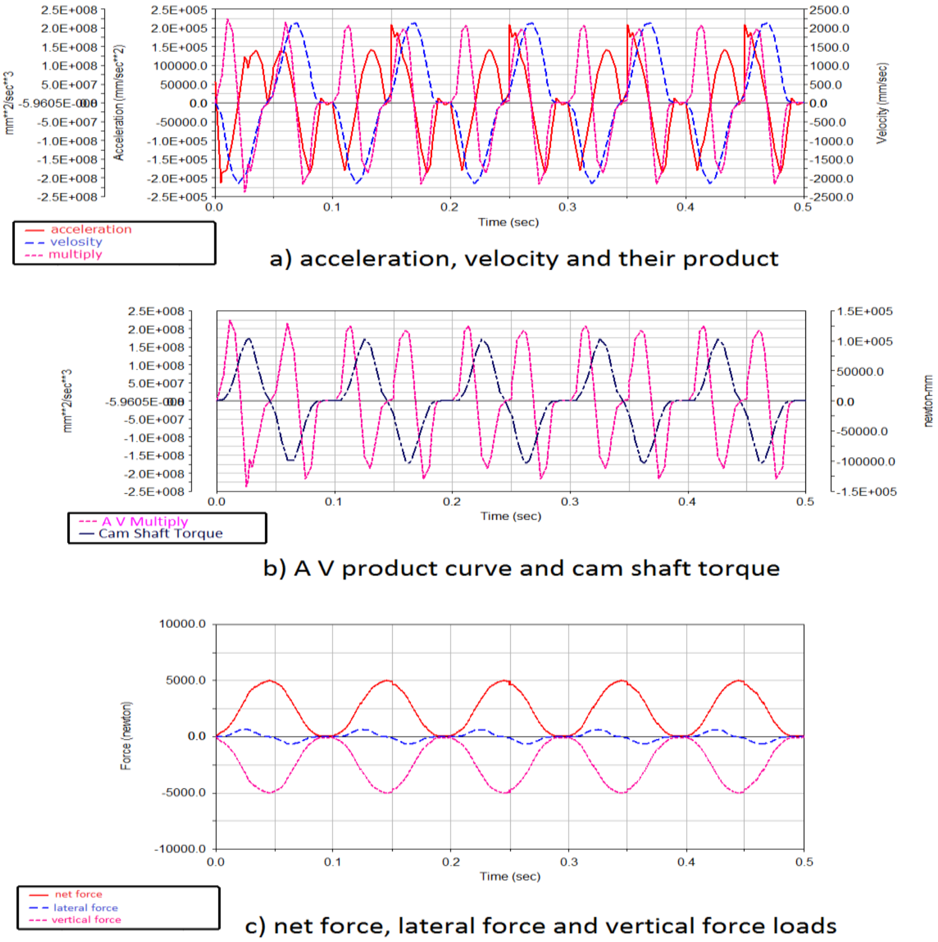

Figure 8: The product of the follower's acceleration and its velocity.

The force loads exerted on the cam shaft are given in figure 8 c). The value of a certain point on the curve can be measured with Adams/postprocessor. From figure 8 c), we can see that the vertical force forms a main part in net force load because the pressure angle (Eq. (11)) is small all the time during the loading practice. The force loads also need to be kept within safety range to prevent failure in cam shaft. Because the cam is locked on the cam shaft with a key, there is no relative rotary movement between the cam and the shaft, so the maximum force load on the shaft reside in a constant area.

6. Conclusion

The cam-spring loading system is introduced to apply periodic loads for fatigue test. With elasto-dynamic analysis and Matlab tools, the responses curves of the follower on its prime and residual vibration periods can be obtained. Based on the calculation of the system's loads in motion and Adams dynamic simulation, the performance of a loading practice can be evaluated. This introduces an alternative way to test the fatigue life of a steering rod by a cam-spring loading set instead of hydraulic means and may also apply to test other rod shaped components when the loading curve has a periodic feature.

References

[1] Lee, S. 1986, "Structural Fatigue Tests of Automobile Components Under Constant Amplitude Loadings" ASM 1986. Pp177-186.

[2] Sateesh,B., Rao,C.S.P. &T.A. Reddy,J.2009, "Optimization of cam-follower motion using B-splines", International Journal of Computer Integrated Manufacturing 2009.Vol.22,No.6, Jun 2009, pp515-523.

[3] Zhang, C. 2008, Machinery Dynamics, 2nd Edition, Higher Education Press, Beijing.pp241-245.

[4] Chen,X.S.&Pu,X.J.2007, "Research on advanced design method of cycloid cam mechanism system", Mechanical Design & Manufacture 2007.Vol.12 No.11,Dec 2007, pp26-28.

[5] Koca,B.&Ekici,B.2010, "Fatigue Life Prediction of a Drag Link by Using Finite Element Method" Proceeding of ASME 2010 10th Biennial Conference on Engineering Systems Design and Analysis, Istanbul, Turkey, July.

[6] Zhou,H.J. 2006, Machine Theory, 2nd Edition, Higher Education Press, Beijing.pp113-153.

[7] Wang,J.W.&Wang.H.&Jiu,H.2008, Matlab7.0 Programming, Mechanical Industry Press, Beijing. pp131-132.

[8] Jia,C.Z.&Yin,J.H.2010, MD Adams Virtual prototyping, Mechanical Industry Press, Beijing. pp116-124.

[9] Gao,L.X. 2011, "Force Loading Cam Design and Simulating By Adams" 2011 International Conference on Consumer Electronics, Communications and Networks, Xian Ning, China, April.

JJMIE

Volume 6, Number 2, April 2012
ISSN 1995-6665
Pages 127 - 133

Jordan Journal of Mechanical and Industrial Engineering

Polyvinyl Butyral (PVB) and Ethyl Vinyl Acetate (EVA) as a Binding Material for Laminated Glass

O. Alsaed[a], I. S. Jalham[b,*]

[a]Graduate student, Industrial Engineering Department, University of Jordan, Amman, Jordan
[b]Industrial Engineering Department, University of Jordan, Amman 11942 Jodan

Abstract

The effect of the type of the bonding interlayer on the mechanical behavior of laminated glass was studied in this paper. Furthermore, this investigation presents mathematical models that helps in predicting this behavior based on the glass plate thickness and the type and thickness of the bonding material. Both practical results and the theoretical model indicate that the failure strength of laminated glass bonded with either PVB or EVA decreases as the interlayer thickness increases. Moreover, the failure strength of the glass bonded with EVA is greater than that for the PVB bonded ones under the same conditions. On the other hand, it was observed that the ability of laminated glass to absorb energy increases with the increase of the interlayer thickness and the increase of glass plate thickness.

1. Introduction

Ceramics and glasses, which have strong ionic-covalent chemical bonds, are very strong and stiff. They are also resistant to high temperatures and corrosion, but are brittle and prone to failure at ambient temperatures. In contrast, thermoplastic polymers such as polyvinyl butyral, which have weak secondary bonds between long chain molecules, exhibit low strength, low stiffness, and a susceptibility to creep at ambient temperatures. These polymers, however, tend to be extremely ductile at ambient temperatures. When combine glass and polymer to form a laminated glass, some change in the failure strength will occur, which depends on both the glass and polymer type. This led to investigate how the glass thickness and the type and number of laminated interlayer affect the maximum load capacity of laminated glass as well as their effect on the absorbed energy.

2. Literature Review

Laminated glass consists of two or more glass plies bonded together with an elastomeric interlayer, usually polyvinyl butyral (PVB) or Ethyl Vinyl Acetate (EVA). After breakage, the interlayer holds the resultant glass shards in place and, in most cases, the glass remains in the frame when laminated glass fractures. This post-breakage characteristic of laminated glass has made it desirable for use in vehicle windshields for decades because it makes the occupant safer from glass shards than other glazing materials.

The shear modulus studies were carried out by Quenett [1], and Hooper [2]. Quenett [1] noticed that when the interlayer thickness decreases, shear modulus increases and reported that the condition of the interlayer is a controlling factor in static bending and dynamic impact resistance. Hooper [2] confirmed the results of Quenett [1]. He stated that after testing glass beams in four point loading with varying temperatures and interlayer hardness, he found that the shear modulus of the interlayer is inversely proportional to the interlayer thickness and also mentioned that plasticizer contents, ambient temperatures, and load durations are the primary factors controlling bending resistance of laminated glass. He attributed this behavior to the "thermoplastic" nature of the interlayer, stating the decreased bending stiffness was the primary disadvantage to architectural laminated glass.

Strength of the monolithic and laminated glasses taking into account the geometry and thickness of the tested plates was studied by several researchers. For example, Pilkington Ltd. [3] compared monolithic glass strength to the strength of laminated glass specimens made of sheet and float glass. They found that, at normal temperature, laminated glass specimens exhibit the same strength as monolithic glass specimens having the same rectangular dimensions and glass thicknesses. On the other hand, Linden et al. [4] conducted a non-destructive test on monolithic, layered, and laminated glass specimens instrumented with strain gages. They concluded that laminated glass strength and monolithic glass strength appeared to be equivalent at normal temperatures; and the strength of laminated glass specimens approached that of layered glass specimens at elevated temperatures. In addition, Norville [5] tested two laminated glass specimen of sizes 38 x 76 and 66 x 66 in. destructively. His

* Corresponding author. e-mail: jalham@ju.edu.jo

destructive experimentation also showed that the strength of laminated glass specimens is the same or greater than that of monolithic specimens having the same rectangular dimensions and nominal thicknesses under similar load conditions.

Keller [6] used novel method to measure the delaminating energy in laminated glass in the relevant dynamic range. He found that increasing the interlayer thickness improves the penetration resistance of laminated glass because more energy can be absorbed in the high speed delimitation process since the interlayer is simply less like to tear.

In contrast to the results of the above mentioned researches contradiction was reported in Nagalla et al [7]; Minor and Reznik [8]. Nagalla et al [7] in their advanced theoretical work compared layered glass to monolithic. They discovered that some aspect ratios of the layered glass experienced lower principal stresses than monolithic glass subjected to uniform, transverse loading in some ranges of the loading. They concluded that the strength factor of 0.6 used by some building codes for laminated glass may be too low for many window geometries and design pressures.

Minor and Reznik [8] destructively tested three sizes of laminated glass specimens (33 x 66, 38 x 76, and 66 x 66 in.) with an 0.030 in. interlayer, and compared the resulting failure pressures to those from tests on monolithic glass specimens having the same rectangular dimensions and nominal glass thicknesses. They introduced four variables, which are: glass thickness, glass type, temperature, and damage to one plate of glass (i.e., damage to tension or compression side). Their testing led to the following general conclusions:

- laminated glass specimens tested at room temperature have approximately the same failure pressure as monolithic glass specimens having the same rectangular dimensions and nominal glass thicknesses
- As temperature increases laminated glass behavior migrates towards the layered glass model
- Laminated glass specimens having twice the nominal glass thickness of monolithic specimens display strength greater than or equal to twice the strength of the monolithic specimens.

Some researchers investigated the effect of temperature on the properties of glass. Linden et al [4] conducted non-destructive testing on two different plate geometries. First, they tested the same plate geometry (60 x 96 x 1/4 in.) as used in the parent report to study load duration and temperature effects. Second, they tested a different geometry (55-1/8 x 57-1/8 x 3/8 in.) with two interlayer thicknesses (0.030 and 0.060 in.) to study the effects of interlayer thickness on strength and deflection. They conducted destructive tests on one plate geometry (60 x 96 x 1/4 in.) at room temperature and at 170°F. Perusal of their data indicates that while load duration and elevated temperatures acting individually reduce the structural rigidity of the laminated glass, the two factors do not interact, producing a greater combined reduction in laminated glass strength. Weller [9], Used experimental study to compare different interlayer materials in laminated glass in respect to their structural behavior. The material properties above the verification temperature clearly showed the temperature dependency. The relaxation times fall with increasing temperature and the shear stress gets smaller.

Theoretical modeling of the glass behavior was also carried out by many researchers. Linden et al. [4] derived theoretical results through the finite difference solution and compared experimental and theoretical results. They concluded that the theoretical finite difference model for monolithic and layered glass appeared to be acceptable for the one glass plate geometry tested. Moreover, Behr and Kremr [10] used experimental validation of a mechanics-based finite element model for architectural laminated glass units subjected to low velocity and two gram projectile impacts. The impact situation models a scenario commonly observed during severe windstorms. This study confirmed the ability of an analytical finite element model to predict accurately the peak strains in representative architectural laminated glass units as a function of impact velocity. Correlations between peak radial strains computed using finite element analysis and those measured experimentally were close, with the average difference between analytical predictions and experimental data being 7.7%.

Zang et al [11] investigation focused on the use of the 3D discrete element method to study the impact fracture problem of laminated glass. The glass and the (PVB) of laminated glass plane are discretized to uniform rigid spherical elements. This investigation showed that the accuracy of the 3D model and numerical analysis code are more validated in the elastic range by comparing with FEM.

Recently, Belies [12] compared (PVB) with stiffer and stronger interlayer Sentry Glass Plus (SGP). After breakage of both glass sheets the load decreased to a relatively low level (typically between 2 kN and 3 kN) before the broken glass pieces and interlayer started again to build up compressive and tensile stresses, respectively. Subsequently, the load slightly increased again and after reaching the maximum, it decreased significantly (to less than 0.3 kN). When subjected to in-plane bending (buckling prevented), the post breakage residual resistance is relatively poor for both interlayers, as illustrated above. The residual load-bearing capacity was very limited and far below the initial glass strength.

It is clear from the above review that the research work focused on the comparison between the strength of monolithic and laminated glasses and did not take into consideration the bonding interlayer thickness, and the position and thickness of the glass plates. Furthermore, the main bonding material in these studies is PVB. This investigation differs from the above mentioned ones in that it concentrates on how the glass thickness and the type and number of laminated interlayer affect the maximum load capacity of laminated glass as well as their effect on the absorbed energy.

3. Materials, Equipment, and Experimental Procedure

3.1. Material:

the materials used in this investigation are float glass plates, and Polyvinyl Butyral (PVB) and Ethylene Vinyl Acetate (EVA) as interlayer materials. The maximum force capacity and the amount of the absorbed energy of the laminated glass were determined for the input variables that are summarized in Tables 1-4 below. Figure 1 shows the schematic diagram for the assembly of the glass plates and interlayer.

Table 1: PVB samples For Bending and Charpy Impact Tests (the outer plates and interlayer thickness changeable).

One interlayer		Four interlayers		Six interlayers	
Inner plate (mm)	Outer plate (mm)	Inner plate (mm)	Outer plate (mm)	Inner plate (mm)	Outer plate (mm)
4	4	4	4	4	4
4	6	4	6	4	6
4	8	4	8	4	8
4	10	4	10	4	10
4	12	4	12	4	12

Table 2: PVB samples for Bending and Charpy Impact Test (the inner plates and interlayer thickness changeable).

One interlayer		Four interlayers		Six interlayers	
Inner plate (mm)	Outer plate (mm)	Inner plate (mm)	Inner plate (mm)	Outer plate (mm)	Inner plate (mm)
4	4	4	4	4	4
6	4	6	4	6	4
8	4	8	4	8	4
10	4	10	4	10	4
12	4	12	4	12	4

Table 3: EVA samples for Bending and Charpy Impact Tests (the outer plates and interlayer thickness changeable).

One interlayer		One interlayer		One interlayer	
Inner plate (mm)	Inner plate (mm)	Inner plate (mm)	Inner plate (mm)	Inner plate (mm)	Inner plate (mm)
4	4	4	4	4	4
4	6	4	6	4	6
4	8	4	8	4	8
4	10	4	10	4	10
4	12	4	12	4	12

Table 4: EVA samples for Bending and Charpy Impact Tests (the inner plates and interlayer thickness changeable).

One interlayer		One interlayer		One interlayer	
Inner plate (mm)	Inner plate (mm)	Inner plate (mm)	Inner plate (mm)	Inner plate (mm)	Inner plate (mm)
4	4	4	4	4	4
6	4	6	4	6	4
8	4	8	4	8	4
10	4	10	4	10	4
12	4	12	4	12	4

3.2. Equipment:

Equipment used in this investigation are Glass cutting machine of BSJ-NL3725 type, Bend testing machine of OUTOGRAPH AG – 1S type, and Charpy testing machine.

3.3. Experimental procedure:

testing procedure can be summarized as follows:

- Cutting plates of 40 cm x 30 cm from glass panels of 4 mm, 6 mm , 8 mm, 10 mm, 12 mm thicknesses. The sharp cut edges have been broken off or beveled with a grinding tool
- Manufacturing of PVB-laminated glass. It comprises the washing and drying of individual glass sheets, laying the PVB film between the two glass sheets by using roller process, and heating and pressing the assembly.

An assembly full-surface bond is created in an autoclave using temperatures of about 140 °C and pressure of about 150 psi. The interlayer becomes a viscous at this temperature and pressure, and any remaining air dissolves into the laminate layer.

- Manufacturing of EVA laminated glass. It comprises the washing and drying of individual glass sheets, laying the EVA film between the two glass sheets by using roller process, and the assembly is headed in single stage lamination process (vacuum with integrated heating and cooling in the same apparatus)
- Cutting of the manufactured laminated glass to the required size by using the cutting machine. For point bend test, the rectangular sheets dimension is 80mm x 300mm while for Charpy test, the rectangular sheets dimension is 80mm x 300mm.

4. Results and Discussions

As stated before, the maximum force capacity and the amount of the absorbed energy of the laminated glass were determined for the input variables that are summarized in Tables 1-4 for the assembly shown in Figure1. The results and discussions of the investigation will be briefed in the following sections.

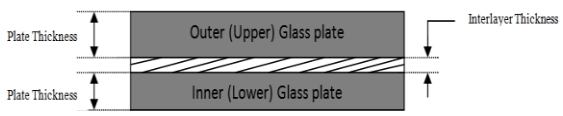

Figure 1: Schematic diagram for the assembly of the glass plates and interlayer.

4.1. Load capacity (force) and absorbed energy:

It is clear from figure 2 that the higher the thickness (number) of interlayer, the less the maximum load capacity of the laminated glass bonded with PVB material for the fixed thickness of the inner glass plate. The same behavior can be observed for the laminated glass bonded with the

 © 2012 Jordan Journal of Mechanical and Industrial Engineering. All rights reserved - Volume 6, Number 2 (ISSN 1995-6665)

same material although the fixed thickness is the thickness of the outer glass plate (Figure 3). The same trends also can be observed for the laminated glass bonded with EVA (Figures 4-5). The trend of these results is in agreement with the shear modulus results reported by Quentt [1], Hooper [2], and the predictions of Zang et al [11]. O the other hand, they contradict with the results of Minor and Reznik [8].

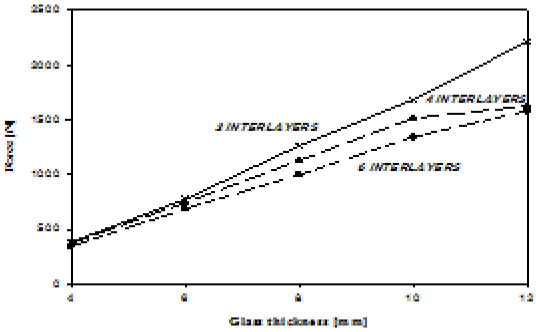

Figure 2: testing the maximum force on (PVB) where the thickness of inner plate was fixed and the outer plate interlayer were changeable.

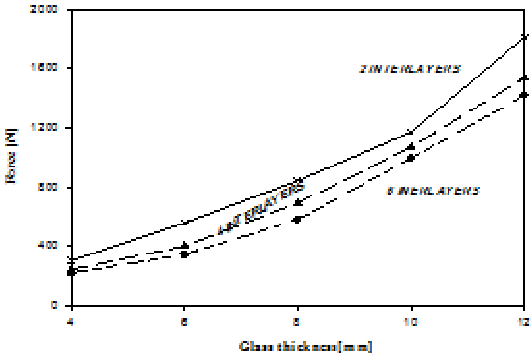

Figure 3: Testing the maximum force on (PVB) laminated glass where the thickness of outer plate was fixed and the inner plate interlayer were changeable.

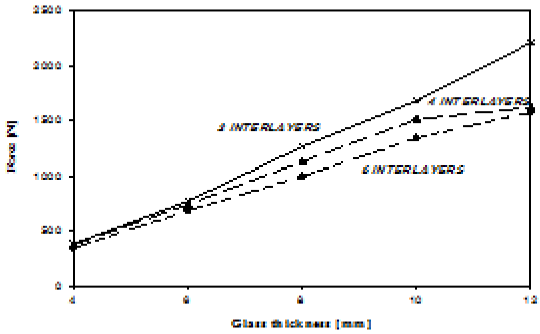

Figure 4: Testing the maximum force on (EVA) laminated glass where the thickness of inner plate was fixed and the outer plate interlayer were changeable.

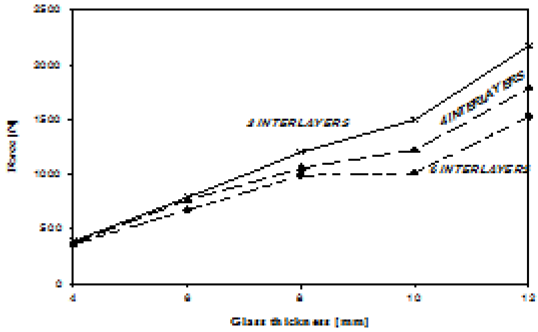

Figure 5: Testing the maximum force on (EVA) laminated glass where the thickness of outer plate was fixed and the inner plate interlayer were changeable.

Figure 6 shows that the position of the plate of the fixed thickness does not affect the maximum load capacity and the maximum load capacity for laminated glasses bonded with EVA is greater than that for the ones bonded with PVB provided that the same conditions are maintained.

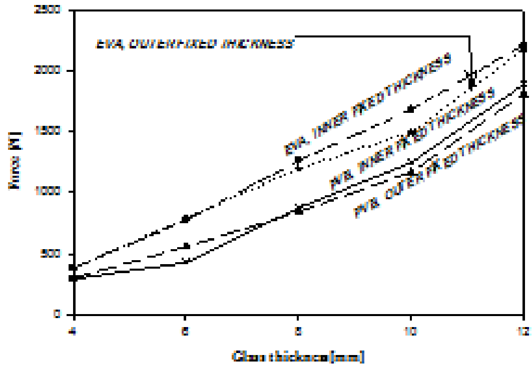

Figure 6: Comparison of the maximum load capacity for the 2 or fixed interlayer thickness, variable bonding material, and different positions of glass thickness.

The absorbed energy shows an opposite effect. For example, Figure 7 shows that the higher the thickness (number) of bonding interlayer, the higher the amount of the absorbed energy. Moreover, the laminated glass which is bonded with PVB absorbs more energy than those bonded with EVA. The trends in these results are in agreement with the results of Keller (2005).

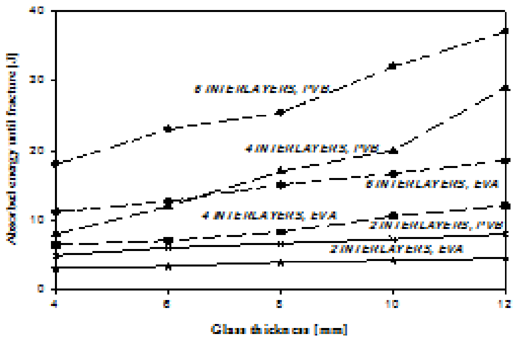

Figure 7: Absorbed energy until fracture by charpy impact test when the inner thickness is variable and the bonding material is PVB and EVA.

An interesting behavior is shown in Figure 2 when the outer thickness of the outer glass is 6 mm. In this case, the maximum load capacity for the 4 interlayer is less than that for the laminated glass bonded with 6 interlayers. Furthermore, the amount of absorbed energy the laminated glass of 4 mm thickness and 6 bonding interlayer of EVA is greater than that for 4 interlayers boded with PVB for the same thickness. These interactions worth more investigations in the future.

4.2. Modeling of the maximum load capacity (force)and the absorbed energy:

The maximum load capacity of glass and its absorbed energy are very important in real life applications. For example, high rise buildings or some open areas are exposed to a high impact wind forces. To be able to find the suitable glass to resist the forces and help in absorbing higher energy, it is of a great importance to select the suitable glass. As it was noticed before, there is a contradiction in the results when comparing the maximum load capacity and the amount of absorbed energy. To overcome this, the modeling took place for the maximum load capacity and the amount of absorbed energy separately depending on the thickness of glass and the thickness of the bonding interlayer regardless the position of glass plates. The modeling of the interaction of the maximum load capacity and the amount of absorbed energy will be considered in our future investigation.

The modeling tool used in this investigation was multiple regressions with the help of minitab software. Four relationships were determined. These are:

- The maximum load capacity as a dependent variable and thickness of glass and the thickness of the PVB bonding interlayer as independent variables.
- The amount of absorbed energy as a dependent variable and thickness of glass and the thickness of the PVB bonding interlayer as independent variables.
- The maximum load capacity as a dependent variable and thickness of glass and the thickness of the EVA bonding interlayer as independent variables.
- The amount of absorbed energy as a dependent variable and thickness of glass and the thickness of the EVA bonding interlayer as independent variables.

The multiple linear regression assumes that the variable response is a linear function of the model parameters and there are more than one independent variable in the model.

The general form of the developed model may be written:

$$y = a + b\,x1 + g\,x2 \tag{1}$$

where

y	: is dependent variable (Max bending force or Max absorbed energy),
a, b, g	: are regression coefficients,
x1, x2	: are the thickness of glass and the interlayer glass thicknesses

After running the minitab software, the results can be summarized as follows:

- The equation that relates the maximum load capacity (y) as a dependent variable and thickness of glass (x1) and the thickness of the PVB bonding interlayer (x2) as independent variables is:

$$\text{Maximum load capacity (PVB)} = -348 + 174\,x1 - 58.3\,x2 \tag{2}$$

The observations, which were described by this relationship, are independent random variable as can be seen on Figure 8 (a) as this figure presents the normal percent probability of the residuals and the plot points lie along a straight line. So, the hypothesized distribution adequately describe data and the model is appropriate. Furthermore, the model explains about 91.5% of the variability of the process because the adjusted R-sq = 91.5%. The analysis of variance of the process shows that the results are extremely significant as the P-value is about zero.

- The equation that relates the amount of absorbed energy as a dependent variable and thickness of glass (x1) and the thickness of the PVB bonding interlayer (x2) as independent variables is:

$$\text{Amount of absorbed energy (PVB)} = -17.4 + 5.12\,x1 + 1.74\,x2 \tag{3}$$

Figure 8 (b) presents the normal percent probability of the residuals and shows that the observations are independent random variable and follow the normal distribution. Moreover, the model explains about 90.3% of the variability of the process because the adjusted R-sq = 90.3%. The analysis of variance of the process shows that the results are extremely significant as the P-value is about zero.

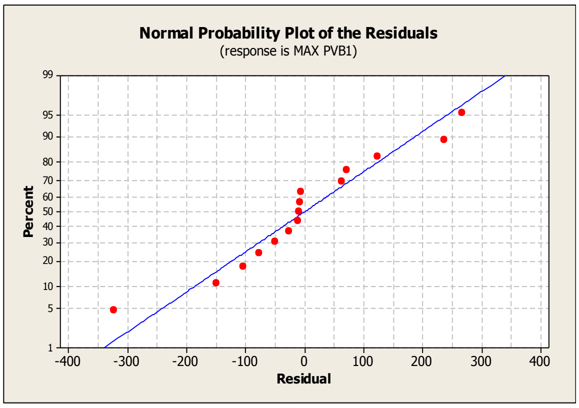

(a)

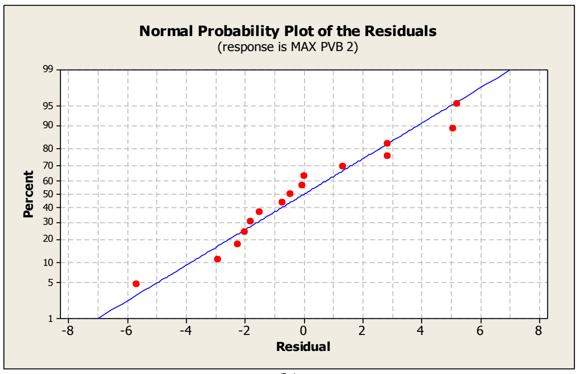

(b)

Figure 8: Normal probability plot of residuals of a) the maximum load capacity relationship and b) amount of absorbed energy for PVB bonding material.

- The equation that relates the maximum load capacity as a dependent variable and thickness of glass (x1) and the thickness of the EVA bonding interlayer (x2) as independent variables is:

$$\text{Maximum load capacity (EVA)} = -88 + 185\,x1 - 68.3\,x2 \qquad (4)$$

Figure 9 (a) presents the normal percent probability of the residuals and shoes that the observations are drawn from independent variables and the standard deviation and the variance of both populations are equal as the plot points shows that the data follows a normal distribution. Also the model explains about 94.7% of the variability of the process because the adjusted R-sq = 94.7%. The analysis of variance of the process shows that the results are extremely significant as the P-value is about zero

- The equation that relates the amount of absorbed energy as a dependent variable and thickness of glass (x1) and the thickness of the EVA bonding interlayer (x2) as independent variables is:

$$\text{Amount of absorbed energy (EVA)} = -6.71 + 2.74\,X1 + 0.620\,X2 \qquad (5)$$

Figure 9 (b) presents the normal percent probability of the residuals. The plot points shows that the process data followed a normal distribution and the observations are independent random variable. Moreover, the model explains about 95.7% of the variability of the process because the adjusted R-sq = 95.7%. The analysis of variance of the process shows that the results are extremely significant as the P-value is about zero.

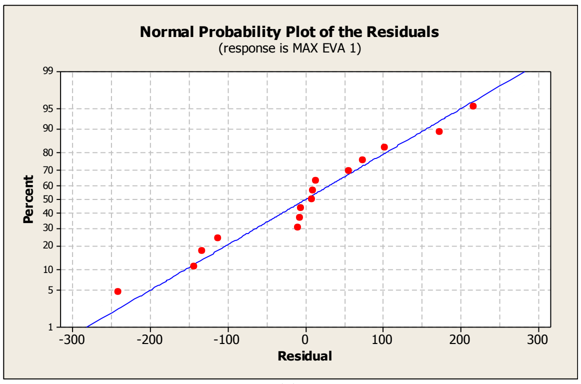

(a)

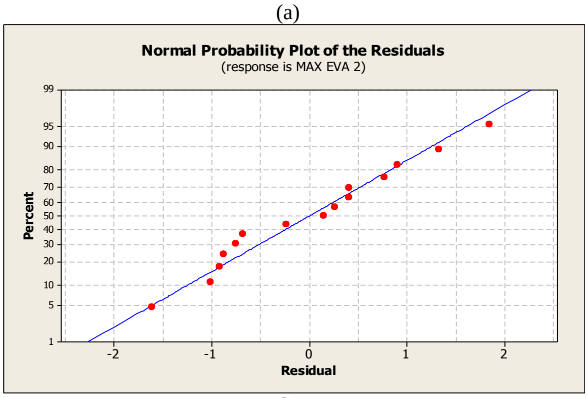

(b)

Figure 9: Normal probability plot of residuals of a) the maximum load capacity relationship and b) amount of absorbed energy for EVA bonding material.

4.3. Failure observation:

Bending test took place until fracture. Then the fractured surface was analyzed. It was found that the propagation of fracture was linear within the glass plate and nonlinear within the bonding polymer as seen in the side view (Figure 10). This difference may be due to the thermoplastic nature of the bonding material which was described by Hooper (1973). The top view in Figure 11 shows the linear nature of propagation within the brittle glass AND Figure 12 shows the failure after Charpy test.

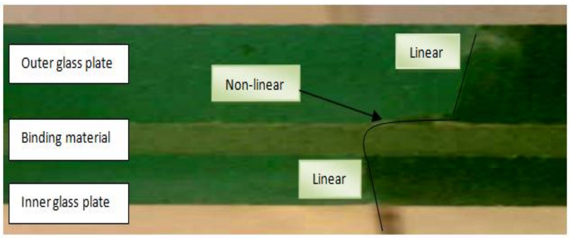

Figure 10: Failure observed after bending test (side view).

Figure 11: Failure observed after bending test (top view).

Figure 12: Failure after Charpy test.

5. Conclusions

The conclusions that can be drawn from this investigation are:

- The higher the thickness (number) of interlayer, the less the maximum load capacity of the laminated glass bonded with PVB material for the fixed thickness of the inner glass plate.
- The higher the thickness (number) of interlayer, the less the maximum load capacity of the laminated glass bonded with EVA material for the fixed thickness of the inner glass plate.
- The position of the plate of the fixed thickness does not affect the maximum load capacity and the maximum load capacity for laminated glasses bonded with EVA is greater than that for the ones bonded with PVB provided that the same conditions are maintained.
- The higher the thickness of bonding (number) interlayer, the higher the amount of the absorbed energy. Moreover, the laminated glass which is bonded with PVB absorbs more energy than those bonded with EVA.
- Regression models were developed to calculate the maximum load capacity and the amount of absorbed energy separately depending on the thickness of glass and the thickness of the bonding interlayer regardless the position of glass plates.
- The propagation of fracture was linear within the glass plate and nonlinear within the bonding polymer.

References

[1] Quenett, R. (1967), The Mechanical Behavior of Laminated Safety Glass Under Bending and Impact Stresses, Forgetragen auf dem DVM-Tag.Wurzburg (Germany), Manuskript-Eing.

[2] Hooper JA (1973), on the bending of architectural laminated glass. International Journal of Mechanical Science, 15, 309-333.

[3] Pilkington, ACI (1971), A Practical and Theoretical Investigation into the Strength of Laminated Glasses Under Uniformly Distributed Loading, Laboratory Report and Discussion, Pilkington ACI Operations Pty. Ltd., pp.206.

[4] Linden MP, Minor JE and Vallabhan CVC (1984), Evaluation of laterally loaded laminated glass units by theory and experiment, Glass Res.And Testing Lab, Texas Tech

[5] Norville, H.S.(1990), Breakage Tests of Du Pont Laminated Glass Units, Glass Research and Testing Laboratory, Texas Tech University, Lubbock, Texas.

[6] Keller Uwe, (2005), Measuring the delaminating energy in laminated safety glass, Proceedings of Glass Processing, Finland , Jun 17-20 2005, 102-104.

[7] Nagalla, S.R., Vallabhan, C.V.G., Minor, J.E., and Norville, H.S. (1985), Stresses in Layered Units and Monolithic Glass Plates, Glass Research and Testing Laboratory, Texas Tech University, Lubbock, Texas, (NTIS Accession No. PB86-142015/AS)

[8] Minor JE and Reznik PL .(1990), failure strengths of laminated glass, J Struct Engrg ASCE,116 (4),1030-1039.

[9] Weller, B. (2005), Experimental Study on Different Interlayer Materials for Laminated Glass, GLASS PROCESSING DAYS 2005 9th, Finland, 386-394.

[10] Behr R A and Kremer PA (1999), Dynamic strains in architectural laminated glass subjected to low velocity impacts from small projectiles, Journal of Materials Science, 34, 5749 – 5756.

[11] Zang M.Y, Lei Z and Wang S. F (2007), Investigation of impact fracture behavior of automobile laminated glass by 3D discrete element method , Springer Verlag 2007.

[12] Belis.J , Depauw.J, Callewaert .D, Delincé and Van Impe. R, (2008) Failure mechanisms and residual capacity of annealed glass/SGP laminated beams at room temperature, Journal of Materials Science, 16, 1866-1875.

JJMIE

Volume 6, Number 2, April 2012
ISSN 1995-6665
Pages 135 - 140

Jordan Journal of Mechanical and Industrial Engineering

A Statistical Analysis of Wind Power Density Based on the Weibull and Ralyeigh models of "Penjwen Region" Sulaimani/ Iraq

S. A. Ahmed[a,]*, H. O. Mahammed[a]

[a]*Faculty of Science and Science Education, School of Science, Dept. of Physics. University of Sulaimani, Iraq*

Abstract

In the present study wind power density of the Penjwen region have been statistically analyzed during the period from January 2001 to December 2003 based on the monthly measured mean wind speed data. The annual and monthly wind speeds and wind density are estimated. The Weibull and Ralyeigh distribution functions have been derived from the available data and both Weibull and Rayleigh probability density functions are fitted to the measured probability distributions on yearly basis, it was shown that the Weibull distribution is fitting the measured monthly probability density distributions better than the Rayleigh distribution for the whole years. The wind power density of this region has been studied based on the Weibull function. Weibull distribution shows a good approximation for estimation of power density.

Keywords: Mean wind speed; Weibull and Rayleigh distribution functions; Wind power density

1. Introduction

Renewable energy sources, wind, solar, geothermal, hydro, biomass and ocean thermal energy have attracted increasing attention from all over the world due to their almost inexhaustible and non-polluting characteristics. Wind energy as one of these important sources is perhaps the most suitable, most effective and inexpensive sources for electricity production as a result, it is vigorously pursued in many countries [1].

Iraq in general and northern region especially has to make use of its renewable resources, such as solar, wind and geothermal energy, not only to meet increasing demand, but also for environmental reasons.

Penjwen region located in the eastern of Sulaimani at 35°37´ N and 45°56´ E and its height above sea level is 1320 meter.

The aim of the present study is to analyze wind speed at Penjwen region due to the important of statistical analysis of wind data to predict the power density in this area and the areas around it.

2. Theoretical Analysis and Formulation

2.1. Vertical extrapolation of wind speed:

Wind speed near the ground changes with height, this requires an equation that predicts wind speed at any height in terms of the measured speed at another height. The most common expression for the variation of wind speed with height is the power law having the following form [2].

$$\frac{v_2}{v_1} = \left(\frac{h_2}{h_1}\right)^{\alpha} \qquad (2\text{-}1)$$

Where v_1 (m/sec) is the actual wind speed recorded at height h_1 (m), and v_2 (m/sec) is the wind speed at the required or extrapolated height h_2 (m). The exponent α depends on the surface roughness and atmospheric stability numerically it lies in the range (0.05 to 0.5).

2.2. Wind speed probability distribution:

The wind speed data in time series format is usually arranged in the frequency distribution format since it is more convenient for statistical analysis, therefore the available time-series data were translated into frequency distribution format [3].

Two of the commonly used functions for fitting a measured wind speed probability distribution in a given location over a certain period of time are the Weibull and Rayleigh distributions. The probability density function of the Weibull of wind speed being v , $f_w(v)$ during any time interval is given, as following [2, 3].

$$f_w(v) = \left(\frac{k}{\alpha}\right)\left(\frac{v}{\alpha}\right)^{k-1} e^{-\left(\frac{v}{\alpha}\right)^k} \qquad (2\text{-}2)$$

Where (m/s) is the Weibull scaling parameter and is the dimensionless Weibull parameter. The shape and scale parameters can be estimated by using the Maximum Likelihood Method (MLH) as [4,5].

* Corresponding author. e-mail: salahaddinahmed@gmail.com

$$k = \left(\frac{\sum_{i=1}^{n} \nu_i^k \ln(\nu_i)}{\sum_{i=1}^{n} \nu_i^k} - \frac{\sum_{i=1} \ln(\nu_i)}{n} \right)^{-1} \quad (2\text{-}3)$$

$$a = \left(\frac{1}{2} \sum_{i=1}^{n} \nu_i^k \right)^{1/2} \quad (2\text{-}4)$$

Where v_i is the wind speed in time stage i and n is the number of non-zero wind data points.

The Ralyeigh $f_R(v)$ distribution is a special case of the Weibull distribution in which the shape parameter k is assumed to be equal to 2. From Equation (2-2) the probability density functions of the Ralyeigh distribution given by [3].

$$f_R(\nu) = \frac{2\nu}{a^2} e^{-\left(\frac{\nu}{a}\right)^2} \quad (2\text{-}5)$$

2.3. Wind power density function:

The evaluation of the wind power per unit area is of fundamental importance in assessing wind power projects, it is well known that the power of the wind at speed V through the blade sweep area A increases as the cube of its velocity and is given by [2,6].

$$P_v = \frac{1}{2} \rho A \nu^3 \quad (2\text{-}6)$$

Where ρ (kg/m^3) is the mean air density, the value 1.069 kg/m^3 is used in this work [7]. This depends on altitude, air pressure and temperature.

The expected monthly or annual wind power density per unit area of a site based on a Weibull probability density function can be expressed as follows[8].

$$P_w = \frac{1}{2} \rho a^3 \Gamma\left(1 + \frac{3}{k}\right) \quad (2\text{-}7)$$

Where Γ is the gamma function and a is the Weibull scale parameter (m/s) given by:

$$P = \frac{V_m}{\Gamma\left(1 + \frac{1}{k}\right)} \quad (2\text{-}8)$$

The two significant parameters k, a are closely related to the mean value of the wind speed V_m .

By extracting a from Equation (2-8) and setting k equal to 2, the power density for the Rayleigh model is found to be [9].

$$P_R = \frac{3}{\pi} \rho V_m \quad (2\text{-}9)$$

Where

$$V_m = a\Gamma\left(1 + \frac{1}{2}\right) \quad (2\text{-}10)$$

The errors in calculating the power densities using the distribution models (Weibull and Rayleigh) in comparison to values of the Probability density distributions derived from measured values can be found using the following formula [2,3].

$$Error\% = \frac{P_{w,R} - P_{m,R}}{P_{m,R}} \quad (2\text{-}11)$$

Where $P_{W,R}$ (w/m^2) is the mean power density calculated from either the Weibull or Rayleigh function used in the calculation of the error, and $P_{m,R}$ is the wind power density for the probability density distribution, derived from measured values which serves as the reference mean power density.

3. Results and Discussion

Data for wind speed in the present calculation were obtained during the period 2001 to 2003 taken from the meteorological directorate center of Sulaimani. The main results obtained from the present study can be summarized as follows.

The monthly mean wind values estimated from the available data for the overall and individual three years are presented in Table (1). It is seen in Table (1) that the highest wind speeds 7.65 m/s occurs in April and June in year 2002. While lowest wind speed 4.88 m/s occur in August in year 2003. The variation of wind speeds often described using the Weibull two-parameter density function. This is statistical method which widely accepted for evaluation local wind local probabilities and considered as a standard approach.

Maximum Likelihood Method was used to calculate bothWeibull's parameters, scale and shape, as shown in Table (1), it is seen from the Table that, while the scale factor varies between 6.19 to 9.73 m/s, the shape factor ranges from 8.84 to 15.00 for location analyzed.

The annual probability density distributions obtained from the Weibull and Rayleigh models were compared to the measured distributions to study their suitability. The annual comparison shows that the Weibull model better than the Rayleigh model to fit the measured probability density distribution as shown in Figure (1), while Figure (2) shows the Weibull distribution of wind speeds all over the data for each year for the studied area.

Table 1: Monthly mean wind speeds, wind power density and the two Weibull parameters (shape and scale).

	Mean Wind Speed (m/sec)			Wind Power Density (w/m²)		
	2001	2002	2003	Weibull	Rayleigh	measured
Jan	**6.43**	**7.13**	**5.91**	**6.49**	**6.51**	**6.30**
Feb	**7.13**	**6.26**	**6.26**	**6.55**	**6.36**	**6.39**
Mar	**7.13**	**6.61**	**5.74**	**6.49**	**6.28**	**6.17**
Apr	**5.56**	**7.65**	**5.74**	**6.32**	**6.57**	**6.21**
May	**7.13**	**6.61**	**6.43**	**6.72**	**6.59**	**6.58**
Jun	**6.26**	**7.65**	**6.09**	**6.67**	**6.80**	**6.52**
Jul	**6.43**	**6.09**	**5.39**	**5.97**	**5.82**	**5.73**
Aug	**7.13**	**6.61**	**4.88**	**6.21**	**5.90**	**5.66**
Sep	**7.13**	**6.43**	**5.39**	**6.32**	**6.05**	**5.92**
Oct	**5.56**	**5.22**	**6.09**	**5.62**	**5.64**	**5.79**
Nov	**7.13**	**5.22**	**7.13**	**6.49**	**6.28**	**6.63**
Dec	**6.26**	**5.22**	**6.26**	**5.91**	**5.80**	**5.99**
Shape	**15**	**8.84**	**11.01**			
Scale	**6.86**	**6.75**	**6.19**			

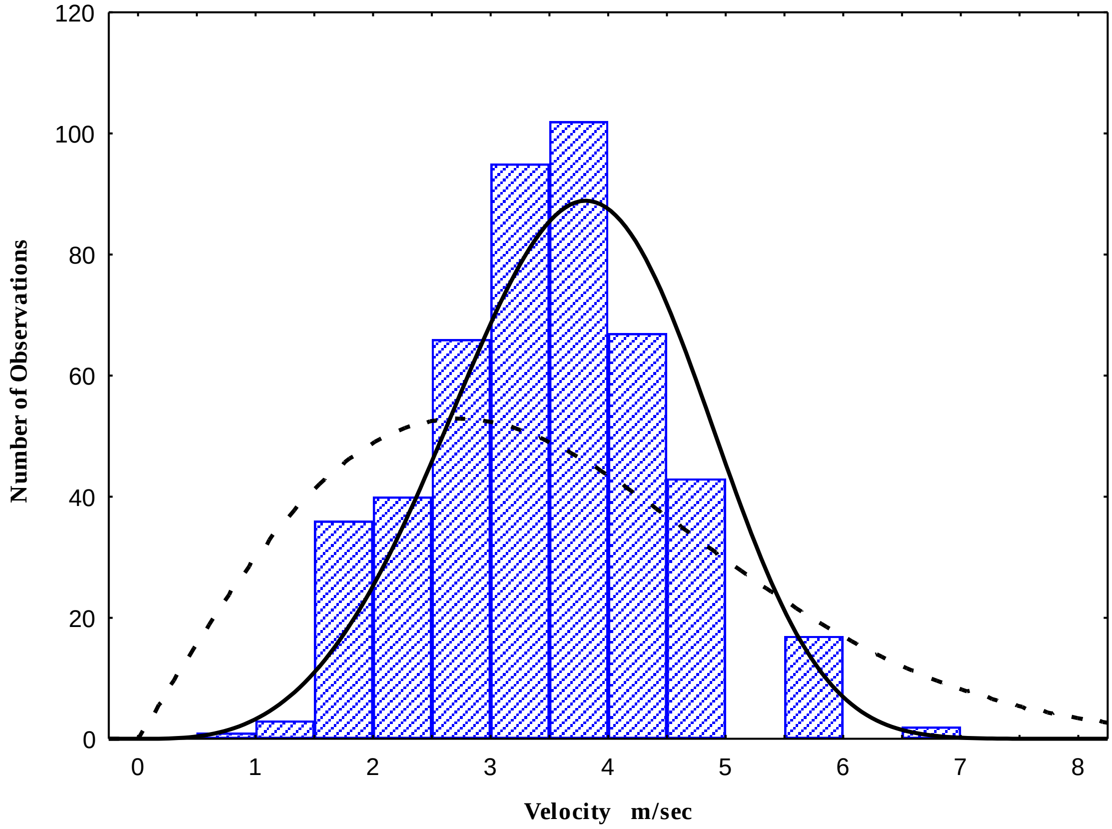

Figure 1: Weibull and Rayleigh comparisons of the actual probability distribution of the wind.

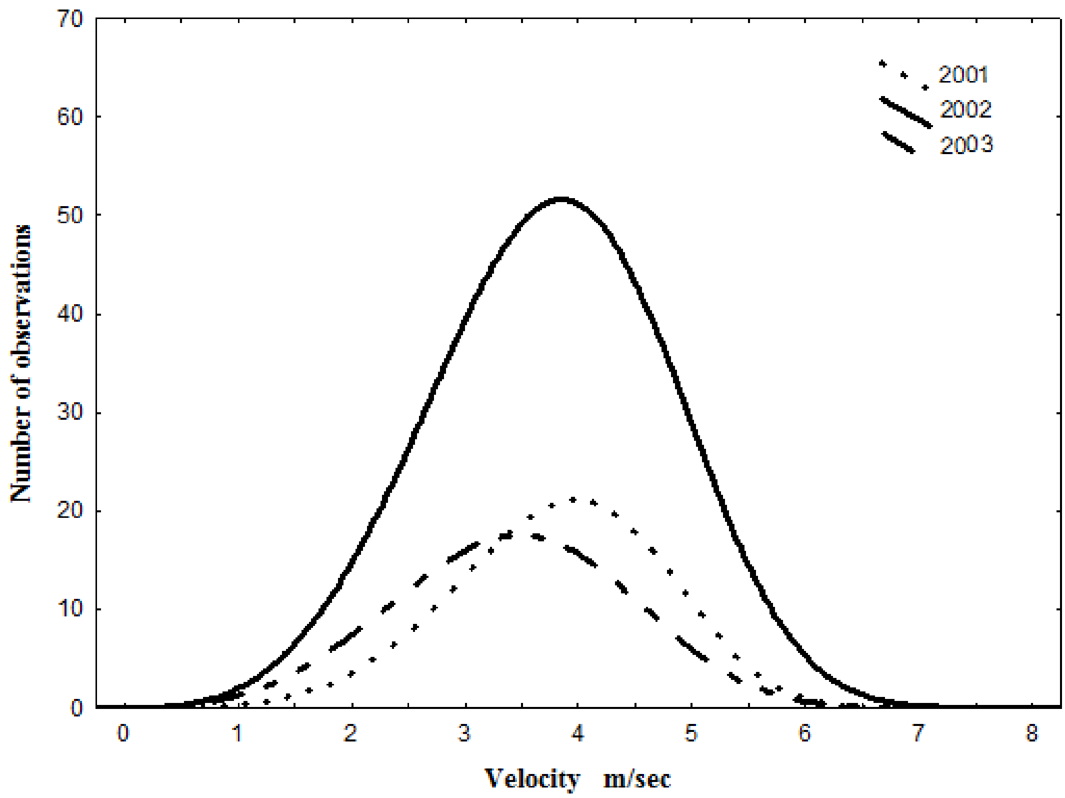

Figure 2: Yearly Weibull probability density distribution of each year for the period of (2001- 2003).

The power densities calculated from the measured probability density distribution and those obtained from the models are shown in Figure (3). The power density shows a large month to month variation, the minimum power densities occur in the February and September (2003) with 14.55 and 14.45 w/m^2 respectively, it is interesting to note that the highest power density value occur in the Spring and Summer months of March, May (2002) and May, July (2001) with the maximum value of (53.49, 53.12) and (54.87, 50.83) w/m^2 respectively. The power densities in the remaining moths are between these two groups of low and high as shown in Figure (4).

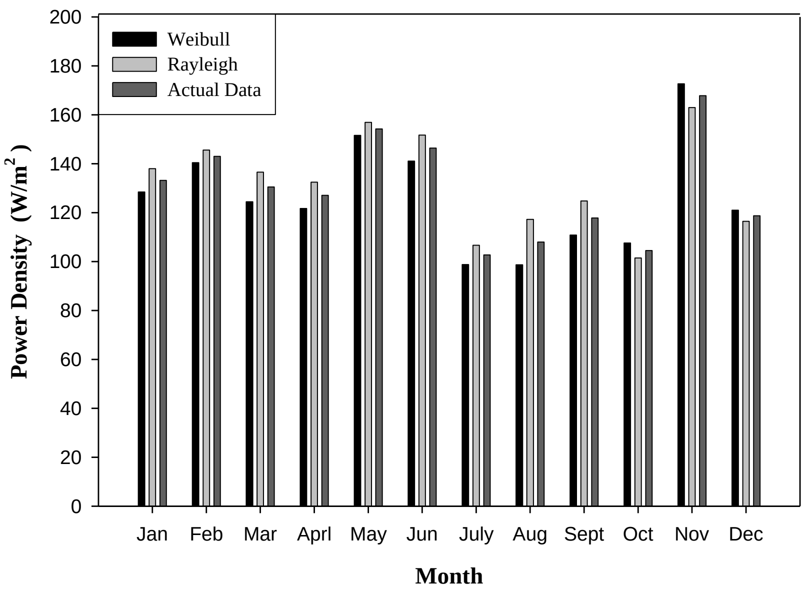

Figure 3: Wind power density obtained from the actual data versus those obtained from the Weibull and Rayleigh models on a monthly basis.

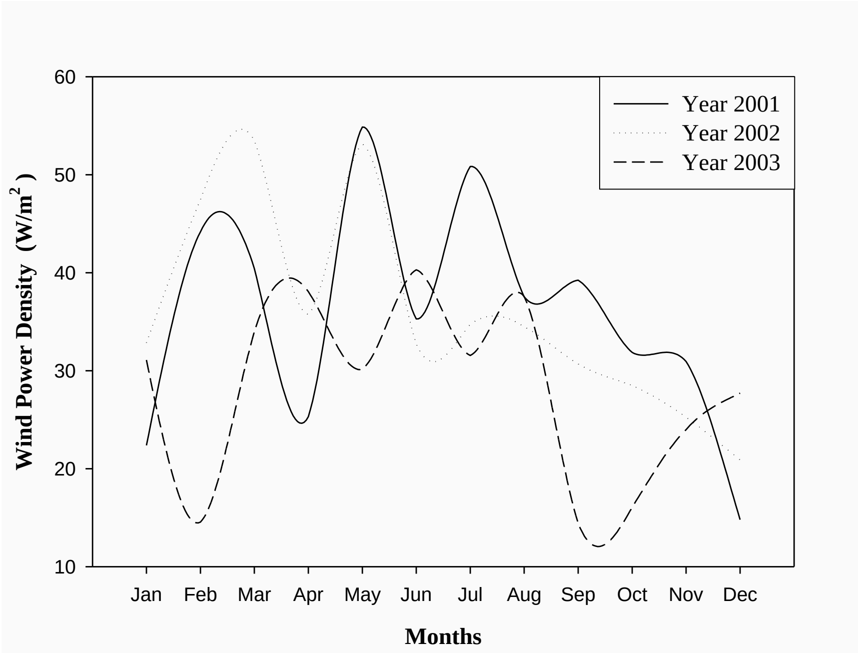

Figure 4: Monthly Weibull probability density distribution for the period of 2001- 2003 for the studied area.

Errors in calculating the power densities using the distributions (Weibull and Rayleigh models) in comparison to those using the measured probability density distributions are presented in Figure (5). The highest error values occur in August and September with 9.27% and 6.96% for the Weibull model respectively, the power density as estimated by the Weibull model has a very small error value 2.59% in February. The monthly analysis shows that the highest error value using the Rayleigh model occur in November with 4.86%, whereas the smallest error in the power density calculation using Raleigh model is 2.28% in December.

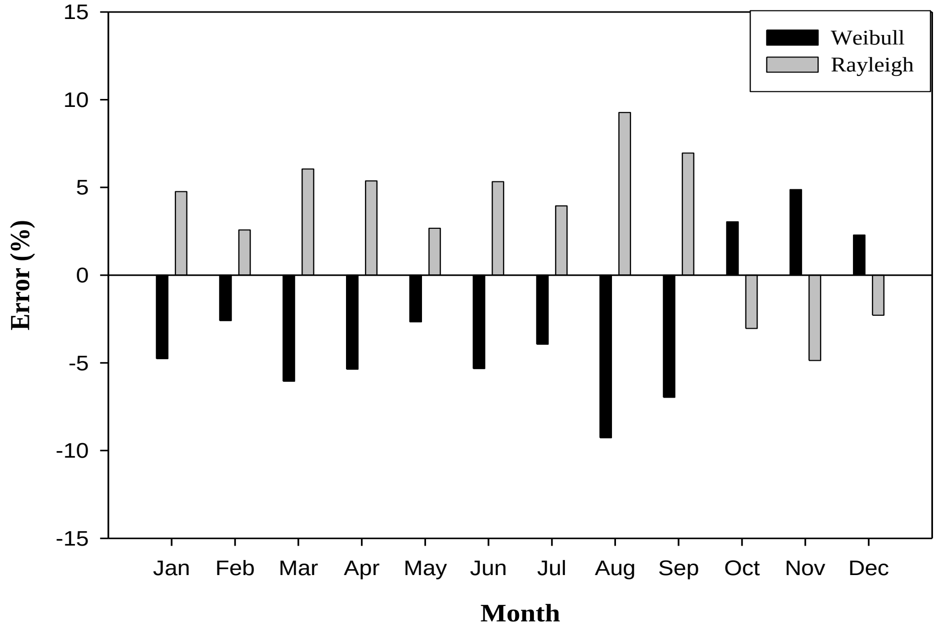

Figure 5: Error values in calculating the wind power density on monthly basis obtained from the Weibull and Rayleigh models in reference to the wind power density obtained from the measured data.

4. Conclusions

Wind characteristics of Penjwen have been analyzed statistically, wind speed data were collected for a period of three years (2001-2003). The probability density distributions and power density distributions were derived from the time series data. Two probability density functions have been fitted to the measured probability distributions on a monthly basis, based on the Weibull and

Rayleigh models. The most important outcomes of the study can be summarized as follows:

- The Weibull distribution is fitting the measured monthly probability density distributions better than the Rayleigh distribution for the whole years.
- The Rayleigh distribution provides better power density estimations in nine months than the Weibull distribution.
- The yearly average error values in calculating the power densities using the distributions in comparison to those using the measured probability density distributions shows a large month to month variation due to the difference of the shape parameters.

References

[1] Mahyoub H.Albuhairi, "Assessment and Analysis of Wind Power density in Taiz –Republic of Yemen"Ass.Uni.Bull.Environ.Res.Vol9,No.2,pp, 13-21, October, 2006.

[2] Mahyoub H.Albuhairi, "A Statistical Analysis of Wind Speed Data and an Assessment of Wind Energy Potential in Taiz-Republic of Yemen", Ass.Uni.Bull.Environ.Res.Vol9, No.2, pp 21-33, Oct.2006.

[3] Ali Naci Celik,"A Statistical Analysis of Wind power Density Based on The Weibull and Rayleigh Models at the southern Region of Turkey" Renewable Energy Vol.29, pp 593-604,2003.

[4] Zaid Hatahet, "Wind Data Analyzer" 2006, www.hatahet.net.

[5] S. Mathew , "Wind Energy" (2006),Electric Edition , Springer (NL).

[6] Wei zhou, Hongxing Yang, Zhaohong Fang, "Wind Power Potential and Characteristic Analysis of the Pearl River Delta Region, China" Renewable Energy Vol.31, (2006), pp 739-753.

[7] Salahaddin A. Ahmed, "Wind Analysis and Distribution of Wind Energy Potential over Iraqi Kurdistan Region" 2009, PhD Thesis, Univ. of Sulaimani Coll. of Science. O.A.Jaramillo, R. Saldana, U. Miranda, "Wind Power Potential of Baja California Sur, Mexico " Renewable Energy Vol.29,(2004),pp 2087-2100.

[8] Adrian Ilinca, Ed McCarthy, Jean-Louis Chaumal, Jean-Louis Retiveau Renewable Energy Vol.28, (2003), pp 1881-189.

JJMIE

Volume 6, Number 2, April 2012
ISSN 1995-6665
Pages 141 - 145

Jordan Journal of Mechanical and Industrial Engineering

Analysis of Hoisting Electric Drive Systems in Braking Modes

K. A. Khandakji[a,]*

[a]Department of Electrical Engineering, Tafila Technical University P.O. Box 179, Tafila 66110, Jordan

Abstract

Braking in hoisting drives is used to reduce the speed of the load (cargo) or to stop it completely. Braking can be realized using electrical and mechanical means; mechanical brake is used to hold the suspended cargo after disconnecting the driving motor from the supply. In modern hoisting electric drive systems, in addition to mechanical braking, electric braking is also used. Electric braking can be realized by transforming the driving electrical motor into the braking mode. The dynamic loads created in the mechanical parts of the hoisting drive depend on the magnitude of the braking torque, load torque, motor speed and other parameters. In this paper a mathematical analysis of the factors on which the braking process depend are analyzed. Recommendations about the appropriate braking methodology by which dynamic loads can be minimized are brought out. A mathematical model of the proposed hoisting electric drive is developed.

Keywords: Hoisting drives; Braking mode; Dynamic loads; Induction motor

1. Introduction

Safety and control is crucial in all crane applications. Operating cranes demand precision and leave no margin for errors. The critical starting and stopping can lead to harmful jerks and false tripping, not to mention accidental dropping of the load. Safety for both people and load is of the outmost importance in crane operation.

Optimizing the operation of the crane is also essential. Minimizing cycle time improves productivity. There are also great savings to be made from extended equipment lifetime and more reliable operation without unplanned stops and downtime. In hoisting motor-drive systems, a torsional vibration is often generated due to the presence of an elastic element in torque transmission. Such a mechanical system is modeled as a two-mass system. In such system, vibration suppression of a low inertia ratio, i.e. when the motor inertia is larger than the load inertia is very difficult. Such a problem was and still a crucial issue for many researchers [1-14]. In this research, an approach to find the maximum loads (torque) created in the elastic elements (ropes) of the electromechanical hoisting system at braking and give recommendations for minimizing these dynamic loads.

2. Design Considerations And Mathematical Representation

In cranes, the braking torque required for holding the suspended nominal cargo $T_{br(nom)}$ can be calculated as follows:

$$T_{br(nom)} = K_s \cdot T^{\downarrow}_{L(nom)} \qquad (1)$$

Where;

K_s- Safety coefficient, K_s=1.5 - 2.5,

$T^{\downarrow}_{L(nom)}$ – Nominal load (cargo) torque at lowering, referred to the motor's shaft,

$$T^{\downarrow}_{L(nom)} = T_{L(nom)} \cdot \eta_{nom} \qquad (2)$$

$T_{L(nom)}$ - Nominal load (cargo) torque, referred to the motor's shaft.

η_{nom} - Nominal efficiency coefficient of the mechanism.

Typically, hoisting mechanisms can be physically modeled as two-mass electromechanical systems. Here the first mass (inertia) J_1 represents the equivalent inertia of the motor rotor and all elements rotating on the motor shaft with speed ω_1 including the brake drum, coupling, etc. On the other hand the second inertia J_2 represents the equivalent inertia of the suspended cargo and all elements moving with and at common speed ω_2 to the cargo. The motion is transferred from J_1 to J_2 via ropes with a stiffness coefficient C_{12}. It is obvious, for analysis, that both J_2 and C_{12} are referred to the motor shaft.

The braking torque T_{br} in general is a function of time, motor speed ω_1 and other parameters; it can be realized by mechanical brake or electrically by transferring the motor into braking mode.

* Corresponding author. e-mail: drkhandakji@yahoo.com

The basic equations describing the braking process at lowering:

$$T_{\mathrm{br}} - T_{\mathrm{el}} = J_1 \frac{d^2\varphi_1}{dt^2} \tag{3.1.}$$

$$T_{\mathrm{el}} - T_{\mathrm{L}}^{\downarrow} = J_2 \frac{d^2\varphi_2}{dt^2} \tag{3.2.}$$

Where

$T_{\mathrm{el}} = C_{12}(\varphi_1 - \varphi_2)$ - Elasticity torque induced in the elastic elements,

φ_1, φ_2 - The angle of rotation of the first mass and the second, respectively.

For calculation, the speed of both masses is assumed to be negative at lowering, and positive at lifting respectively, i.e.:

$\omega_1 = \frac{d\varphi_1}{dt}$ <0 and $\omega_2 = \frac{d\varphi_2}{dt}$ <0 at lowering,

$\omega_1 = \frac{d\varphi_1}{dt}$ >0 and $\omega_2 = \frac{d\varphi_2}{dt}$ >0 at lifting.

Assuming the braking process at lowering can be accomplished only when $T_{br} > T_L^{\downarrow}$, equations 3 can be used for the given process until the motor's speed $\omega_1 \neq 0$, the braking torque is also assumed constant over the braking process and does not depend on the motor's speed (Figure 1).

Dividing (3.1) by J_1 and (3.2) by J_2 and subtracting 3.2 from 3.1 after division we get:

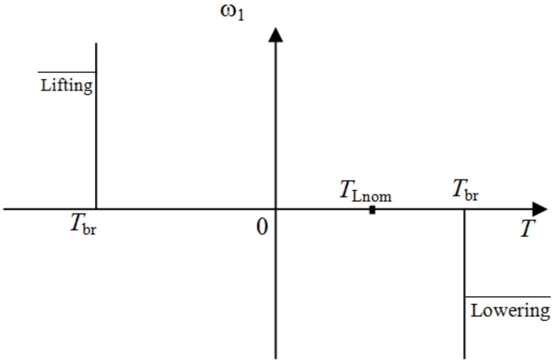

Figure 1: Speed-torque diagram of the hoisting drive with constant braking torque.

$$\frac{1}{J_1} T_{\mathrm{br}} - \left(\frac{1}{J_1} T_{\mathrm{el}} + \frac{1}{J_2} T_{\mathrm{el}} \right) + \frac{1}{J_2} T_{\mathrm{L}} = \frac{d^2(\varphi_1 - \varphi_2)}{dt^2} \tag{4}$$

Multiplying (4) by the stiffness coefficient C_{12} we get

$$T^2 \frac{d^2 T_{el}}{dt^2} + T_{el} = \frac{T_{br} J_2 + T_L J_1}{J} \tag{5}$$

Where

$J = J_1 + J_2,$

$T = \frac{1}{\Omega}$, Ω - The frequency of oscillations of the second-order system.

If the losses in the ropes due to deformation are neglected, then the ropes elasticity torque is

$T_{\mathrm{el}} = C_{12}(\varphi_1 - \varphi_2)$.

The solution of (5) can be found in the following form

$$T_{\mathrm{el}} = \frac{T_{\mathrm{br}}}{\gamma_2} + \frac{T_{\mathrm{L}}}{\gamma_1} + A \sin \Omega t + B \cos \Omega t \tag{6}$$

Where

$$\gamma_1 = \frac{J}{J_1}, \quad \gamma_2 = \frac{J}{J_2}.$$

A, *B*- constants that can be found from the initial conditions of braking, the speed of both masses is equal, i.e. $\omega_1 = \omega_2$, and the elasticity torque equals the load torque, thus substituting in (6), (when t = 0, $\omega_1 = \omega_2$ and $T_{\mathrm{el}} = T_{\mathrm{L}}$) we get

$$T_{el} = T_{\mathrm{L}} + \frac{T_{\mathrm{br}} - T_{\mathrm{L}}}{\gamma_2} (1 - \cos \Omega t) \tag{7}$$

The time at which the periodic oscillations of the elasticity torque will have maximum value is

$$t_{\mathrm{m}} = (2n - 1) \frac{\pi}{\Omega} \tag{8}$$

Where n=1, 2, 3 … - the number of the period.

Respectively the maximum value of the elasticity torque at the half of the first period (n=1) is

$$T_{\mathrm{el\ max}} = T_{\mathrm{L}} + \frac{2(T_{\mathrm{br}} - T_{\mathrm{L}})}{\gamma_2} \tag{9}$$

The ratio between the maximum instantaneous $T_{\mathrm{el\ max}}$ and the maximum calculated $T_{\mathrm{el\ mc}}$ (by design) elasticity torque value is expressed by the coefficient K_{d}

$$K_{\mathrm{d}} = \frac{T_{\mathrm{el\ max}}}{\mathrm{T}_{\mathrm{el\ mc}}},$$

Where

$$T_{\mathrm{el\ mc}} = \frac{T_{\mathrm{m}} - T_{\mathrm{L}}^{\uparrow}}{\gamma_2} + T_{\mathrm{L}}^{\uparrow},$$

Where T_{m} -The motor's torque.

Usually in cranes design $T_m = 2T^{\uparrow}_{L\,nom}$ and $T^{\uparrow}_{L} = T^{\uparrow}_{L\,nom}$, thus;

$$T_{el\ mc} = \frac{T_L^{\uparrow}}{\gamma_2}(\gamma_2 + 1) \tag{10}$$

Substituting (9) and (10) in K_d, we get

$$K_d = \left[1 + \frac{2K_{br} - 3}{\gamma_2 + 1}\right]\eta^2_{nom} \tag{11}$$

Where

$$K_{br} = \frac{T_{br}}{T_L^{\downarrow}}$$

Equation (11) shows that when $K_{br} \leq 1.5$, Kd<1. This means that at breaking, the maximum load created in the rope at lowering will be less than that at lifting. It shows also, that when K_{br}=1.5, K_d does not depend on γ_2 and the less is K_d, the less will be η_{nom}.

Coefficient K_{OL} shows the ratio between the maximum instantaneous elasticity torque value and the load torque value:

$$K_{OL} = \frac{T_{el\ max}}{T_L^{\downarrow}} = 1 + \frac{2(K_{br} - 1)}{\gamma_2} \tag{12}$$

Equations (9-12) are used to estimate the dynamic loads created in the links of the mechanical part of the hoisting drive, that should not exceed 150% of the steady-state load value. On the other hand K_d practically should not exceed 1.25.

3. Simulation and Results

In order to find expressions for the speed $\omega_1(t)$ and $\omega_2(t)$, (7) should be substituted in (3.1) and 3.2, then integrating both equations and substituting the value of the initial speed for both masses to be the nominal value ω_{nom} we get:

$$\omega_1 = -\omega_{nom} + \frac{T_{br} - T_L}{J}t + \frac{T_{br} - T_L}{J\Omega}\frac{J_2}{J_1}\sin\Omega t \tag{13}$$

$$\omega_2 = -\omega_{nom} + \frac{T_{br} - T_L}{J}t - \frac{T_{br} - T_L}{J\Omega}\sin\Omega t \tag{14}$$

As in hoisting drives $J_1 > J_2$ then the amplitude of the speed $\omega_1(t)$ should be less that one of $\omega_2(t)$. After braking $\omega_1(t)$ will reach zero after a finite time which can be found from (13) by substituting $\omega_1(t) = 0$ we get:

$$\frac{T_{br} - T_L}{J}\left(t + \frac{J_2}{J_1\Omega}\sin\Omega t\right) = \omega_{nom}.$$

After the motors speed reaches zero, the braking torque will be assumed to be infinity ($T_{br} = \infty$) and the motor's speed will remain zero. The results of simulation for the braking process at lowering the nominal load (3 ton) for a particular crane are depicted in Fig. 2 (a and b).

The analysis of the obtained simulation results for different hoisting drives conducted elsewhere but omitted for brevity, revealed that the sudden intensive braking of hoisting drives at lowering the nominal load with the nominal speed does not lead to impermissible loading in the elastic links of the mechanism like ropes.

The braking process at lifting with a constant braking torque (T_{br}) is also simulated using the following equations:

$$-T_{br} - T_{el} = J_1\frac{d^2\varphi_1}{dt^2} \tag{15.1}$$

$$T_{el} - T_L^{\uparrow} = J_2\frac{d^2\varphi_2}{dt^2} \tag{15.2}$$

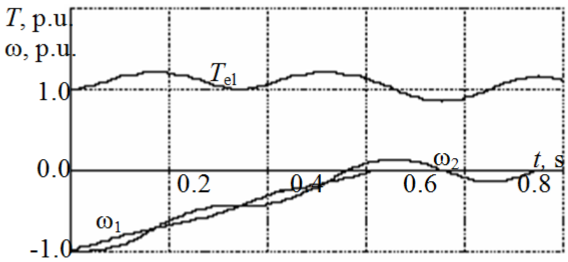

a) K_{br} = 1.5

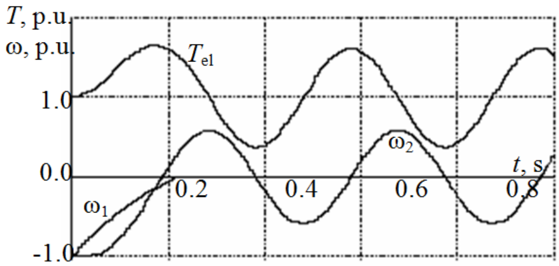

b) K_{br} = 2.5

Figure 2: Braking transient at lowering the nominal load with two different braking torque values.

At lowering the nominal load which corresponds to T_{Lnom}, the motor's torque required for lowering the nominal load $T^{\downarrow}_{L(nom)}$ was calculated using (2), while at lifting the same nominal load, the motor's torque is calculated using the following equation:

$$T^{\uparrow}_{L\,nom} = \frac{T_L}{\eta_{nom}} \tag{16}$$

The solution for the differential equations (15.1) and (15.2) substituting the initial conditions (when t = 0, $\omega_1 = \omega_2$, $T_{el} = T_L$

and $\frac{dT_{el}}{dt} = 0$) is:

$$T_{el} = T_L - \frac{T_{br} + T_L}{\gamma_2}(1 - \cos\Omega t) \tag{17}$$

The minimum value of the elasticity torque at lifting can be found by substituting $t = t_m = (2n-1)\frac{\pi}{\Omega}$, (found in (8) in (17)):

$$T_{el\ min} = T_L - \frac{2(T_{br} + T_L)}{\gamma_2} \quad (18)$$

An expression for the speed of the first mass can be found by solving (15.1) taking into account (17):

$$\omega_1 = \omega_{nom} - \frac{T_{br} + T_L}{J} t - \frac{T_{br} + T_L}{J\Omega} \frac{J_2}{J_1} \sin \Omega t \quad (19)$$

Respectively for the speed of the second mass

$$\omega_2 = \omega_{nom} - \frac{T_{br} + T_L}{J} t + \frac{T_{br} + T_L}{J\Omega} \sin \Omega t \quad (20)$$

At the first stage of braking, when the motor's speed $\omega_1 = 0$, the mechanism is to be considered as a one-mass system, thus

$$T_{el} - T_L = J_2 \frac{d^2 \varphi_2}{dt^2} \quad (21)$$

After a complete stop of the motor, the initial conditions for the formed single-mass system are:
$T_{el} = T_{el\ min}$ defined in (18), $\omega_2 = \omega_1 = 0$.

The solution of (21) is:

$$T_{el} = T_L - 2\frac{T_L - T_{br}}{\gamma_2} \cos \Omega_2 t \quad (22)$$

The maximum value of T_{el} will occur when $\Omega_2 t = \pi$, thus

$$T_{el\max} = T_L + \frac{2(T_{br} + T_L)}{\gamma_2} \quad (23)$$

For this case $K_d = \dfrac{2\left(T_{br} + 2T_L^{\uparrow}\right) + \gamma_2 T_L^{\uparrow}}{T_L^{\uparrow}(\gamma_2 + 1)}$.

After affecting some mathematical rearrangements and substituting $T_L^{\downarrow} = T_L^{\uparrow}\eta^2$, K_d can be rewritten in the following form

$$K_d = 1 + \frac{2K_{br}\eta_{nom}^2 + 1}{\gamma_2 + 1} \quad (24)$$

K_{OL} for this case will be

$$K_{OL} = \frac{T_{el\max}}{T_L^{\uparrow}} = 1 + \frac{2\left(K_{br}\eta_{nom}^2 + 1\right)}{\gamma_2} \quad (25)$$

Simulations of the braking process at lifting were made for the same 3-ton hoisting capacity crane. The results of simulation revealed that assuming similar conditions (the load weight, braking torque, motor's speed, etc.) at lifting and lowering, the dynamic loads created in the elastic elements (ropes) are greater at lifting.

As seen from (17), (19) and (20) the maximum value of the elasticity torque can occur at finite initial conditions of the braking mode at lifting, particularly, there is a finite value of the oscillations frequency at which the elasticity torque has maximum value. Substituting the time at which T_{el} will have maximum magnitude $t_m = \frac{\pi}{\Omega}$ in (19) and equating (19) to zero, the frequency at which T_{el} will have maximum can be found as follows:

$$\Omega_m = \frac{T_{br} + T_L}{\omega_{nom} J} \pi \quad (26.1)$$

The frequency of the vibrations induced in the two-mass system depends on the stiffness coefficient C_{12} of the ropes and the moment of inertia of the first and the second mass (J_1 and J_2):

$$\Omega = \sqrt{\frac{C_{12} J}{J_1 J_2}} \quad (26.2)$$

Assuming J_1 and J_2 to be constant for the hoisting drive, a value of C_{12m} (which corresponds to the maximum frequency found in (26)) can be found by substituting $\Omega = \Omega_m$ in (26.2):

$$C_{12m} = \frac{\pi^2 (T_{br} + T_L)^2}{J\gamma_1\gamma_2\omega_{nom}^2} \quad (27)$$

As the stiffness coefficient of the ropes $C_{12} = \frac{a}{l}$, where a- is a constant that depends on the material and the cross-sectional area of the rope, l- is the length of the rope, therefore a finite value of the rope length l_m that corresponds to C_{12m} as follows: (Assuming $\pi^2 \cong 10$)

$$l_m = 0{,}1\, a \frac{J\gamma_1\gamma_2\omega_{nom}^2}{(T_{br} + T_L)^2} \quad (28)$$

If the braking process with finite J, T_{br} and T_L occurs at a ropes length l_m, then the ropes will be exposed to maximum elasticity torque, but l_m can have values which maybe unreal for a certain drive.
The change in the cargo (load) weight will result in a change in the moment of inertia of the second mass of the two-mass mechanical system, thus γ_2 will also vary. The effect of the change of γ_2 on the dynamic loads induced in the ropes at braking at lifting the nominal load (at the nominal hoisting speed assuming critical ropes length l_m) is shown in Fig. 3.

Analysis of the curves depicted in Fig. 3 shows that for mechanisms with relatively low J_2 (γ_2 >20), braking can be accomplished using pure mechanical brake without exposing the ropes to impermissible elasticity torque values (K_d =1.15-1.2). On the other hand, mechanical brake can cause harmful deformation in ropes for mechanisms with γ_2 <10 at possible ropes length value (K_d >1.3 at K_{br} = 1.5). Higher values of K_d are possible at K_{br} = 2.5 but with unreal ropes length values.

The braking process at lifting the nominal load at the nominal speed with different braking torque values and ropes length was simulated; the results of simulation are depicted in Fig. 4 and Fig.5.

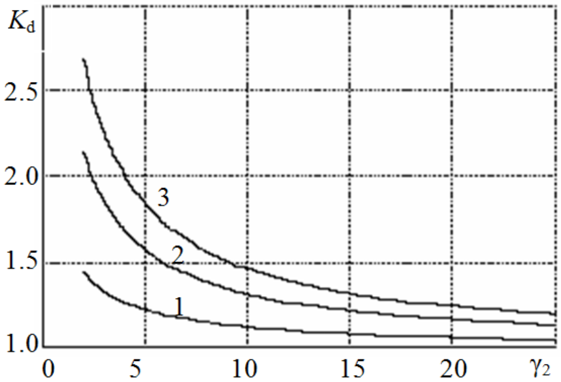

Figure 3: The relationship between K_d and γ_2 for the braking process at lifting the nominal load with different braking torque values (1-K_{br}=0.2; 2-K_{br}=1.5; 3-K_{br}=2.5).

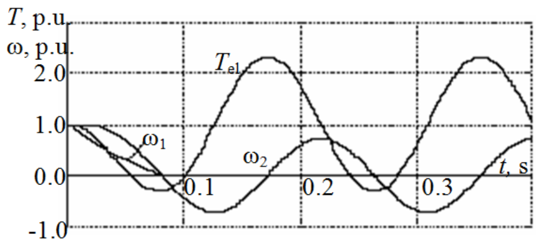

Figure 4: Simulation of the braking process at lifting the nominal load (3 ton). K_{br}=2.5, l=l_m=5.5m.

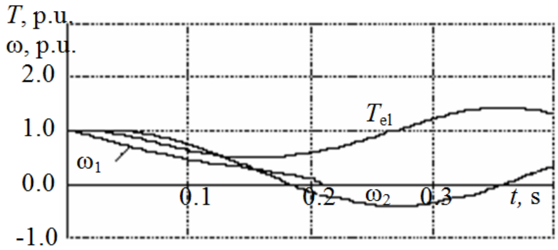

Figure 5: Simulation of the braking process at lifting the nominal load (3 ton). K_{br}=0.2, l=20m, l_m=37m.

The results of simulation of the above mentioned braking transient revealed that the use of the intensive mechanical brake with K_{br} = 2.5 (Fig. 4) will create impermissible dynamic elasticity torque in the ropes (K_d = 1.9), while the braking with a relatively reduced braking torque (Fig. 5) by the use of other braking means like electrical, does not expose ropes to impermissible dynamic elasticity torque (K_d = 1.2), but the transient time will be increased. Mechanical brake is recommended to be used only when the motors speed is decreased to values less than 0.1 of the rated value.

4. Conclusion

In this research study the braking transient of the hoisting electric drive systems was studied, the main parameters on which the elasticity torque induced in the ropes depends are defined. Equations for the calculating the maximum elasticity torque at braking with constant braking torque in lowering and lifting are derived. Analysis revealed that the maximum dynamic elasticity torque at lifting may be of a grater value than at lowering. For mechanisms with γ_2 < 15…20, the magnitude of the induced dynamic elasticity torque at braking is increased. Formulae for calculating the stiffness coefficient of the ropes and respectively the ropes length at which the maximum induced dynamic elasticity torque at braking occur are derived. Mechanical braking of hoisting mechanisms which have K_d>1.5-1.6 is not recommended, it is more rational to brake such mechanisms by transforming the electrical motor into braking mode, mechanical brake is recommended to be used only when the motors speed is less than 0.1 of the rated value.

References

[1] Kamal Khandakji, "Vibration Control of Two-Mass Mechatronic System with Low Inertia Ratio". *International Journal of Automation and Control.* May 2009, Vol. 3 Issue 4, pp 352-362.

[2] Orlowska-Kowalska Teresa and Szabat Krzysztof, "Neural-Network Application for Mechanical Variables Estimation of a Two-Mass Drive System". *IEEE Transactions on Industrial Electronics*; Jun. 2007, Vol. 54 Issue 3, pp 1352-1364.

[3] Kyo-Beum Lee and Frede Blaabjerg, "An Improvement of Speed Control Performances of a Two-Mass System Using a Universal Approximator". *Electrical Engineering*; May 2007, Vol. 89 Issue 5, pp 389-396.

[4] Orlowska-Kowalska Teresa and Szabat Krzysztof, "Control of the Drive System with Stiff and Elastic Couplings Using Adaptive Neuro-Fuzzy Approach". *IEEE Transactions on Industrial Electronics*; Feb. 2007, Vol. 54 Issue 1, pp 228-240.

[5] Mikhlin Yu. V and Reshetnikova S. N, "Dynamic Analysis of a Two-Mass System with Essentially Nonlinear Vibration Damping". *International Applied Mechanics*; Jan2005, Vol. 41 Issue 1, pp 77-84.

[6] Kamal Khandakji and Kosmas Zdrozis, "Determination of Quality Parameters of Hoisting Electric Drive Systems With 3-Phase Induction Motors". Proc. 5th International Conference on Technology and Automation; Oct. 2005, pp. 294-296.

[7] Matthias Feiler, Christian Westermaier and Dierk Schroeder, "Adaptive Speed Control of a Two-Mass System". *IEEE Conference on Control Applications*, Istanbul, 2003.

[8] Cveticanin L, "Vibrations of a Free Two-Mass System with Quadratic Non-Linearity and a Constant Excitation Force". *Journal of Sound & Vibration*; Feb. 2004, Vol. 270 Issue 1/2, pp 441-450.

[9] Gallina P. and Trevisani A, "Delayed Reference Control of a Two-Mass Elastic System". *Journal of Vibration & Control*; Jan. 2004, Vol. 10 Issue 1, pp 135-159.

[10] Cveticanin L, "Forced Non-Linear Vibrations of a Symmetrical Two-Mass System". *Journal of Sound & Vibration*; Aug. 2003, Vol. 265 Issue 2, pp 451-459.

[11] Peter Karsten, Scholing Ingo and Orlik Bernd, "Robust Output-Feedback H∞ Control with a Nonlinear Observer for a Two-Mass System". *IEEE Transactions on Industry Applications*; May/Jun. 2003, Vol. 39 Issue 3, pp 637-645.

[12] Cveticanin L, "The Motion of a Two-Mass System with Non-Linear Connection". *Journal of Sound & Vibration*; Apr2002, Vol. 252 Issue 2, pp 361-370.

[13] Chernous'ko F.L, "The Optimum Rectilinear Motion of a Two-Mass System". *Journal of Applied Mathematics & Mechanics*; Jan. 2002, Vol. 66 Issue 1, pp 1-8.

[14] Morimoto Shigeo, Hamamoto Akira and Takeda Yoji, "Vibration Control of Two-Mass System with Low Inertia Ratio Considering Practical Use". *Electrical Engineering in Japan*; Nov. 1998, Vol. 125 Issue 2, pp 1-9.

JJMIE

Volume 6, Number 2, April 2012
ISSN 1995-6665
Pages 147 - 153

Jordan Journal of Mechanical and Industrial Engineering

An Experimental Study on the Solubility of a Diesel-Ethanol Blend and on the Performance of a Diesel Engine Fueled with Diesel-Biodiesel - Ethanol Blends

M. Al-Hassan[a,*] , H. Mujafet[a] and M. Al-Shannag[b]

[a]Mechanical Engineering Department, Faculty of Engineering Technology, Al-Balqa' Applied University, Jordan
[b]Chemical Engineering Department, Faculty of Engineering Technology, Al-Balqa' Applied University, Jordan

Abstract

The phase stability of DE and DBE blends at different component concentrations, as well as the effects of using DBE blends including ethanol of various proportions on a CI engine performance are experimentally investigated. The engine was operated with DBE blends having 5, 10, 15 and 20% ethanol with fixed 10% biodiesel on a volume basis, to solve the phase separation problem, as well as on diesel fuel alone at constant load and at engine speed ranges from 800 to 1600 rpm for each run. The experimental results of the phase stability revealed that the DE blends is not stable and separated after 2, 5, 24 and 80 hours, for 20%, 15%, 10% and 5% ethanol concentration, respectively. Whereas for DBE blends the separation time is longer than of the first system and reached 1, 3 and 9 days for 20%, 15%, 10% ethanol concentration, respectively. The blend of DBE5 was of the best stability with very little separation. The experimental results of the engine performance indicated that the equivalence air-fuel ratio and the brake specific fuel consumption for the fuel blends are higher than that of diesel fuel and increases with the increase of the ethanol concentration in the blends. The brake power for the fuel blend of 5% ethanol concentration is close to that of diesel fuel and decreases with higher concentrations. The brake thermal efficiency was increased with fuel blends of 5 and 10% ethanol concentration and decreases with a higher ethanol proportion in the blends. In conclusion, among the different fuel blends, the blends containing 5 and 10% ethanol concentration are the most suited for CI engines due to its acceptable engine performance and to the fuels solubility.

Keywords: Ethanol; Biodiesel; Fuel Blends; Solubility; Engine Performance

1. Introduction

The increase on energy demand, environmental concern of the global warming and climate change and increasing petroleum price in the worldwide has greatly increased the interests of the application study of alternative fuels to internal combustion engines. Among these alternative fuels, biodiesel and diesohol (diesel – ethanol blends) have received much attention in recent years for Compression Ignition (CI) diesel engines. Ethanol is regards as a renewable fuel because it can be made from many types of raw materials such as corn, sugar cane, sugar beets, molasses, cassava, waste biomass materials, sorghum, barley, maize, etc. [1, 2]. Ethanol has been successfully used to blend with gasoline fuel as part of the alternative to reduce the consumption of conventional gasoline [3, 4]. However, it has not been commercially used to replace part of diesel fuel to diesel engines, because the barriers for application have not been overcome yet, due to the difference in chemical and physical properties between ethanol and diesel fuel. At present, significant investigations of the potential application of ethanol - diesel (ED) fuel blends on diesel engine have been carried out. Hansen et al. [5] investigated the Cummins engine performance with 15 % ED fuel blends and found that the engine power decreases by about of 7 to 10 % and the brake thermal efficiency increases by about of 2 – 3 % at rated speed. Kass et al. [6] tested the torque output from the same model engine with two blends containing 10 % and 15 % ethanol and reported an approximate 8 % engine power reduction for both fuel blends. Huang et al. [7] investigated the engine performance and exhaust emissions of diesel engine when using 10%, 20%, 25% and 30% ethanol-blended diesel fuels. In that study, the results showed that the brake thermal efficiencies decreased with increasing amount of ethanol in the blended fuels. Rakopoulos et al. [8] studied the effects of ethanol blends with diesel fuel, with 5% and 10% (v/v) on the performance and emissions of a turbocharged direct injection diesel engine. The results showed that increasing the ethanol amount in the fuel blend increased the brake specific fuel consumption and decreased the brake thermal efficiency. Results of [9–11] shows that diesel fuel blended with ethanol up to 10 vol. % can be used to solve the fuel shortage problems, increase the energy conversion efficiency, improve fuel economy and reduce its harmful emissions. Also using ED fuel blends on diesel engine can yield a significant reduction of

[*] Corresponding author. e-mail: moh_05_alhassan@yahoo.com

carbon monoxide and nitrogen oxide [12] and particulate matter emissions [13, 14]. Nevertheless, a major drawback with using ethanol in diesel engines is the limited solubility of ethanol in diesel fuel; therefore, phase separation and water tolerance in ethanol–diesel blend fuel are vital problems.

The phase separation can be prevented in two ways: by adding an emulsifier that acts to suspend small droplets of ethanol within the diesel fuel, or by adding a co- solvent that acts as a bridging agent through molecular compatibility and bonding to produce a homogeneous blend [15-18]. Emulsification usually requires heating and blending steps to generate the final blend, whereas co-solvents allow fuels to be ‘‘splash-blended’’, thus simplifying the blending process.

Currently, biodiesel is known to act as an additive or emulsifier due to its potential to improve the solubility of ethanol in diesel fuel and could improve lubricity of ethanol over a wide range of temperatures and blend properties [19–22]. Fernando and Hanna [23] determined the relative compatibilities of ethanol, biodiesel, and diesel fuel. They concluded that ethanol–biodiesel–diesel (EB-diesel) fuel blend, micro emulsions, are stable well below sub-zero temperatures and have shown equal or superior fuel properties to regular diesel fuel. Barabas and Todorut [24] studied the key fuel properties of the EB-diesel blends and investigated that blends have the same or very close density and viscosity to standardized diesel fuel. The surface tensions of the blends are only 20% higher than that of diesel fuels. In general, the blends containing 5% ethanol had very close fuel properties compared to diesel fuel. Ali et al. [25, 26] used 12 different blends of methyl tallowate, methyl soyate, ethanol, and diesel fuel in a diesel engine and found that engine performance with these blends did not differ significantly from that with diesel fuel. Violeta Makareviciene et al. [27] conducted solubility test on multi-component biodiesel fuel system. They found that rapeseed oil ethyl and methyl esters are soluble in ethanol and diesel without limits and the addition of ethanol increases the inter-solubility of ethanol and fossil diesel. Prommes kwancheareon et al. [28] conducted solubility test on EB-diesel blend using palm oil methyl ester as additive and reported emission test results of the fuel blend. They found that 5% ethanol, 15% Biodiesel and 20% diesel blend was most suitable for diesohol production due to its lower emissions and acceptable fuel properties.

Through the above literature review, it can be concluded that there are many technical barriers to the direct use of ethanol in diesel fuel, due to the differences in its physical and chemical properties: for instance, the solubility of ethanol in diesel fuel. In addition, the research results on the engine performance are contradictory. Therefore, further studies are necessary to find the way to make ethanol be mixable with diesel and then applicable to diesel engines. The objective of this study is to investigate the solubility of diesel with ethanol as well as the use of biodiesel (waste frying oil methyl esters) as an additive in stabilizing ethanol in diesel fuel blends and to conduct experiments on the diesel engine performance when fuelled with diesel-biodiesel-ethanol fuel blends compared with that fuelled with pure diesel.

2. Experimental study

The experimental study was carried out in two stages:

- To investigate the phase stability of ED and EB-diesel blends.
- And to conduct tests on engine performance when operating alternately on diesel fuel and its various blends with ethanol and biodiesel.

2.1. Fuel used:

Diesel, ethanol and biodiesel were used as the materials to form the fuel blends. Diesel fuel was obtained from the local fuels supply station, and the ethanol with a purity of 99% (Assay, UK) was purchased from a shop selling chemicals. Biodiesel fuel was produced from waste frying oil by transesterification process using methanol as the alcohol and sodium hydroxide (NaOH) as the catalyst. Methanol and NaOH both with a purity of 99% (Assay, UK) were obtained from the same place where the ethanol was purchased. The transesterification reaction was carried out with methanol/oil molar ratio of 4.5:1 and catalyst concentration of 0.5% (wt /wt. of oil) NaOH. The procedures as follows: waste frying oil was heated to 110 °C to evaporate possibly existed water in the oil and then filtered. Then the oil was poured in to (preheated to 70 °C) vessel placed on, a temperature-controlled, hotplate magnetic stirrer. With the oil stirred and heated to a temperature of 50 °C, a solution of methanol and sodium hydroxide (prepared freshly during the experiment) was added into the vessel taking this moment as time zero of the reaction. After a 30 minute reaction time, the mixture was transfer red to a separating flask and allowed to settle for overnight to produce two distinct liquid phases (i.e. methyl ester-upper layer and glycerin - lower layer). After separation of the two phases by sedimentation, the methyl esters were purified by distilling the residual methanol at 80 °C. The residual catalyst was extracted by the successive washing of the methyl ester with warm distilled water at a temperature of 50°C until the wash water becomes clear Then, the water present was removed by heating at 110 °C and the final product, biodiesel, would be obtained as a clear, light yellow liquid. Finally, the fatty acid (FA) composition of the obtained waste frying methyl ester i.e. biodiesel was determined using High Pressure Gas Chromatography (GC) model 2010 equipped with a split injector(AOC-20i), a flame ionization detector (FID) and a DB-23(60m length, 0.25mm I.D., 0.15 um film thickness) column with maximum temperature of 260ºC [29]. The operational conditions for GC were as follows: the starting temperature was 165ºC and this temperature was retained for 8 min; then the temperature was increased to 185ºC with a rate of 1ºC /min; and then increased to 220ºC with a rate of 5ºC /min, staying at 220ºC for 10 min. The injector and detector temperatures were set at 230ºC and 240ºC, respectively, and helium was used as carrier gas at a flow rate of 1.20 mL/min. The relative percentage of the FA was calculated on the basis of the peak area of a fatty acid species to the total peak area of all the fatty acids in the sample. Each FA determination was run in triplicate, and average values are reported (Table 1).

Table 1: Fatty acid composition (wt %) of the biodiesel (waste frying oil methyl esters).

Fatty acid methyl ester				Molecular mass, (kg kmol^{-1})		Percent contribution of element,%		
Trivial name	Chemical formulae	Symbol	%,by weight	Fatty acid	Contrib-ution	C	H	O
Myristic	$C_{14}H_{28}O_2$	C14:0	0.06	228.38	0.14	73.63	12.36	14.01
Palmitic	$C_{16}H_{32}O_2$	C16:0	8.51	256.43	21.82	74.94	12.58	12.48
Palmitoleic	$C_{16}H_{30}O_2$	C16:1	0.18	254.41	0.46	75.54	11.89	12.58
Heptadecanoic	$C_{17}H_{34}O_2$	C17:0	0.06	270.46	0.16	75.50	12.67	11.83
Heptadecenoic	$C_{17}H_{32}O_2$	C17:1	0.03	268.44	0.08	76.06	12.02	11.92
Stearic	$C_{18}H_{36}O_2$	C18:0	3.47	284.48	9.87	76.00	12.76	11.25
Oleic	$C_{18}H_{34}O_2$	C18:1	27.91	282.47	78.84	76.54	12.13	11.33
Linoleic	$C_{18}H_{32}O_2$	C18:2	57.98	280.45	162.61	77.09	11.50	11.41
Linolenic	$C_{18}H_{30}O_2$	C18:3	0.56	278.44	1.56	77.65	10.86	11.49
Arachidic	$C_{20}H_{40}O_2$	C20:0	0.33	312.54	1.03	76.86	12.90	10.24
Gadoleic	$C_{20}H_{38}O_2$	C20:1	0.18	310.52	0.56	77.36	12.34	10.30
Erucic	$C_{22}H_{42}O_2$	C22:0	0.52	338.58	1.76	78.04	12.50	9.45
Lignoceric	$C_{24}H_{48}O_2$	C24:0	0.21	368.65	0.77	78.20	13.12	8.68
Average value				279.66		76.42	12.28	11.31

2.2. Phase stability:

The experiments on solubility were performed on two stages: Firstly, ethanol- diesel blends with (%, v/v) 5, 10, 15 and 20 of ethanol with 95, 90, 85 and 80 of diesel, respectively, which were named as DE5, DE10, DE15 and DE20. Secondly, ethanol- biodiesel- diesel blends with (%, v/v) 5, 10, 15 and 20 of ethanol, 85, 80, 75 and 70 of diesel respectively, and with a fixed 10 % volume of biodiesel as a co-solvent, which were named as DBE5, DBE10, DBE15 and DBE20. The fuels with a predetermined volume were mixed into a homogeneous mixture by a magnetic stirrer for five minutes. Then, the final blend was kept in a graduated glass vial for observing the solubility and the physical stability.

2.3. Engine tests:

Tests have been conducted on a naturally aspirated, single cylinder, four stroke diesel engine type Lister 8-1 TE 9. The experimental set up is shown in Fig.1. The engine swept volume was 1433-cm3; the maximum power of 8-HP (6-kW). The engine was coupled to a three phase asynchronous electrical AC dynamometer (type B.K.B. Compound), which can be used for absorbing the power developed by the engine and as a motor for starting the engine. The dynamometer maximum speed is 2500 rpm; and the torque arm radius is 220-mm. The load in Newton and speed in rpm can be measured directly. The volumetric fuel consumption was measured by a glass tube divided into three sections 25, 50, and 75 cm3. and the volumetric air consumption was determined by the air consumption meter type TE 40 equipped with air tank fitted with a circular sharp-edge measuring orifice of 32.02-mm in diameter with a discharge coefficient of 0.6 and with an inclined manometer capable of reading 1-mm H2O to measure the pressure drop across the orifice. The time of 25-cm3 fuel and air consumption (during this time) were measured with a stopwatch with accuracy of ± 0.01 s.

The experiments on engine performance were carried out by using pure diesel fuel and four fuel blends at various engine-operating conditions. The fuel blends were prepared, just before starting the experiment, by pouring ethanol and biodiesel into a fuel measuring tank in the following proportions (% by volume): D85B10E5, D80B10E10, D75B10E15 and D70B10E20 and mixed together by hand in order to keep fuel blends prepared in homogeneous conditions. To obtain the baseline parameters, the engine was first operated on pure diesel fuel. The engine performance was taken at constant load and at engine speed ranges from 800 to and 1600 rpm with an increment of 200-rpm. Similar experiments with a fuel blends were conducted over the same engine load and speeds without any modification to the engine. The start of measurements were taken after the engine was warmed-up and the required speed was obtained by changing the rack position of the high pressure diesel fuel pump. The operating conditions were stabilized and the variables that were continuously measured were recorded. This included the dynamometer speed and load, time required to consume 25-cm3 of fuels, pressure drop across the orifice. Consequently, the engine torque, brake power, brake specific fuel consumption, brake thermal efficiency, actual air fuel ratio (AFR), and the equivalence AFR for the tested fuels were calculated. For all conducted experiments, before running the engine to a new fuel blend, it was allowed to run for sufficient time to consume the remaining fuel from the previous experiment. For each experiment, three runs were performed to obtain an average value of the experimental data.

3. Results and Discussion

3.1. Fuel properties:

The ultimate analysis was performed on biodiesel to determine the fatty acid methyl ester compositions and accordingly to calculate its elemental composition. Based on that analysis, as shown in table1, the elemental composition of the biodiesel consists of 76.4 wt % carbon, 12.3 wt % hydrogen and 11.3 wt % oxygen. Moreover, the calculated average chemical formula is C17.4 H33.4 O1.9. In addition, the Cetane number (CN) of the biodiesel was calculated based on the CN of the fatty acid methyl esters as shown in Tab.2, [30]. Knowing the elemental composition of the fuels used for the experiment, the Stoichiometric air-fuel ratio and the lower heating value of the fuels and fuel blends can be determined using the following equations [31 and 32]:

$$C_aH_bO + c\left(O_2 + 3.776N_2\right) = d\,CO_2 + e\,H_2O + c\left(3.776N_2\right) \tag{1}$$

$$\mathrm{LHV} = 33.9\mathrm{C} + 125.6\mathrm{H} - 10.9(\mathrm{O_y} - S) - 2.512(9H + W) \tag{2}$$

$$(LHV)_{bl} = \sum \chi_i \rho_i LHV_i / \sum \chi_i \rho_i \tag{3}$$

$$(AFR)_{bl} = \sum \chi_i \rho_i (AFR)_{st} / \sum \chi_i \rho_i \tag{4}$$

$$\rho_{bl} = \chi_i \rho_i \tag{5}$$

Based upon the ratio from Eq.1, the molecular weights of oxygen, atmospheric nitrogen, atomic carbon, and atomic hydrogen are, 15.9994, 28.16, 12.011, and 1.008, respectively. In Eq.2, C, H, Oy and W represent the elemental composition of fuels i.e. the amounts of carbon, hydrogen, oxygen and water in unit mass of the fuel, χi the volumetric percentage of fuel constituent i, ρi is the constituent i fuel density. The computation value of Stoichiometric air-fuel ratios and lower heating values of diesel, ethanol, biodiesel, and its blends are presented in Table 3.As shown from Tab. 3 ethanol has a lower cetane number than diesel fuel, and therefore the ignition delay could increase. However, the large cetane number of the biodiesel compensates, in some extent, the reduction of cetane number from addition of ethanol to diesel, thus improving the engine ignition. The lower heating value of the ethanol and biodiesel are lower than that of diesel fuel, and consequently the amounts of ethanol and biodiesel should be 1.56 and 1.14, respectively times greater than that of diesel fuel to achieve the same power output. The stoichiometric air-fuel ratio of the ethanol and biodiesel were 62% and 86%, respectively of the diesel fuel, hence the amount of air required for complete combustion is lesser. The latent heat of vaporization of the ethanol and biodiesel was 2.24 times greater than that of diesel fuel. This means that the temperature of the air-fuel mixture in the engine cylinder at the end of the compression stroke decreases (the time interval between the beginning and the end of ignition) and as a result the combustion temperature decreases. In addition, blending ethanol and biodiesel with diesel fuel can supply additional oxygen for diffusive controlled combustion phase and can cause improvements in the combustion process.

3.2. Solubility of the blends of diesel with ethanol:

The test results of the solubility of ethanol-diesel and ethanol – diesel with biodiesel as a co-solvent are shown in Figs. 2A and 2B respectively. From Fig. 2A it can be seen that the blends of ethanol with diesel were not stable and were all separated after some times. DE5, DE10, DE15 and DE20 maintained 80, 24, 5, and 2 hours, respectively, before separating. Therefore, to solve this problem, biodiesel was used as a co-solvent of ethanol in diesel fuel for further tests. The results show that all of the blends with biodiesel were all lasted longer before the separation happened. Fig. 2B shows that the blends of DBE10, DBE15 and DBE20 were separated after 9, 3 and 1 days, respectively. Whereas the blend of DBE5 was of the best stability with very little separation.

Table 3: Chemical and physical properties of the tested fuels

Property	Diesel	Biodiesel	Ethanol	DBE5	DBE10	DBE15	DBE20
Chemical formulae	$C_{12.35}H_{21.76}$	$C_{17.4}H_{33.4}O_{1.9}$	C_2H_5OH	--	--	--	--
Elemental composition, w%:							
C	87.13	76.40	52.14	--	--	--	--
H	12.88	12.23	13.13	--	--	--	--
O	0	11.30	34.73	--	--	--	--
Density @20 ºC	820	882	786	824.5	822.8	821.1	819.4
Viscosity @ 20 ºC, Pa s	2.8	4.6	1.20	--	--	--	--
Latent heat, kJ kg $^{-1}$	375	--	840	--	--	--	--
Cetane number	48	49.30	6	--	--	--	--
Lower heating value, MJ kg $^{-1}$	42.90	37.40	27.47	41.58	40.84	40.10	39.35
Stoichiometric AFR	14.45	12.48	9.0	13.98	13.72	13.46	13.19

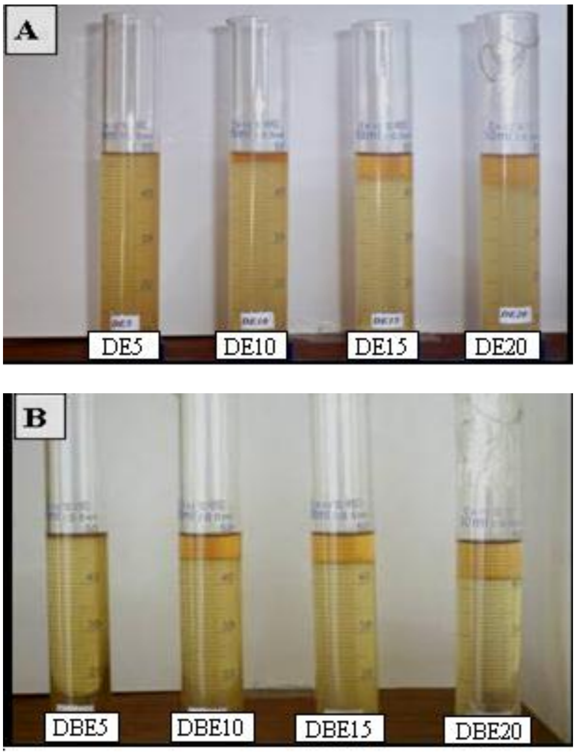

Figure 2: Solubility of the blends of ethanol with diesel: A - DE, B – DBE.

3.3. Engine performance:

For each testing condition, the volumetric fuel flow rate was measured, and then converted into the mass consumption rate based on the density of the fuels tested. Based on the engine torque, the engine speed and the mass consumption rate of the fuel and air, the actual air–fuel ratio, the brake power, the brake specific fuel consumption (BSFC) and the brake thermal efficiency (BTE) can be calculated.

3.3.1. Effect of fuel blends on equivalence air–fuel ratio:

The equivalence air–fuel ratio (ϕ) was calculated based on the actual air–fuel ratio and stoichiometric air–fuel ratio. The variation of the ϕ of diesel fuel and fuel blends as a function of the engine speed is shown in Fig.3. As shown from the figure the ϕ increases as the engine speed increase and then decrease for all fuel tested, this is due to the engine friction resistance at low speeds (up to 1400 rpm) and to the hydraulic losses in the intake system at higher speeds. In addition, it is obvious that the ϕ of the fuel blends is higher than diesel fuel. This can be attributed to the fact that at each engine speed, the amount of air enter to the engine is constant. Moreover, to obtain the same equivalence air–fuel ratio, we need more mass flow rate of fuel blends than diesel fuel, because the stoichiometric air–fuel ratio of ethanol and biodiesel is lower than diesel fuel. Accordingly, as the ethanol percentage increases in the blends the equivalence AFR increases.

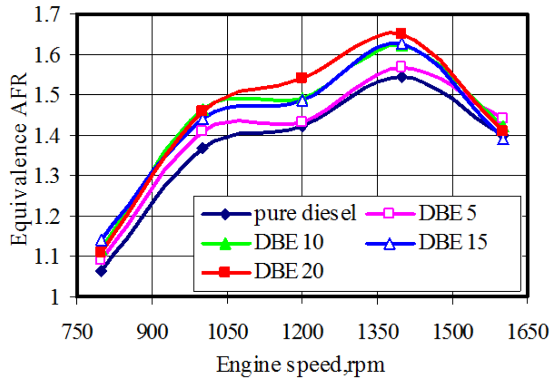

Figure 3: The variation of equivalence air-fuel ratio with different engine speeds for DBE blends and pure diesel fuel.

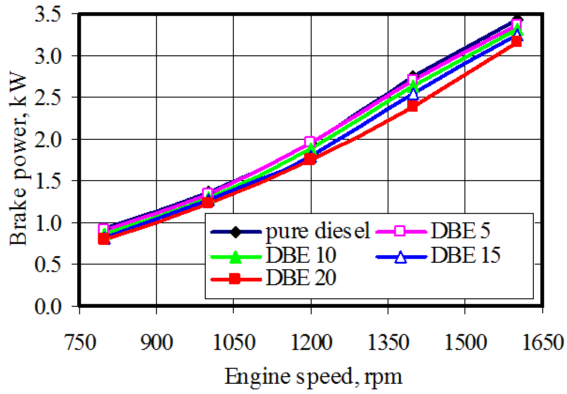

Figure 4: The variation of brake power with different engine speeds for DBE blends and pure diesel fuel.

3.3.2. Effect of fuel blends on engine brake power:

The variation of the engine brake power obtained with different fuel blends at various engine speeds is shown in Fig. 4. As the figure shows the engine power increases with the increasing of the engine speed for all fuels. Comparing with diesel fuel, the blend including 5% ethanol (DBE5) gives the same engine power. However, as the ethanol concentration increases above 5% the engine power decreases. This can be explained as follows: for a small amount of ethanol, the large cetane number of the biodiesel compensates the reduction of cetane number from addition of ethanol to diesel fuel. Therefore, the heat of combustion and the cetane number of the DBE5 blend remained steady, and thus the engine power remains the same as the engine operates with pure diesel fuel. On the other hand, as the ethanol concentration increases the cetane number of the blended fuel decreases and the auto ignition temperature and heat of vaporization (the latent heat of vaporization of ethanol is higher than diesel fuel) of blended fuels increases. Therefore, longer ignition delays occur and the combustion process may extend to the expansion stroke and the fuel cannot be completely burned as results the engine power decrease. Another reason for decreasing engine power can be related to the decreasing lower heating value of DBE blends due the lower heating value of the ethanol and biodiesel than that of diesel fuel.

3.3.3. Effect of fuel blends on brake specific fuel consumption:

The brake specific fuel consumption variation of the tested fuels at various engine speeds is shown in Fig. 5. It is obvious that the BSFC decreases with the increasing of engine speeds up to 1400 rpm, but increases after 1400 rpm. The minimum BSFC lies between the engine speeds of 1200 to 1400 rpm for all fuel tested. In addition, it can be seen that the BSFC of fuel blends are higher than that of diesel fuel, and increases with the increase of ethanol concentration in the blends. This is because the lower heating value of ethanol and biodiesel is lower than that of diesel fuel. Therefore, more fuel is required to obtain the same engine brake power.

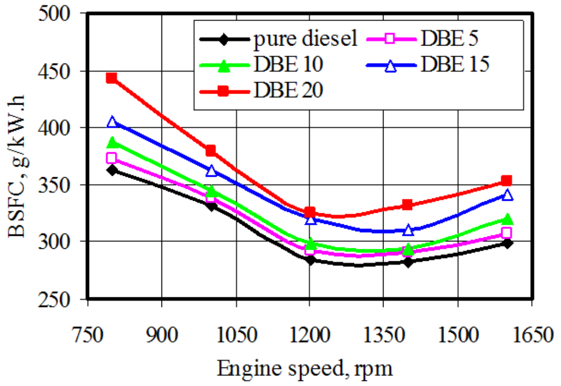

Figure 5: The variation of brake specific fuel consumption with different engine speeds for DBE blends and pure diesel fuel.

3.3.4. Effect of fuel blends on brake thermal efficiency:

The variation of brake thermal efficiency with engine speed for different fuels is shown in Fig. 6. The BTE increases with the increase of engine speed from 800 to 1400 rpm but decreases from 1400 to 1600 rpm. Compared with diesel fuel, the BTE of the DBE5 and DBE10 blends is slightly higher than that of diesel fuel. However, as the ethanol concentration increases above 10% the BTE decrease. This can be attributed to the following factors: Up to 10% ethanol concentration, the oxygen content in the fuel blends improves combustion especially during the phase of diffusion-controlled combustion and hence increases the BTE. Higher than 10% ethanol concentration, the higher latent heat of vaporization leads to increase the heat losses; the lower cetane number leads to longer ignition delay and hence incomplete combustion occur as more fuel is burned in the expansion stroke; and the reduction in lower heating value of the fuel blends leads to an increase in the volume of fuel injected to maintain the same engine power. Therefore, the combined effect of these factors will lead to the BTE decrease.

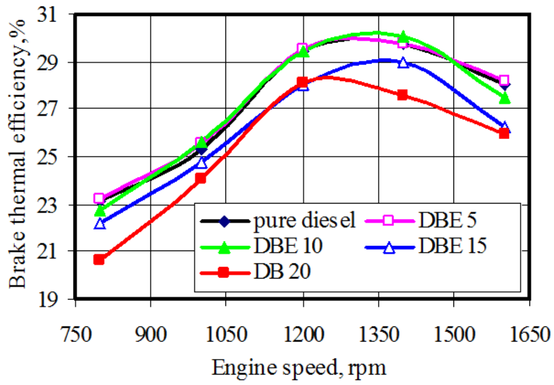

Figure 6: The variation of brake thermal efficiency with different engine speeds for DBE blends and pure diesel fuel.

4. Conclusion

An experimental study on the phase stability of ethanol-diesel and ethanol- diesel blended with a fixed amount of biodiesel as a co-solvent of ethanol in diesel fuel as will as the effect of ethanol – diesel – biodiesel blends on engine performance, and compared to the base diesel fuel had been investigated. The main results obtained can be summarized as follows:

- Waste frying oil-derived biodiesel could be used as an effective additive for diesel-ethanol mixture. The addition of biodiesel to diesel-ethanol mixture permits a higher ethanol concentration and contributes to more stable fuel blends than a mixture of only diesel-ethanol blends.
- The inter-solubility of the components of diesel–biodiesel–ethanol system decreased with increasing ethanol concentration. The blend of DBE5 was of the best stability with very little separation.
- Experimental results show that equivalence air-fuel ratio increases as the percentage of ethanol (% v) in the blended fuel increases.
- The engine brake power of fuel blend of DBE5 was very close to that of diesel fuel, but for higher ethanol concentration in the blends it was slightly lower compared with diesel fuel.
- The brake specific fuel consumption of the engine fuelled by the blends was higher compared with pure diesel. The more ethanol was added in, the higher brake specific fuel consumption was.
- The brake thermal efficiency of the engine fuelled with the DBE5% and DBE10% blends were higher but decreases as the ethanol concentrations increased compared with diesel fuel.
- In general, it can be concluded that ethanol can be used in compression ignition engines without any modification on the engine design by blending it with diesel fuel at low concentration. The phase separation which is the most important problem encountered can be prevented by adding biodiesel into the blends. The optimum percentage of ethanol was determined as 5% with 85 % diesel and 10% of biodiesel.

Acknowledgment

The authors would like to thank the Al-Balqa Applied University for supporting this work.

References

[1] P.S. De Caro, Z. Mouloungui, G. Vaitilingom, JCh. Berge, "Interest of combining an additive with diesel–ethanol blends for use in diesel engines". Fuel, Vol. 80, No. 4, 2001, 565 –74

[2] S. Prasad, A. Singh, H.C. Joshi, "Ethanol as an alternative fuel from agricultural, industrial and urban residues". Resources Conservation and Recycling, Vol.50, No. 1, 2007, 1–39.

[3] D.S. Barry, R.B.Justin, E.H.Kathleen, "Grain and cellulosic ethanol: history, economics, and energy policy". Biomass and Bioenergy, Vol.31, No. 6, 2007, 416–425.

[4] C.O.B. Regina Delgado, S. Antonio Araujo, J. Valter Jr Fernandes, "Properties of Brazilian gasoline mixed with hydrated ethanol for flex-fuel technology". Fuel Processing Technology, Vol.88, No. 4, 2007, 365–368.

[5] A.C. Hansen, Q. Zhang, "Engine durability evaluation with E-diesel". Paper Number: 036033. In: An ASAE meeting presentation, Las Vegas, Nevada, USA, 27–30 July 2003 p. 13.

[6] M.D. Kass, J.F.Thomas, J.M.Storey, N.Domingo, J.Wade, G. Kenreck, "Emissions from a 5.9 liter diesel engine fueled with ethanol diesel blends". SAE Technical Paper 2001-01-2018 (SP-1632).

[7] J.Huang, Y. Wang, S. Li, A.P. Roskilly, Y. Hongdong, H. Li, "Experimental investigation on the performance and emissions of a diesel engine fuelled with ethanol–diesel blends". Applied Thermal Engineering, Vol. 29, No. 11–12, 2009, 2484–90.

[8] D.C. Rakopoulos, C.D. Rakopoulos, E.C. Kakaras, E. Giakoumis, "Effect of ethanol–diesel fuel blends on the engine performance and emissions of heavy duty DI diesel engine". Energy Conversion and Management, Vol. 49, No. 11, 2008, 3155–62.

[9] A.C. Hansen, R.H. Hornbaker, Q. Zhang, PWL. Lyne, "On-farm evaluation of diesel fuel oxygenated with ethanol". Paper Number: 01-6173. In: An ASAE annual international meeting presentation, Sacramento, California, USA, 30 July–01August 2001 p. 17

[10] Ozer Can, smet elikten, Nazim Usta, "Effects of ethanol addition on performance and emissions of a turbocharged indirect injection diesel engine running at different injection pressures". Energy Conversion and Management, Vol. 45, 2004, 2429–40.

[11] CY. Lin, JC. Huang, "An oxygenating additive for improving the performance and emission characteristics of marine diesel engines". OCEAN Eng, Vol. 30, No. 13, 2003, 1699–715.

[12] EA. Ajav, B. Singh, TK. Bhattacharya, "Experimental study of some performance parameters of a constant speed stationary diesel engine using ethanol–diesel blends as fuel". Biomass and Bioenergy, Vol.17, 1999, 357–65.

[13] BQ. He, SJ. Shuai, JX. Wang, H. He, "The effect of ethanol blended diesel fuels on emissions from diesel engine". Atmospheric Environment, Vol. 37, 2003, 4965–71.

[14] A.C. Hansen, Q. Zhang, PWL. Lyne, "Ethanol–diesel fuel blends – a review". Bioresource Technology, Vol. 96, 2005, 277–85.

[15] M. Lapuerta, O. Armas, R. Garcı´a-Gontreras, "Stability of diesel–bioethanol blends for use in diesel engines". Fuel, Vol. 86, 2007, 1351–1357.

[16] X. Pang, X. Shi, Y. Mu, H. He, S. Shuai, , H. Chen, R. Li, "Characteristics of carbonyl compounds from a diesel-engine using biodiesel–ethanol–diesel as fuel". Atmospheric Environment, Vol. 40, 2006, 7057–7065.

[17] E.W. De Menezes, R. da Silva, R. Cataluna, R.J.C. Ortega, "Effect of ethers and ether/ethanol additives on the physicochemical properties of diesel fuel and on engine tests". Fuel, Vol.85, 2006, 815–822.

[18] X. Shi, Y. Yu, H. He, S. Shuai, J. Wang, R. Li, "Emission characteristics using methyl soyate–ethanol–diesel fuel blends on a diesel engine". Fuel, Vol.84, 2005, 1543–1549.

[19] Ribeiro, N.M., Pinto, A.C., Quintella, C.M., da Rocha, G.O., Teixeira, L.S.G., Guarieiro, L.L.N., et al. "The role of additives for diesel and diesel blended (ethanol or biodiesel) fuels: a review". Energy & Fuels, Vol. 21, 2007, 2433–2445.

[20] X. Shi, Y. Yu, H. He, S. Shuai, H. Dong, R. Li, "Combination of biodiesel– ethanol–diesel fuel and SCR catalyst assembly to reduce emissions from a heavy-duty diesel engine". Journal of Environmental Sciences, Vol. 20, 2008, 177–182.

[21] V. Makareviciene, E. Sendzikiene, P. Janulis, "Solubility of multi-component biodiesel fuel systems". Bioresource Technology, Vol. 96, 2005, 611–6.

[22] E.Sendzikiene, V. Makareviciene, P. Janulis, "Influence of fuel oxygen content on diesel engine exhaust emissions". Renewable Energy, Vol. 31, 2006, 2502–12.

[23] S. Fernando, M. Hanna, "Development of a novel biofuel blend using ethanol–biodiesel–diesel micro emulsions: EB-diesel". Energy & Fuels, Vol. 18, 2004, 1695–703.

[24] I, Barabas, I. Todorut Adrian, "Key fuel properties of biodiesel–diesel fuel–ethanol blends". SAE, Vol. -01-1810, 2009.

[25] Y. Ali, Y, KM. Eskridge, MA. Hanna, "Testing of alternative diesel fuel from tallow and soybean oil in Cummins N14-410 diesel engine". Bioresource Technology, Vol. 53, 1995, 243–54.

[26] Y. Ali, MA. Hanna, JE Borg. "Optimization of diesel, methyl tallowate and ethanol blend for reducing emissions from diesel engine". Bioresource Technology, Vol. 52, 1995, 237–43

[27] Violeta Makareviciene, Egle Sendzikiene, and Prutenis Janulis, "Solubility of multi- component biodiesel fuel systems." Bioresource Technology, Vol. 96, 2005, 611-16.

[28] P. Kwanchareon, P, A. Luengnaruemitchai, S. Jai-In, "Solubility of a diesel–biodiesel–ethanol blend, its fuel properties, and its emission characteristics from diesel engine". Fuel, Vol. 86, 2007, 1053–61.

[29] Royal Scientific Society (RSS) of Jordan, Industrial Chemistry Center, Form no. RSSPMP 1302 Rev. 2, 2010.

[30] Gerhard Knothe. "Dependence of biodiesel fuel properties on the structure of fatty acid alkyl esters". Fuel Processing Technology, Vol. 86, 2005, 1059 –1070.

[31] Heywood JB. Internal combustion engine fundamentals, New York: Mc-Graw Hill 1989, p.69

[32] Artamonov MD, Ilarionov VA, Morin MM. Motor vehicles fundamental and design, English translation, Moscow: Mir Publishers 1976, p.23.

JJMIE

Volume 6, Number 2, April 2012
ISSN 1995-6665
Pages 155 - 161

Jordan Journal of Mechanical and Industrial Engineering

Optimal Controller Design Algorithm For Non-Affine in Input Discrete-Time Nonlinear System

A. Al-Tamimi[a,*]

[a]Department of Mechatronic Engineering, Hashemite University 13115 Jordan

Abstract

Convergence is proven of the value-iteration-based algorithm to find the optimal controller in the case of general non-affine in input nonlinear systems. That is, it is shown that algorithm converges to the optimal control and the optimal value function. It is assumed that at each iteration the value and action update equations can be exactly solved. Then two standard neural networks (NN) are used: a critic NN is used to approximate the value function while an action network is used to approximate the optimal control policy.

Keyword: Optimal control; Adaptive critics; Approximate dynamic programming; Hamilton Jacobi Bellman; Value iteration; Policy iteration

1. Introduction

This paper is concerned with the design of optimal controller using the application of approximate dynamic programming techniques (ADP) to solve for the value function, and hence the optimal control policy, in discrete-time non-affine in input nonlinear optimal control problems having continuous state and action spaces. ADP is a reinforcement learning approach Sutton and Barto [20] based on adaptive critics Barto et al. [3], Widrow et al. [25]) to solve dynamic programming problems utilizing function approximation for the value function. ADP techniques can be based on value iterations or policy iterations. In contrast with value iterations, policy iterations require an initial stabilizing control action, Sutton and Barto [20]. Howard [11] proved convergence of policy iteration for Markov Decision Processes with discrete state and action spaces. Lookup tables are used to store the value function iterations at each state. Watkins [21] developed Q-learning for discrete state and action MDPs, where a ‘Q function’ is stored for each state/action pair, and model dynamics are not needed to compute the control action..

ADP was proposed by Werbos [22], [23], [24] for discrete-time dynamical systems having continuous state and action spaces as a way to solve optimal control problems, Lewis and Syrmos [14], forward in time. Bertsekas and Tsitsiklis [4] provide a treatment of Neurodynamic programming, where neural networks (NN) are used to approximate the value function. Cao [26] presents a general theory for learning and optimization.

ADP for linear systems has received ample attention. An off-line policy iteration scheme for discrete-time systems with known dynamics was given in [10] to solve the discrete-time Riccati equation. In [5] Bradtke et al. implemented an (online) Q-learning policy iteration method for discrete-time linear quadratic regulator (LQR) optimal control problems. A convergence proof was given. Hagen [9] discussed, for the LQR case, the relation between the Q-learning method and model-based adaptive control with system identification. Landelius [13] applied HDP, DHP, ADHDP and ADDHP value iteration techniques, called greedy policy iterations therein, to the discrete-time LQR problem and verified their convergence. It was shown that these iterations are in fact equivalent to iterative solution of an underlying algebraic Riccati equation, which is known to converge (Lancaster and Rodman [12]). Liu and Balakrishnan [16] showed convergence of DHP for the LQR case.

In this paper a full, rigorous proof of convergence of the online value-iteration algorithm, to solve the DT HJB equation of the optimal control problem for general non-affine in input nonlinear discrete-time systems is provided. It is assumed that at each iteration, the value update and policy update equations can be exactly solved. Note that this is true in the specific case of the LQR, where the action is linear and the value quadratic in the states. For implementation, two NN are used- the critic NN to approximate the value and the action NN to approximate the control. As a value iteration based algorithm, of course, an initial stabilizing policy is not needed.

Section II of the paper starts by introducing the non-affine in-input nonlinear discrete-time optimal control problem. Section III demonstrates how to setup the HDP algorithm to solve for the nonlinear discrete-time optimal control problem. In Section IV, the proof the convergence of HDP value iterations to the solution of the DT HJB equation is presented. In Section V, two neural network parametric structures to approximate the optimal value function and policy is introduced. As is known, this

[*] Corresponding author. e-mail: altamimi@hu.edu.jo

provides a procedure for implementing the HDP algorithm. Finally, Section VI presents example that show the practical effectiveness of the ADP technique. The example considers a nonlinear system and the results are compared to solutions based on State Dependent Riccati Equations (SDRE).

2. The Discrete-Time Hub Equation

Consider a non-affine in input nonlinear dynamical-system of the form

$$x_{k+1} = f\,(x_k, u(x_k)) \tag{1}$$

where $x \in \mathbb{R}^n$, $f(x) \in \mathbb{R}^n$, and the input $u \in \mathbb{R}^m$. Suppose the system is drift-free and, without loss of generality, that $x = 0$ is an equilibrium state, e.g. $f(0) = 0$, Assume that the system **Error! Reference source not found.** is stabilizable on a prescribed compact set $\Omega \in \mathbb{R}^n$.

Definition 1. Stabilizable system: A nonlinear dynamical system is defined to be stabilizable on a compact set $\Omega \in \mathbb{R}^n$ if there exists a control input $u \in \mathbb{R}^m$ such that, for all initial conditions $x_0 \in \Omega$ the state $x_k \to 0$ as $k \to \infty$.

It is desired to find the control action $u(x_k)$ which minimizes the infinite-horizon cost function given as

$$V(x_k) = \sum_{n=k}^{\infty} Q(x_n) + u^T(x_n) R u\ (x_n) \tag{2}$$

for all x_k, where $Q(x) > 0$ and $R > 0 \in \mathbb{R}^{m\times m}$. The class of controllers needs to be stable and also guarantee that (2) is finite, *i.e.* the control must be admissible [1].

Definition 2 Admissible Control: A control $u(x_k)$ is defined to be admissible with respect to (2) on Ω if $u(x_k)$ is continuous on a compact set $\Omega \in \mathbb{R}^n$, $u(0) = 0$, u stabilizes **Error! Reference source not found.** on Ω, and $\forall x_0 \in \Omega,\ V(x_0)$ is finite.

Equation (2) can be written as

$$\begin{aligned} V(x_k) &= x_k^T Q x_k + u_k^T R u_k + \sum_{n=k+1}^{\infty} x_n^T Q x_n + u_n^T R u_n \\ &= x_k^T Q x_k + u_k^T R u_k + V(x_{k+1}) \end{aligned} \tag{3}$$

where we require the boundary condition $V(x=0)=0$ so that $V(x_k)$ serves as a Lyapunov function. From Bellman's optimality principle [14], it is known that for the infinite-horizon optimization case, the value function $V^*(x_k)$ is time-invariant and satisfies the discrete-time Hamilton-Jacobi-Bellman (HJB) equation

$$V^*(x_k) = \min_{u_k}(x_k^T Q x_k + u_k^T R u_k + V^*(x_{k+1})) \tag{4}$$

Note that the discrete-time HJB equation develops backward-in time.

The optimal control u^* satisfies the first order necessary condition, given by the gradient of the right hand side of (4) with respect to u as

$$\frac{\partial(x_k^T Q x_k + u_k^T\ R u_k)}{\partial u_k} + \frac{\partial x_{k+1}}{\partial u_k}^T \frac{\partial V^*(x_{k+1})}{\partial x_{k+1}} = 0 \tag{5}$$

and therefore

$$u^*(x_k) = -\frac{1}{2} R^{-1} \frac{\partial x_{k+1}}{\partial u_k}^T \frac{\partial V^*(x_{k+1})}{\partial x_{k+1}} \tag{6}$$

Where

$$\frac{\partial^2 V(x_k)}{\partial u^2(x_{k)}} \rangle 0$$

Substituting (6) in (4), one may write the discrete-time HJB as

$$\begin{aligned} V^*(x_k) = x_k^T Q x_k + \frac{1}{4} \frac{\partial V^{*T}(x_{k+1})}{\partial x_{k+1}} \frac{\partial x_{k+1}}{\partial u_k} R^{-1} \frac{\partial x_{k+1}}{\partial u_k}^T \frac{\partial V^*(x_{k+1})}{\partial x_{k+1}} \\ + V^*(x_{k+1}) \end{aligned} \tag{7}$$

where $V^*(x_k)$ is the value function corresponding to the optimal control policy $u^*(x_k)$. This equation reduces to the Riccati equation in the linear quadratic regulator (LQR) case, which can be efficiently solved. In the general nonlinear case, the HJB cannot be solved exactly.

In the next sections we apply the HDP algorithm to solve for the value function V^* of the HJB equation (7) and present a convergence proof.

3. The HDP Algorithm

The HDP value iteration algorithm [22] is a method to solve the DT HJB online. In this section, a proof of convergence of the HDP algorithm for the non-affine in-input nonlinear discrete-time setting is presented.

In the HDP algorithm, one starts with an initial value, e.g. $V_0(x) = 0$ and then solves for u_0 as follows

$$u_o(x_k) = \arg\min_u (x_k^T Q x_k + u^T R u + V_0(x_{k+1})) \tag{8}$$

Once the policy u_0 is determined, iteration on the value is performed by computing

$$\begin{aligned} V_1(x_k) &= x_k^T Q x_k + u_0^T(x_k) R u_0(x_k) + V_0(f\,(x_k), u_0(x_k))) \\ &= x_k^T Q x_k + u_0^T(x_k) R u_0(x_k) + V_0(x_{k+1}) \end{aligned} \tag{9}$$

The HDP value iteration scheme therefore is a form of incremental optimization that requires iterating between a sequence of action policies $u_i(x)$ determined by the greedy update

$$\begin{aligned} u_i(x_k) &= \arg\min_u (x_k^T Q x_k + u^T R u + V_i(x_{k+1})) \\ u_i(x_k) &= \arg\min_u (x_k^T Q x_k + u^T R u + V_i(f\,(x_k, u))) \end{aligned} \tag{10}$$

and a sequence $V_i(x) \geq 0$
where

$$V_{i+1}(x_k) = \min_u (x_k^T Q x_k + u^T R u + V_i(x_{k+1})) \\ = x_k^T Q x_k + u_i^T(x_k) R u_i(x_k) + V_i(f(x_k, u_i(x_k))) \quad (11)$$

with initial condition $V_0(x_k) = 0$.

Note that, as a value-iteration algorithm, HDP *does not require an initial stabilizing gain*. This is important as stabilizing gains are difficult to find for general nonlinear systems.

Note that i is the value iterations index, while k is the time index. The HDP algorithm results in an incremental optimization that is implemented forward in time and online. Note that unlike the case for policy iterations in [10], the sequence $V_i(x_k)$ is not a sequence of cost functions and are therefore not Lyapunov functions for the corresponding policies $u_i(x_k)$ which are in turn not necessarily stabilizing. In Section IV it is shown that $V_i(x_k)$ and $u_i(x_k)$ converges to the value function of the optimal control problem and to the corresponding optimal control policy respectively.

4. Convergence of The HDP Algorithm

In this section, the proof of convergence for nonlinear HDP is presented. That is, the iteration (10) and (11) converges to the optimal value, *i.e.* $V_i \to V^*$ and $u_i \to u^*$ as $i \to \infty$. The linear quadratic case has been proven by [12] for the case of known system dynamics.

Lemma 1. Let μ_i be any arbitrary sequence of control policies and Λ_i be defined by

$$\Lambda_{i+1}(x_k) = Q(x_k) + \mu_i^T R \mu_i + \Lambda_i(\underbrace{f(x_k, \mu_i(x_k))}_{x_{k+1}}) \quad (12)$$

Let u_i and V_i be the sequences defined by (10) and (11). If $V_0(x_k) = \Lambda_0(x_k) = 0$, then $V_i(x_k) \leq \Lambda_i(x_k) \quad \forall i$.

Proof: Since $u_i(x_k)$ minimizes the right hand side of equation (11) with respect to the control u, and since $V_0(x_k) = \Lambda_0(x_k) = 0$, then by induction it follows that $V_i(x_k) \leq \Lambda_i(x_k) \quad \forall i$.

Lemma 2. Let the sequence V_i be defined as in (11). If the system is controllable, then:

- There exists an upper bound $Y(x_k)$ such that $0 \leq V_i(x_k) \leq Y(x_k) \quad \forall i$.
- If the optimal control problem (4) is solvable, there exists a least upper bound $V^*(x_k) \leq Y(x_k)$ where $V^*(x_k)$ solves (7), and that

$$\forall i : 0 \leq V_i(x_k) \leq V^*(x_k) \leq Y(x_k).$$

Proof: see [27]
Now the main result.

Theorem 1. Consider the sequence V_i and u_i defined by (11) and (10) respectively. If $V_0(x_k) = 0$, then it follows that V_i is a non-decreasing sequence $\forall i : V_{i+1}(x_k) \geq V_i(x_k)$. Moreover, as $i \to \infty$, $V_i \to V^*$, $u_i \to u^*$ and hence the sequence V_i converges to the solution of the DT HJB (7).

Proof: From Lemma 1, let μ_i be any arbitrary sequence of control policies and Λ_i be defined by

$$\Lambda_{i+1}(x_k) = Q(x_k) + \mu_i^T R \mu_i + \Lambda_i(\underbrace{f(x_k, \mu_i(x_k))}_{x_{k+1}})$$

If $V_0(x_k) = \Lambda_0(x_k) = 0$, it follows that $V_i(x_k) \leq \Lambda_i(x_k) \quad \forall i$. Now assume that $\mu_i(x_k) = u_{i+1}(x_k)$ such that

$$\Lambda_{i+1}(x_k) = Q(x_k) + \mu_i^T R \mu_i + \Lambda_i(f(x_k, \mu_i(x_k))) \\ = Q(x_k) + u_{i+1}^T R u_{i+1} + \Lambda_i(f(x_k, u_{i+1}(x_k))) \quad (13)$$

and consider

$$V_{i+1}(x_k) = Q(x_k) + u_i^T R u_i + V_i(f(x_k, u_i(x_k))) \quad (14)$$

It will next be proven by induction that if $V_0(x_k) = \Lambda_0(x_k) = 0$, then $\Lambda_i(x_k) \leq V_{i+1}(x_k)$. Induction is initialized by letting $V_0(x_k) = \Lambda_0(x_k) = 0$ and hence

$$V_1(x_k) - \Lambda_0(x_k) = Q(x_k) \\ \geq 0 \\ V_1(x_k) \geq \Lambda_0(x_k)$$

Now assume that $V_i(x_k) \geq \Lambda_{i-1}(x_k)$, then subtracting (13) from (14) it follows that

$$V_{i+1}(x_k) - \Lambda_i(x_k) = V_i(x_{k+1}) - \Lambda_{i-1}(x_{k+1}) \geq 0$$

and this completes the proof that $\Lambda_i(x_k) \leq V_{i+1}(x_k)$.

From $\Lambda_i(x_k) \leq V_{i+1}(x_k)$ and $V_i(x_k) \leq \Lambda_i(x_k)$, it then follows that

$$\forall i : V_i(x_k) \leq V_{i+1}(x_k).$$

From part a) in Lemma 2 and the fact that V_i is a non-decreasing sequence, it follows that $V_i \to V_\infty$ as $i \to \infty$. From part b) of Lemma 2, it also follows that

$$V_\infty(x_k) \leq V^*(x_k).$$

It now remains to show that in fact V_∞ is V^*. To see this, note that from (11) it follows that

$$V_\infty(x_k) = x_k^T Q x_k + u_\infty^T(x_k) R u_\infty(x_k) + V_\infty(f(x_k, u_\infty(x_k)))$$

and hence

$$V_\infty(f(x_k, u_\infty(x_k))) - V_\infty(x_k) = -x_k^T Q x_k - u_\infty^T(x_k) R u_\infty(x_k)$$

and therefore $V_\infty(x_k)$ is a Lyapunov function for a stabilizing and admissible policy $u_\infty(x_k) = \eta(x_k)$. Using part b) of Lemma 2 it follows that $V_\infty(x_k) = Y(x_k) \geq V^*(x_k)$. This implies that $V^*(x_k) \leq V_\infty(x_k) \leq V^*(x_k)$ and hence $V_\infty(x_k) = V^*(x_k)$, $u_\infty(x_k) = u^*(x_k)$.

5. Neural Network Approximation for Value and Action

It has just been proven that the nonlinear HDP algorithm converges to the value function of the DT HJB equation that appears in the non-affine in-input nonlinear discrete-time optimal control. It was assumed that the action and value update equations (10), (11) can be exactly solved at each iteration. In fact, these equations are difficult to solve for general nonlinear systems. Therefore, for implementation purposes, one needs to approximate u_i, V_i at each iteration. This allows approximate solution of (10), (11).

In this section, we review how to implement the HDP value iterations algorithm with two parametric structures such as neural networks [24] [15]. NN Approximation for Implementation of HDP Algorithm for Nonlinear Systems

It is well known that neural networks can be used to approximate smooth functions on prescribed compact sets [28]. Therefore, to solve (11) and (10), $V_i(x)$ is approximated at each step by a critic NN

$$\hat{V}_i(x) = \sum_{j=1}^{L} w_{vi}^j \phi_j(x) = W_{Vi}^T \boldsymbol{\phi}(x) \tag{15}$$

and $u_i(x)$ by an action NN

$$\hat{u}_i(x) = \sum_{j=1}^{M} w_{ui}^j \sigma_j(x) = W_{ui}^T \boldsymbol{\sigma}(x) \tag{16}$$

where the activation functions are $\phi_j(x), \sigma_j(x) \in C^1(\Omega)$ respectively. Since it is required that $V_i(0) = 0$ and $u_i(0) = 0$, we select activation functions with $\phi_j(0) = 0, \sigma_j(0) = 0$. Moreover, since it is known that V^* is a Lyapunov function, and Lyapunov proofs are convenient if the Lyapunov function is symmetric and positive definite, it is convenient to also require that the activation functions for the critic NN be symmetric, i.e. $\phi_j(x) = \phi_j(-x)$.

The neural network weights in the critic NN (15) are w_{vi}^j. L is the number of hidden-layer neurons. The vector $\boldsymbol{\phi}(x) \equiv \left[\phi_1(x)\ \phi_2(x) \cdots \phi_L(x)\right]^T$ is the vector activation function and $W_{Vi} \equiv \left[w_{vi}^1\ w_{vi}^2 \cdots w_{vi}^L\right]^T$ is the weight vector at iteration i. Similarly, the weights of the neural network in (16) are w_{ui}^j. M is the number of hidden-layer neurons. $\boldsymbol{\sigma}(x) \equiv \left[\sigma_1(x)\ \sigma_2(x) \cdots \sigma_L(x)\right]^T$ is the vector activation function, and $W_{ui} \equiv \left[w_{ui}^1\ w_{ui}^2 \cdots w_{ui}^L\right]^T$ is the vector weight.

According to (11), the critic weights are tuned at each iteration of HDP to minimize the residual error between $\hat{V}_{i+1}(x_k)$ and the target function defined in equation (17) in a least-squares sense for a set of states x_k sampled from a compact set $\Omega \subset \mathbb{R}^n$.

$$\begin{aligned} d(x_k, x_{k+1}, W_{Vi}, W_{ui}) &= x_k^T Q x_k + \hat{u}_i^T(x_k) R \hat{u}_i(x_k) + \hat{V}_i(x_{k+1}) \\ &= x_k^T Q x_k + \hat{u}_i^T(x_k) R \hat{u}_i(x_k) + W_{Vi}^T \boldsymbol{\phi}(x_{k+1}) \end{aligned} \tag{17}$$

The residual error (c.f. temporal difference error) becomes

$$\left(W_{Vi+1}^T \boldsymbol{\phi}(x_k) - d(x_k, x_{k+1}, W_{Vi}, W_{ui})\right) = e_L(x) \tag{18}$$

Note that the residual error in (18) is explicit, in fact linear, in the tuning parameters W_{Vi+1}. Therefore, to find the least-squares solution, the method of weighted residuals may be used [8]. The weights W_{Vi+1} are determined by projecting the residual error onto $de_L(x)/dW_{Vi+1}$ and setting the result to zero $\forall x \in \Omega$ using the inner product, *i.e.*

$$\left\langle \frac{de_L(x)}{dW_{Vi+1}}, e_L(x) \right\rangle = 0 \tag{19}$$

where $\langle \mathrm{f,g} \rangle = \int_\Omega f g^T dx$ is a Lebesgue integral. One has

$$0 = \int_\Omega \phi(x_k)\left(\phi^T(x_k) W_{Vi+1} - d^T(x_k, x_{k+1}, W_{Vi}, W_{ui})\right) dx_k \tag{20}$$

Therefore a unique solution for W_{Vi+1} exists and is computed as

$$W_{Vi+1} = \left(\int_\Omega \phi(x_k)\phi(x_k)^T dx\right)^{-1} \int_\Omega \phi(x_k) d^T(\phi(x_k), W_{Vi}, W_{ui}) dx \tag{21}$$

To use this solution, it is required that the outer product integral be positive definite. This is known as a persistence of excitation condition in system theory. The next assumption is standard in selecting the NN activation functions as a basis set.

Assumption 1. The selected activation functions

$\left\{\phi_j(x)\right\}^L$ are linearly independent on the compact set $\Omega \subset \mathbb{R}^n$.

Assumption 1 guarantees that excitation condition is satisfied and hence $\int_{\Omega} \phi(x_k)\phi(x_k)^T dx$ is of full rank and invertible and a unique solution for (21) exists.

The action NN weights are tuned to solve (10) at each iteration. The use of $\hat{u}_i(x_k, W_{ui})$ from (16) allows the rewriting of equation (16) as

$$W_{ui} = \arg\min_{w} \left(x_k^T Q x_k + \hat{u}_i^T(x_k, w) R \hat{u}_i(x_k, w) + \hat{V}_i(x_{k+1}^i) \right)\Big|_{\Omega} \tag{22}$$

where $x_{k+1}^i = f(x_k, \hat{u}_i(x_k, w))$ and the notation means minimization for a set of points x_k selected from the compact set $\Omega \in \mathbb{R}^n$.

Note that the control weights W_{ui} appear in (22) in an implicit fashion, *i.e.* it is difficult to solve explicitly for the weights since the current control weights determine x_{k+1}. Therefore, one can use an LMS algorithm on a training set constructed from Ω. The weight update is therefore

$$\begin{aligned} W_{ui}\big|_{m+1} &= W_{ui}\big|_m - \\ &\alpha \left. \frac{\partial \left(x_k^T Q x_k + \hat{u}_i^T(x_k, W_{ui}\big|_m) R\, \hat{u}_i(x_k, W_{ui}\big|_m) + \hat{V}_i(x_{k+1}) \right)}{\partial W_{ui}} \right|_{W_{ui}|_m} \\ &= W_{ui}\big|_m - \alpha \sigma(x_k) \left(2R\hat{u}_i(x_k, W_{ui}\big|_m) + \frac{\partial x_{k+1}}{\partial u_k}^T \frac{\partial \phi(x_{k+1})}{\partial x_{k+1}} W_{Vi} \right)^T \end{aligned} \tag{23}$$

where α is a positive step size and m is the iteration number for the LMS algorithm. By a stochastic approximation type argument, the weights $W_{ui}\big|_m \Rightarrow W_{ui}$ as $m \Rightarrow \infty$, and satisfy (22). Note that one can use alternative tuning methods such as Newton's method and Levenberg-Marquardt in order to solve (22).

6. Simulation Examples

In this section, an examples are provided to demonstrate the solution of the DT HJB equation. The example is for a DT non-affine in-input nonlinear system. MATLAB is used in the simulations to implement some of the functions discussed in the paper.

Consider the following affine in input nonlinear system

$$x_{k+1} = f(x_k, u_k) \tag{24}$$

Where

$$f(x_k, u_k) = \begin{bmatrix} 0.2x_k(1)\exp(x_k^2(2)) \\ .3x_k^3(2) \end{bmatrix} + \begin{bmatrix} 0 \\ -.2 \end{bmatrix} u_k^2$$

The approximation of the value function is given as

$$\hat{V}_{i+1}(x_k, W_{Vi+1}) = W_{Vi+1}^T \phi(x_k)$$

The vector activation function is selected as

$$\begin{aligned} \phi(x) = [&x_1^2 \quad x_1x_2 \quad x_2^2 \quad x_1^4 \quad x_1^3x_2 \\ &x_1^2x_2^2 \quad x_1x_2^3 \quad x_2^4 \quad x_1^6 \quad x_1^5x_2 \quad x_1^4x_2^2 \\ &x_1^3x_2^3 \quad x_1^2x_2^4 \quad x_1x_2^5 \quad x_2^6] \end{aligned}$$

and the weight vector is

$$W_V^T = \begin{bmatrix} w_v^1 & w_v^2 & w_v^3 & w_v^4 & \ldots\ldots & w_v^{15} \end{bmatrix}.$$

The control is approximated by

$$\hat{u}_i = W_{ui}^T \sigma(x_k)$$

where the vector activation function is

$$\begin{aligned} \sigma^T(x) = [&x_1 \quad x_2 \quad x_1^3 \quad x_1^2x_2 \quad x_1x_2^2 \\ &x_2^3 \quad x_1^5 \quad x_1^4x_2 \quad x_1^3x_2^2 \quad x_1^2x_2^3 \\ &x_1x_2^4 \quad x_2^5] \end{aligned}$$

and the weights are

$$W_u^T = \begin{bmatrix} w_u^1 & w_u^2 & w_u^3 & w_u^4 & \ldots\ldots & w_u^{12} \end{bmatrix}$$

The control NN activation functions are selected as the derivatives of the critic activation functions, since the gradient of the critic activation functions appears in (23). The critic activations are selected as polynomials to satisfy $\hat{V}_i(0) = 0$ at each step. Note that then automatically one has $\hat{u}_i(0) = 0$ as required for admissibility. The result of the algorithm is compared to the discrete-time State Dependent Riccati Equation (SDRE) proposed in [6].

The training sets is $x_1 \in [-2, 2]$, $x_2 \in [-1, 1]$. The value function weights converged to the following

$$W_V^T = [1.0382 \;\; 0 \;\; 1.0826 \;\; .0028 \;\; \text{-}0 \;\; \text{-}.053 \;\; 0 \;\; \text{-}.2792 \;\; \text{-}.0004 \;\; 0 \;\; \text{-}.0013 \;\; 0 \;\; .1549 \;\; 0 \;\; .3034]$$

and the control weights converged to

$$W_u^T = [0 \;\; \text{-}.0004 \;\; 0 \;\; 0 \;\; 0 \;\; .0651 \;\; 0 \;\; 0 \;\; 0 \;\; \text{-}.0003 \;\; 0 \;\; \text{-}.0046]$$

The result of the nonlinear optimal controller derived in this paper is compared to the SDRE approach. Figure 2 and Figure 3 show the states trajectories for the system for both.

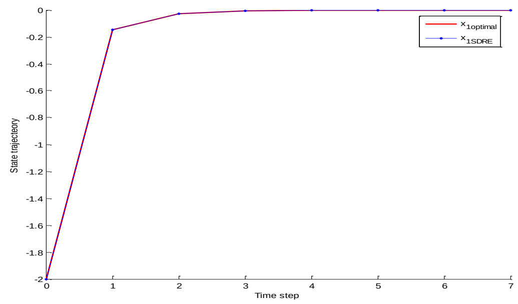

Figure 2: The state trajectory for both methods.

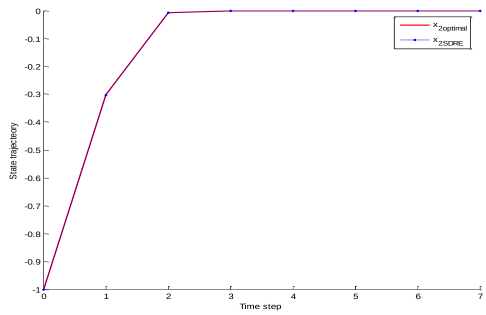

Figure 3: The state trajectory for both methods.

In Figure 4, the cost function of the SDRE solution and the cost function of the proposed algorithm in this paper are compared. It is clear from the simulation that the cost function for the control policy derived from the HDP method is lower than that of the SDRE method. In Figure 5, the control signals for both methods are shown.

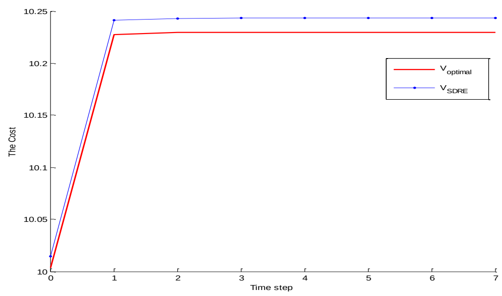

Figure 4: The cost function for both methods.

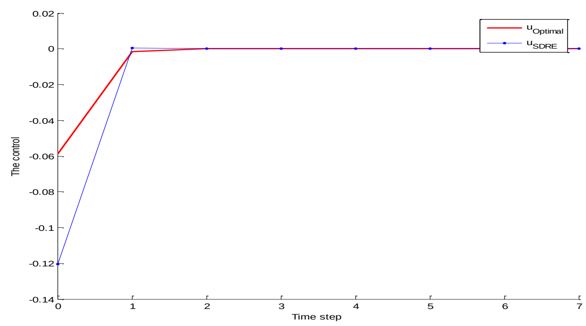

Figure 5: The control signal input for both methods.

7. Conclusion

It has been proven the convergence of the algorithm to the value function solution of Hamilton-Jacobi-Bellman equation for non-affine in-input nonlinear dynamical systems, assuming exact solution of value update and the action update at each iteration.

Neural networks are used as parametric structures to approximate at each iteration the value (i.e. critic NN), and the control action. In the special case affine-in input nonlinear system $x_{k+1}=f(x_k)+g(x_k)u_k$, the use of the second neural network to approximate the control policy, the internal dynamics, *i.e.* $f(x_k)$, is not needed to implement HDP. This holds as well for the special LQR case for linear system as shown in [27], where use of two NN avoids the need to know the system internal dynamics. In the non-affine in-input nonlinear example, it is shown that the optimal controller derived from the HDP based value iteration method outperforms suboptimal control methods like those found through the SDRE method.

References

[1] Abu-Khalaf, M., F. L. Lewis, "Nearly Optimal Control Laws for Nonlinear Systems with Saturating Actuators Using a Neural Network HJB Approach," Automatica, vol. 41, pp. 779 – 791, 2005.

[2] Al-Tamimi, A., M. Abu-Khalaf, F. L. Lewis, "Adaptive Critic Designs for Discrete-Time Zero-Sum Games with Application to H-Infinity Control" *IEEE Transactions on Systems, Man, Cybernetics-Part B*, Cybernaetics, Vol 37, No 1, pp 240-247, Feb , 2007.

[3] Barto, A. G., R. S. Sutton, and C. W. Anderson, "Neuronlike elements that can solve difficult learning control problems," *IEEE Trans. Syst., Man, Cybern.*, vol. SMC-13, pp. 835–846, 1983.

[4] Bertsekas, D.P. and J. N. Tsitsiklis, *Neuro-Dynamic Programming*, Athena Scientific, MA, 1996.

[5] Bradtke, S. J., B. E. Ydestie, A. G. Barto, "Adaptive linear quadratic control using policy iteration," Proceedings of the American Control Conference , pp. 3475-3476, Baltmore, Myrland, June, 1994.

[6] Cloutier, J. R.," State –Dependent Riccati equation Techniques: An overview," Proceeding of the American control conference, Albuquerque, NM, June 4-6, 1997, pp 932-936.

[7] Ferrari, S., Stengel, R. "Model-Based Adaptive Critic Designs", pp 64-94, Eds J. Si, A. Barto, W. Powell, D. Wunsch *Handbook of Learning and Approximate Dynamic Programming, Wiley*, August 2004.

[8] Finlayson, B. A.. The Method of Weighted Residuals and Variational Principles. Academic Press, New York, 1972

[9] Hagen, S. B Krose, " Linear quadratic Regulation using Reinforcement Learning," Belgian_Dutch Conference on Mechanical Learning, pp. 39-46, 1998.

[10] Hewer, G.A., "An iterative technique for the computation of the steady state gains for the discrete optimal regulator," IEEE Trans. Automatic Control, pp. 382-384, Aug. 1971.

[11] Howard, R., *Dynamic Programming and Markov Processes*, MIT Press, Cambridge, MA, 1960.

[12] Lancaster, P. L. Rodman, *Algebraic Riccati Equations*, Oxford University Press, UK 1995.

[13] Landelius, T., *Reinforcement Learning and Distributed Local Model Synthesis*, PhD Dissertation, Linkoping University, Sweden, 1997.

[14] Lewis, F. L., V. L. Syrmos, *Optimal Control*, 2nd ed., John Wiley, 1995.

[15] Lewis, F. L., Jagannathan, S., & Yesildirek, A.. *Neural Network Control of Robot Manipulators and Nonlinear Systems.* Taylor & Franci, (1999).

[16] Lu, X., S.N. Balakrishnan, "Convergence analysis of adaptive critic based optimal control," Proc. Amer. Control Conf., pp. 1929-1933, Chicago, 2000.
[17] Prokhorov, D., D. Wunsch, "Adaptive critic designs," IEEE Trans. on Neural Networks, vol. 8, no. 5, pp 997-1007, 1997.
[18] Si, Ji. A. Barto, W. Powell, D. Wunsch, *Handbook of Learning and Approximate Dynamic Programming*, John Wiley, New Jersey, 2004.
[19] Stevens B., F. L. Lewis, *Aircraft Control and Simulation*, 2nd edition, John Wiley, New Jersey, 2003.
[20] Sutton, R.S., A.G. Barto, *Reinforcement Learning*, MIT Press, Cambridge, MA, 1998.
[21] Watkins, C., *Learning from Delayed Rewards*, Ph.D. Thesis, Cambridge University, Cambridge, England, 1989.
[22] Werbos, P.J., "A menu of designs for reinforcement learning over time," , Neural Networks for Control, pp. 67-95, ed. W.T. Miller, R.S. Sutton, P.J. Werbos, Cambridge: MIT Press, 1991.
[23] Werbos, P.J., "Approximate dynamic programming for real-time control and neural modeling," Handbook of Intelligent Control, ed. D.A. White and D.A. Sofge, New York: Van Nostrand Reinhold, 1992.
[24] Werbos, P.J., "Neural networks for control and system identification," Heuristics, Vol. 3, No. 1, Spring 1990, pp. 18-27,.1990.
[25] Widrow, B., N. Gupta, and S. Maitra, "Punish/reward: Learning with a critic in adaptive threshold systems," IEEE Trans. Syst., Man, Cybern., vol. SMC-3, pp. 455–465, 1973.
[26] Xi-Ren Cao, "Learning and Optimization—From a SystemsTheoretic Perspective", Proc. of IEEE Conference on Decision and Control, pp. 3367-3371, 2002.
[27] Al-Tamimi, F. L. Lewis, M. Abu-Khalaf, "Discrete-time nonlinear HJB solution using Approximate dynamic programming: Convergence Proof," *IEEE Transactions on Systems, Man, Cybernetics-Part B*, Volume 38, Issue 4, pages 943 – 949, Aug 2008.
[28] Hornik, K., A. Stinch combe, H. White (1990). Universal approximation of unknown mapping and its derivatives using multilayer feed forward networks, Neural Newton, Vol.3, P 551-560.

Appendix

Lemma 2. Let the sequence V_i be defined as in (11). If the system is controllable, then:

- There exists an upper bound $Y(x_k)$ such that $0 \le V_i(x_k) \le Y(x_k)\ \ \forall i$.
- If the optimal control problem (4) is solvable, there exists a least upper bound $V^*(x_k) \le Y(x_k)$ where $V^*(x_k)$ solves (7), and that $\forall i: 0 \le V_i(x_k) \le V^*(x_k) \le Y(x_k)$.

Proof: Let $\eta(x_k)$ be any stabilizing and admissible control policy, and Let $V_0(x_k) = Z_0(x_k) = 0$ where Z_i is updated as

$$\begin{aligned} Z_{i+1}(x_k) &= Q(x_k) + \eta^T(x_k) R\eta(x_k) + Z_i(x_{k+1}) \\ x_{k+1} &= f(x_k) + g(x_k)\eta(x_k) \end{aligned} \tag{1}$$

It follows that the difference

$$\begin{aligned} Z_{i+1}(x_k) - Z_i(x_k) &= Z_i(x_{k+1}) - Z_{i-1}(x_{k+1}) \\ &= Z_{i-1}(x_{k+2}) - Z_{i-2}(x_{k+2}) \\ &= Z_{i-2}(x_{k+3}) - Z_{i-3}(x_{k+3}) \\ &\ \ . \\ &\ \ . \\ &\ \ . \\ &= Z_1(x_{k+i}) - Z_0(x_{k+i}) \end{aligned} \tag{2}$$

Since $Z_0(x_k) = 0$, it then follows that

$$\begin{aligned} Z_{i+1}(x_k) &= Z_1(x_{k+i}) + Z_i(x_k) \\ &= Z_1(x_{k+i}) + Z_1(x_{k+i-1}) + Z_{i-1}(x_k) \\ &= Z_1(x_{k+i}) + Z_1(x_{k+i-1}) + Z_1(x_{k+i-1}) + Z_{i-2}(x_k) \\ &= Z_1(x_{k+i}) + Z_1(x_{k+i-1}) + Z_1(x_{k+i-2}) + ... + Z_1(x_k) \end{aligned} \tag{3}$$

and equation (2) can be written as

$$\begin{aligned} Z_{i+1}(x_k) &= \sum_{n=0}^{i} Z_1(x_{k+n}) \\ &= \sum_{n=0}^{i} (Q(x_{k+n}) + \eta^T(x_{k+n}) R\eta(x_{k+n})) \\ &\le \sum_{n=0}^{\infty} (Q(x_{k+n}) + \eta^T(x_{k+n}) R\eta(x_{k+n})) \end{aligned}$$

Since $\eta(x_k)$ is an admissible stabilizing controller, $x_{k+n} \to 0$ as $n \to \infty$ and

$$\forall i: \quad Z_{i+1}(x_k) \le \sum_{i=0}^{\infty} Z_1(x_{k+i}) = Y(x_k)$$

Using Lemma 1 with $\mu_i(x_k) = \eta(x_k)$ and $\Lambda_i(x_k) = Z_i(x_k)$, it follows that

$$\forall i: \quad V_i(x_k) \le Z_i(x_k) \le Y(x_k)$$

which proves part a). Moreover if $\eta(x_k) = u^*(x_k)$, then

$$\underbrace{\sum_{n=0}^{\infty} (Q(x_{k+n}) + u^{*T}(x_{k+n}) Ru^*(x_{k+n}))}_{V^*(x_k)} \le \underbrace{\sum_{n=0}^{\infty} (Q(x_{k+n}) + \eta^T(x_{k+n}) R\eta(x_{k+n}))}_{Y(x_k)}$$

and hence $V^*(x_k) \le Y(x_k)$ which proves part b) and shows that $\forall i: 0 \le V_i(x_k) \le V^*(x_k) \le Y(x_k)$ for any $Y(x_k)$ determined by an admissible stabilizing policy $\eta(x_k)$.

JJMIE

Volume 6, Number 2, April 2012
ISSN 1995-6665
Pages 163 - 173

Jordan Journal of Mechanical and Industrial Engineering

Costing of the Production and Delivery of Ready-Mix-Concrete

O. Al-Araidah[a,]*, A. Momani[a], N. AlBashabsheh[a], N. Mandahawi[b], R. H. Fouad[b]

[a]Industrial Engineering Department, Jordan University of Science and Technology, Irbid, Jordan
[b]Department of Industrial Engineering, Hashemite University, Zarqa, Jordan

Abstract

The paper presents a model for costing production and transportation of ready-mix-concrete (RMC) based on type of the mix and customer site information. The on-floor cost of the mix is based on the type of concrete and is estimated using activity based costing (ABC). The cost of transporting RMC to customer's site is obtained as a function of traveling distance, traffic factor, and demand. Volume-based discounts, penalty for late delivery, and cost of mix spoilage are considered. Moreover, the paper provides a cost ground for improving the RMC production system using activity based management (ABM) to improve the financial performance of the company. The proposed model is applied at a local RMC company where obtained results show differences between the costing system of the company and that using the proposed model.

Keywords: Activity-based costing (ABC); Activity-based management (ABM); Ready mix concrete (RMC)

1. Introduction

Companies sell their products/services to make profit, where profit on a product is the difference between the selling price and the total cost of making that product. To be successful, a product must satisfy design specification within the cost criteria specified at the start of the project. To estimate the cost of a product, traditional cost methodologies were used since 1920s. Theses costing methodologies were appropriate then but not today because of the different financial objectives (pricing and profitability analysis, not inventory valuation) and the different operating situation (labors intensive, overheads, majority of cost is the manufacturing cost, single product company). On the other hand, activity-based costing (ABC) tackles theses issues.

ABC is a costing model that identifies activities in an organization and assigns the cost of each activity resource to products according to the actual consumption by each activity. This helps estimating the actual cost of products for the purpose of discontinuing unprofitable products and lowering prices of overpriced ones. ABC assigns the cost of resource to products through activities. As a result, ABC has predominantly been used to support strategic decisions such as pricing, outsourcing, and identification and measurement of process improvement initiatives. Several researchers discussed costing criteria in the manufacturing and service arenas. In this study, we utilize ABC in leading efforts for managing and improving activities in ready-mixed concrete (RMC) plants.

RMC refers to concrete that is specifically manufactured for delivery to the customer's construction site by truck-mounted transit mixers in a freshly mixed and plastic or unhardened state. The first ready-mix factory was built in the 1930s, but the industry did not begin to expand significantly until the 1960s, and it has continued to grow since then. RMC can be custom-made to suit different applications and is sold by volume usually expressed in cubic meters. It is sometimes preferred over on-site concrete mixing because of the precision of the mixture and reduced worksite confusion. Other advantages of RMC include elimination of storage space for basic materials at site, less labor, and lower levels of pollution at the site. A disadvantage of RMC is the impact of traveling time on properties of concrete. This time is largely influenced by the distance from plant to site, weight limits of roads and bridges, and traffic conditions. Today, modern additives help elongate the time-span of RMC at added expense. To our knowledge, no research exists that utilizes ABC for managing/improving the activities of producing and transporting RMC.

This paper presents a model for costing RMC based on the type of the mix and site information. To this end, the production process is subdivided into its main activities. The cost of each activity is then evaluated utilizing financial records of the company. A cost fraction of that activity is allocated to a product based on the rate of its consumption of that activity [1, 2]. The per-product cost is set constant for a product regardless to the customer information. A further investigation of the value of each activity is used to improve the performance of the production system and hence reduce the cost. The second cost phase deals with transporting products to customer's site. The study employs heuristics for concrete delivery to compute the actual cost of transportation based on site information, the volume of the ordered product, and the state of the traffic to and from the site. Cost information are then used to derive improvement efforts of the various

* Corresponding author. e-mail: alarao@just.edu.jo

activities using lean thinking. Projected results help managers realize cost and efforts associated with production and overhead activities. The rest of the paper is organized as follows. Section 2 provides background and reviews related literature. Section 3 presents the proposed costing model. Section 4 presents a case study and the final section provides concluding remarks.

2. Background and Literature Review

In today's markets, manufacturing companies, especially small ones, struggle to increase their profits because of the high competitiveness and globalization. Therefore, more efforts are directed towards reducing production expenses. To this end, the impact of the various value-added, supporting, and non value-added activities on the cost of the product or service should be investigated.

Today, manufacturing companies are becoming more information intensive, highly flexible, and immediately responsive to the customer expectations [3]. Due to the changing manufacturing environment, traditional cost accounting is rapidly disappearing. Traditional accounting systems were developed at a time when direct labor contributed to a large percentage of the total cost of the product. Changes in manufacturing technologies, such as the just-in-time philosophy, robotics, and flexible manufacturing systems decreased the direct labor component of production and increased overhead cost. In today's manufacturing environment, direct labor accounts for only 10% of the cost, whereas material accounts for 55% and overhead for 35%. As a result, product cost distortion occurs due to allocating overhead cost to the products arbitrarily on the basis of direct labor hours used by each product [4, 5]. Cooper reports several situations that can cause distortions to occur, examples include production volume diversity, complexity diversity, material diversity, and setup diversity [6, 7]. In the literature, several researchers applied ABC in real life. Examples include air conditioning industry [8], land transportation [9], agricultural systems [10], and healthcare [11, 12].

ABC emerged as a logical alternative to traditional cost management systems that tended to produce insufficient results when it came to allocating cost. The concept of ABC came into prominence with the development of ABM by cooper and Kaplan in 1988 [1]. ABC concentrates on the need to make a more realistic allocation of overhead cost to products. It emphasizes the requirement to obtain a better understanding of the behavior of overhead cost, and thus ascertains what causes overhead cost and how they relate to products ABC provides information to identify the components of overhead more precisely, assigns cost of resource to products more accurately, and as a result it acts as a decision support tool for companies [4, 13]. The implementation of ABC is justified if the cost of installing and operating the system are more than offsets by the long term benefits [14]. Several limitations of ABC are presented in [15, 16, 17].

Element of ABC include Activity: Work performed within an organization or the aggregations of action performed within an organization. Activity driver: Associates activates with their respective cost object. Activity drivers' measure the frequency and intensity of the demand placed on activities by cost objects. They are typically a one-to-one relationship with the activity. Activity measures: A measure of the workload involved in the activity. It can be similar to the activity driver. Bill of activity: A listing of the activities required (and optionally, the associated cost of the resources consumed) by a product or other cost object. It should list each activity, activity drivers, number of units, unit cost per driver, and extended cost that, taken together, compose the total for any particular cost object. Cost drivers: Any element that would cause a change in the cost of activity. Cost elements: An amount paid for a resource consumed by an activity and included in activity cost pool. Cost objects: Any customer, product, service, contract, project, or other work unit for that separate cost measurement is desired. Performance measures: Indicators of the work performed and the results achieved in an activity, process, or organizational unit. Performance measures may be financial or operational. Processes: A series of activities linked to perform a specific objective. Resources: An economic element that is applied or used in the performance of activities, salaries and materials are resources used in the performance of activities. They can also include any non-monetary assets that are essential for the completion of the item. Resource drivers: A measurement tool to associate cost with their respective activities or cost object resources drivers measure the quantity of resources consumed by an activity, typically a one-to-one relationship with the resource [1]. Figure 1 illustrates the hierarchical relationship among expense categories, activities, and products.

In [18], the authors proposed efficient and inexpensive steps for implementing ABC in small business. This procedure systematically provides the decision-maker with accurate cost information to establish corporate strategies, determine product cost, and improve the cost structure.

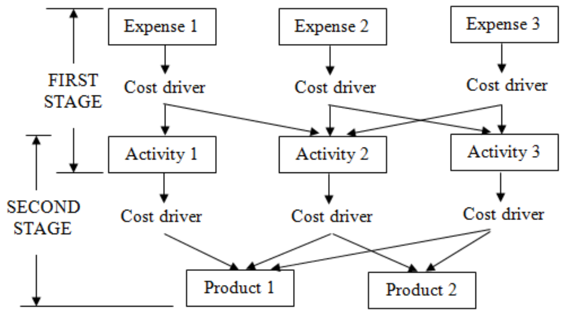

Figure 1: Relationship among expense categories, activities, and products [1].

ABC, by itself, is not enough for continuous improvement of the company. Activity Based Management (ABM) is a management philosophy that focuses on the planning, execution and measurement of activities and helps companies to survive in the competitive world of business. ABM allows leaders to examine non-value-added activities and make rational decisions to eliminate them. ABM relies on the ABC system to specify where non-value-added activities exist and to value the monetary benefits associated with their elimination [19, 20]. Management must institute a conscious process of organizational change and implementation if the organization is to receive benefits from the improved insights resulting from an ABC analysis [2]. Figure 2 illustrates the stages of ABM including monitoring, managing, and improving the performance of process [21].

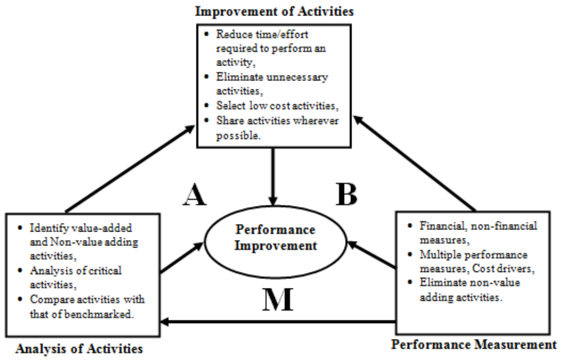

Figure 2: A conceptual framework for activity –based management [21].

Concrete is a primary material used in architecture and public work projects ranging in size from a single house to high-rise buildings. Concrete is a hardened building material created by combining a chemically inert mineral aggregate (usually sand, gravel, or crushed stone), a binder (natural or synthetic cement), chemical additives, and water. As concrete dries, it acquires a stone-like consistency that renders it ideal for constructing roads, bridges, water supply and sewage systems, factories, airports, railroads, waterways, mass transit systems, and other structures. The U.S. RMC industry had over $27 billion in annual sales and 107,000 employed workers in 2005. It has experienced solid growth during the past 15 years: real revenues have grown at an average annual rate of 3.8 percent since 1992 [22].

Concrete manufacturers expect their raw material suppliers to supply a consistent, uniform product. At the cement production factory, the proportions of the various raw materials that go into cement must be checked to achieve a consistent kiln feed, and samples of the mix are frequently examined using X-ray fluorescence analysis [22]. The strength of concrete is probably the most important property that must be tested to comply with specifications. To achieve the desired strength, workers must carefully control the manufacturing process, which they normally do by using statistical process control. The American Standard of Testing Materials and other organizations have developed a variety of methods for testing strength. Quality control charts are widely used by the suppliers of ready-mixed concrete and by the engineer on site to continually assess the strength of concrete. Other properties important for compliance include cement content, water/cement ratio, and workability, and standard test methods have been developed for these as well.

RMC is not only a product, it is a service, and each year about 20 million cubic meters of concrete are delivered in truck-mixers [23]. The truck-mixers have developed since the late 1940s from a mobile site mixer into specialized vehicle capable of mixing, delivering and distributing concrete in a very economic manner. Indeed, in the viability of RMC depends on the efficient utilization of the specialized truck-mixer fleet [24]. Although truck-mixer vehicles available in the range from 2 to 9 cubic meters capacity, the majority in use have a load capacity of 6 cubic meters of concrete. With "shelf life" of only a few hours, RMC is very much a local delivery service with an average distance from the depot to point of delivery of about 8 km.

Delivery cost, including the question of economy of scale, has been of interest to decision makers in different transportation sectors for many years. Managers need to have enough information about their cost to make the right decision about the type of services to provide and the prices to charge [25]. There are many approaches to estimate the cost per km for trucks. Each of them employs a different methodology and models to calculate the variable cost of operating trucks. Fuel, repair and maintenance, tire, depreciation, and labor cost are the most important cost that are considered to estimate operating cost per km. Daniels [26] divided vehicle operating cost into two different categories, running cost and standing cost. Running cost includes fuel consumption, engine oil consumption, tire cost, and maintenance cost. Standing cost includes license, insurance, interest charges. Daniels considered speed as the most important factor in fuel consumption and found maintenance cost rise with increasing speed. If fuel consumption and maintenance cost change, operating cost will change as well. Vehicle size is another factor that affects fuel consumption and it will change operating cost. By using average axle number for each firm we can include vehicle size in our model.

Watanatada and Dhareshwar [27] divided the variables that affect the truck operating cost to the following categories: 1. Truck characteristics e.g., weight, engine power, and maintenance. 2. Local factors e.g., speed limit, fuel price, labor cost, and drivers' attitude. 3. Road characteristics e.g., pavement roughness, and road width. Operating cost is considered a function of road characteristics and so is policy sensitive. Barnes and Langworthy [28] estimated operating cost for commercial trucks based on fuel, repair, maintenance, tires and depreciation cost. The authors also considered adjustment factors for cost, based on pavement roughness, driving conditions and fuel price changes. Moreover, they estimated the average truck operating cost per *km* at $0.27 cents not including labor cost. For a labor cost of around $0.22 per *km*, the total operating cost using Barnes' model adds up to $0.49 per *km*. Hashami [29] developed and tested a linear model in her thesis of Operating Cost for Commercial Vehicle Operators. Details of her contribution are presented in section 3.

3. Cost Model for RMC

To estimate the cost of a demanded volume of RMC, it is necessary to cost required materials, labor involved, fuel and maintenance needed, plant and ancillary equipment hired and depreciated, and delivery of RMC to customer site. The proposed cost model subdivides the cost of RMC into three main cost categories including 1) On-floor cost: the model utilizes a step-by-step ABC procedure from literature, 2) Cost of delivery: a new model for costing the delivery of RMC is proposed, and 3) Cost associated with riding RMC scrap: the model assigns cost to scrap based on the location where RMC got spoiled. To illustrate, if RMC is spoiled in the factory, only on-floor cost will be charged. On the other hand, the sum of on-floor and delivery cost is charged if RMC is spoiled in its way to customer.

3.1. On-floor cost: The ABC model

Figure 3 illustrates the proposed ABC model based on procedures for producing RMC and the related plant processes. A common procedure to identify cost activities is to interview people who work in overhead departments and ask them to describe their major activities. Activity centers are established such that all activities related to accomplishing a particular attribute are grouped. A good rule of thumb is not to have more than 20-25 activity centers for an ABC project [2]. Table 1 presents RMC main in-plant activities and their cost centers.

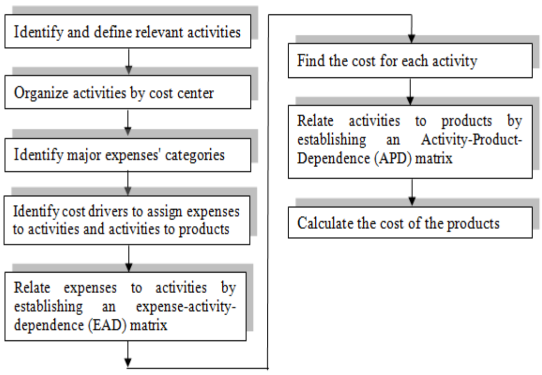

Figure 3: On-floor ABC procedure.

For a typical RMC plant, Table 2 presents expense categories included in the income statement of the company. Moreover, the table presents the cost driver(s) of each category. Once the main expenses have been defined, a total cost of each expense can be found. Sample cost values are shown in Table 2 as obtained from the case study. This helps management and reengineering-teams efforts to minimizing expenses. Notice that equipment complexity is used as a cost driver for maintenance since more complex machines usually require more effort and time. The complexity of the machine may be measured by the number of components of the machine or the amount of technology contained in that machine. Miscellaneous costs (MC) are expenses that cannot be itemized or traced back to specific activities. Hence, miscellaneous cost are estimated or forecasted for the coming year (MC_{t+1}) based on historical data and are divided equally over all overhead activities.

Table 1: Main activities and their cost centers.

Activities	Cost centers
1. Electrical maintenance 2. Vehicle maintenance 3. Riding scrap 4. Equipment and plant maintenance	Maintenance center
5. Management 6. Guard work 7. Marketing and advertising	Administration center
8. Purchasing 9. General accounting	Accounting center
10. Material receiving and shipping 11. Employee transportation	Transportation center
12. Weighing 13. Mixing Operation	Preparation of raw material
14. Quality Assurance	Development center

Table 2: Expense categories, their cost drivers and yearly cost

Expense category	**Cost driver**	**Cost** ($/year)
Overhead Expenses		
Salaries	Total labor salary per year	153,672
Overtime	Total labor overtime per year	67,976
Depreciation	550Money use of resources	173,
Office Expense	Level of use of office resources (%)	3,655
Utilities	Total cost per year	1,800
Transport	Distance (km)	10,440
Maintenance	Equipment complexity	49,407
Insurance	Cost of resource used by activity	34,860
Licenses	Type of licenses	4,490
Research and development	Cost of resource used by activity	4,950
Communication	Cost of resource used by activity	10,354
Miscellaneous	Total cost per year	300
	Total	515,454
Materials' Cost		
Portland Cement	Unit mass	1,772,550
Fine Aggregate	Unit mass	264,690
Coarse Aggregate	Unit mass	263,385
Water	Unit mass	38,466
Chemical Component	Unit mass	89,100
	Total	2,428,191

To relate expenses to activities, an Expense-Activity-Dependence (EAD) matrix is established [18]. To illustrate, the activities that contribute to each expense are identified and the EAD matrix is created. The expense categories represent the columns of the EAD matrix, whereas the activities represent the rows. If activity i contributes to the expense category j, a checkmark"√" is placed in the cell i, j. Follows, each expense category is traced back to activities and each expense category is divided among activities according to the proportion of contribution. The check marks in the EAD matrix are replaced by the proportions of contribution such that each column of the EAD matrix must add up to 1, implying that the entire expense category is spread across the activities.

Equation 1 presents the total cost $TCA(i)$ of activity i where, j is the number of expense categories and $EAD(i,j)$ is the entry i,j of the EAD matrix.

$$TCA(i) = \sum_{j=1}^{J} EAD(i,j) \quad (1)$$

To obtain the overhead cost of a unit volume of an RMC product, the activities consumed by the product are identified and the Activity-Product-Dependence (APD) matrix is created. If product k (row entry) consumes the activity i (column entry), a check-mark is placed on the cell k,i. Follows, check marks in the APD matrix are replaced by the estimated proportions of consumption of product k from activity i such that each column of the APD matrix must add up to 1. These proportions are traced over the demand years and are assumed to be constant over the years. Equation 2 illustrates the overhead cost CO_k of a unit volume of product k where, N is Number of activities and $APD(k, i)$ is the entry k, i of the APD matrix.

$$CO_k = \sum_{i=1}^{N} TCA(i) \times APD(k,i) \quad (2)$$

On-floor cost (CF_k) of a unit volume of product k is then computed by adding the cost of overhead activities to the cost of raw materials as illustrated in equation 3. Where, M is the number of materials' types, u_{mk} is the amount of material m used to produce a unit volume of product k, and c_m is the unit cost of material m. To estimate CF_k for the coming year ($t+1$), overhead expenses and materials' volumes and cost are to be foreseen based on expert opinion, regression models or time series analysis.

$$CF_k = CO_k + \sum_{m=1}^{M} u_{mk} c_m \quad (3)$$

3.2. Delivery cost model:

The RMC supply process can be divided into five major components including RMC production, product loading, transporting RMC to site, RMC placement, and truck return. The RMC production and placement activities must be connected by trucks to form an operation cycle. Since RMC is a perishable and un-storable material, it cannot be generated and stored in advance. Hence, time is critical when it comes to the delivery process of RMC because as time passes, the properties of fresh concrete change quickly, causing it to become unusable within few hours. If the truck travel time exceeds the cold-joint time (the time within which the concrete hardens), the concrete is rendered useless and must be dumped, which raises the operating cost. Therefore, to conform to quality and legislation requirements, RMC must be poured within a set time constraint. In practice, truck service is limited to a given region; the trucks must be carefully dispatched in order to prevent the cold joint process. Consequently, RMC production scheduling and truck-dispatching not only affect transshipment efficiency, but also the operating cost. A number of limitations on the RMC must be taken into account before building a model for RMC delivery:

- The materials are batched at a central plant, and the mixing begins at the plant, so the traveling time from the plant to the site is critical over longer distances.
- Access roads and site access have to be able to carry the weight of the truck and load.
- RMC should be placed within 2 hours of batching to avoid cold-joint. Concrete is still useable after this point but may not conform to the relevant specifications.
- A minimum volume of RMC must be available in the truck during each trip.

Hashami [29] developed a general linear model (Equation 4) to obtain the total annual cost of delivery taking into account the correlations among the delivery variables. The model treats all customers equally, which means that near and far customers will pay the same amount of money.

$$C = B\,O + B1\,(K/T) + B2\,T + B3\,P + B4\,O + B5\,H \quad (4)$$

Where: C: Total annual cost, O: 1 if the firm is the owner/operator, 0 otherwise, K: Overall travel distance in kilometers, T: Number of truckloads, P: 1 if firm is assessed a financial penalty for late delivery, 0 otherwise, H: 1 if the firm hauls more than one product, 0 otherwise, and B, $B1$, $B2$, $B3$, $B4$, and $B5$ are the associated cost.

The paper presents a model for costing the delivery of RMC to the customer as a function of the travel distance and traffic conditions. To this end, the travel distance (l, in kilometers) is penalized by a factor ($w \geq 1$) to account for traffic conditions. Equation 5 illustrates the cost of delivery (CT_k) of a truck load of product k where, w_h and w_r are traffic factors for the hauling and return trip respectively, and c_h and c_r are the cost ($/km) for the hauling and return trip respectively.

$$CT_k = l_h\, w_h\, c_h + l_r\, w_r\, c_r \quad (5)$$

3.3. Cost of riding RMC wastes:

Concrete waste is a material that is no longer valuable in its current state for its intended use and is either discarded or recycled. Reasons for RMC spoilage include failure to confirm to required RMC specifications, or delay during which cold-joint takes place. Such delays are due plant break down, truck break down, or traffic conditions. Potential cost associated with spoilage management include the on-floor cost of wasted concrete (CO_k), and delivery cost to the location where spoilage took place (CT_k); CT_k = 0 if spoilage took place at the RMC plant. Equation 6 illustrates the proposed costing model (CS_t) of riding spoiled amounts of all RMC products during year t. In this paper, we use forecasting methods to predicate the spoilage amounts (VS_{kt+1}) of product k for the coming year ($t+1$) based on historical data. The estimated spoilage cost per year (CS_{t+1}) is then divided over the estimated volume of production for all RMC products (TD_{t+1}) during that year to obtain the spoilage cost per unit volume. TD_{t+1} is estimated using forecasting methods based on demand history.

$$CS_t = \sum_k (CF_k + CT_k) VS_{kt} \tag{6}$$

3.4. Penalties for late deliveries and volume discounts:

The cost associated with delayed concrete deliveries (*CP*) cannot be itemized or traced back to specific activities. Hence, *CP* cost are estimated or forecasted for the coming year and are divided over TD_{t+1} to obtain the related cost per unit volume. On the other hand, volume discounts are traceable cost and are part of the marketing policy of the company. Volume discounts may take various formats including fixed discount per order, percentage discounts based on volume, and rough discounts based on negotiations with the customer. To this end, the proposed model does not include volume discounts and leaves the room to company on deciding the amount of discount on an order as a reduction from its profit.

3.5. Total cost of RMC:

Equation 7 presents the total cost (C_{kt+1}) for producing and transporting D_k unit volumes of RMC product k for the year $t+1$. Where, c is the capacity of the truck, and $\left\lceil \frac{D_k}{c} \right\rceil$, number of required truck loads, is the nearest integer greater than or equal to $\frac{D_k}{c}$.

$$C_{k\,t+1}(D_k) = CF_{k\,t+1}\, D_k + CT_{k\,t+1} \left\lceil \frac{D_k}{c} \right\rceil + \left(CS_{t+1} + CP_{t+1}\right)\frac{D_k}{TD_{t+1}} \tag{5}$$

Note that real time costing of product k is composed of 1. Estimated overhead cost, 2. Today's cost of materials, 3. Today's cost of delivery, 4. Estimated cost of spoiled RMC, and 5. Estimated cost of penalties. To compute the true cost of a product during a previous year, financial records are consulted to provide true expenses. Moreover, true demands replace estimated ones.

4. Model Verification

To verify the usability of the model, we implement the proposed costing model on a local RMC plant and results are compared to that obtained using the traditional costing model of the company. To identify and classify activities, trace expenses to activities, and trace activities' cost to products, departments in the RMC plant are visited, employees are interviewed, and organization chart is studied. The main identified activities include maintenance (electrical, cars and bulldozer, equipments and plant), management, purchasing, general accounting, receiving, employee transportation, weighing, mixing, quality assurance, waste management (riding scrap), and guard work (plant equipment and inventory). A thorough investigation of related expenses show that expenses of the activities can be categorized into salaries, overtime, office, communication, research and development, insurance, licensing, fuel and oil, raw materials, water and electricity, and miscellanies.

To obtain the on-floor cost of products, we track expenses of the company to products through expense categories and related activities. Table 2 illustrates expense categories and their cost. Expense categories are related to activities as shown in the EAD Matrix, Table 3. Dollar values for activity-expense intersection and total cost per activity are shown in Table 4.

Table 3: Expense-Activity-Dependence (EAD) Matrix.

Activity	**Expense Categories**											
	Salaries	Overtime	Depreciation	Office Expense	Utilities	Transport	Insurance	Communication	Licenses	Maintenance	R&D	Miscellaneous
Electrical Maintenance	0.081	0.114			0.083			0.081		0.248	0.101	0.083
Vehicle Maintenance	0.025	0.038			0.083			0.041		0.029	0.141	0.083
Equipments and plant Maintenance	0.119	0.170			0.083	0.073		0.122		0.711		0.083
Management	0.158		0.005	0.337	0.083	0.181	0.001	0.219	0.022	0.005	0.404	0.083
RM receiving	0.019	0.024			0.083		0.001	0.023				0.083
General accounting	0.081		0.005	0.237	0.083	0.141	0.001	0.077	0.022	0.002	0.091	0.083
Purchasing raw material	0.033		0.004	0.027	0.083	0.141	0.001	0.035	0.022		0.061	0.083
Employee transportation	0.018	0.024	0.004		0.083	0.280	0.001		0.022	0.003		0.083
Weighing	0.018	0.025			0.083							0.083
Mixing	0.388	0.543	0.977		0.083		0.990	0.348	0.880			0.083
Quality assurance	0.041	0.061	0.004	0.399	0.083	0.141	0.001	0.023	0.022	0.002	0.202	0.083
Waste management	0.002	0.001	0.001		0.001	0.010	0.001		0.010			0.002
Guard work	0.017				0.083	0.033		0.031				0.083

Table 4: Dollar values for activity-expense intersections and total activity cost.

Activity	Expense Categories												Cost ($/Year)
	Salaries	Overtime	Depreciation	Office Expense	Utilities	Transport	Insurance	Communication	Licenses	Maintenance	R&D	Miscellaneous	
Electrical Maintenance	12,447.43	7,749.26			149.850			838.674		12,252.94	499.950	24.950	33,963.06
Vehicle Maintenance	3,841.80	2,583.09			149.85			424.51		1,432.80	697.95	24.95	9,154.96
Equipments and plant Maintenance	18,286.97	11,555.92			149.85	762.12		1,263.19		35,128.38		24.95	67,171.37
Management	24,280.18		867.75	1,231.74	149.85	1,889.64	49.80	2,267.53	98.78	247.04	1,999.80	24.95	33,107.04
RM receiving	2,919.77	1,631.42			149.85		49.80	238.14				24.95	5,013.93
General accounting	12,447.43		867.75	866.24	149.85	1,472.04	49.80	797.26	98.78	98.81	450.45	24.95	17,323.36
Purchasing raw material	5,071.18		694.20	98.69	149.85	1,472.04	49.80	362.39	98.78		301.95	24.95	8,323.82
Employee transportation	2,766.10	1,631.42	694.20		149.85	2,923.20	49.80		98.78	148.22		24.95	8,486.52
Weighing	2,766.1	1,699.4			149.85							24.95	4,640.30
Mixing	59,624.74	36,910.97	169,558.35		149.85		34,511.40	3,603.19	3,951.20			24.95	308,334.65
Quality assurance	6,300.55	4,146.54	694.20	1,458.35	149.85	1,472.04	49.80	238.14	98.78	98.81	999.90	24.95	15,731.91
Waste management	307.34	67.98	173.55		1.80	104.40	49.80		44.90			0.60	750.37
Guard work	2,612.42				149.85	344.52		320.97				24.95	3,452.72

To cost the various products, P150, P200, P250, P300, and P350, of the company for 2009, the activities consumed by each product are identified and the Activity-Product Dependence (APD) matrix is created. It is noticed that the only difference between these products is the percentage of raw materials consumed by the product. Hence, the dollar expense of a product type k from a certain activity, excluding materials, equals the relative yearly demand of that product type ($\frac{D_k}{TD}$) multiplied by that expense. To illustrate, the relative demands of P150, P200, P250, P300, and P350 are 20%, 50%, 20%, 10%, and 0% respectively. Therefore, the $33,963 of electrical maintenance, see Table 5, is subdivided among P150, P200, P250, and P300 as $6,792.61, $16,981.53, $6,792.61, and $3,396.31, respectively. Therefore, the overhead cost per unit volume of each product (CO) equals $5.727.

Table 5 presents the yearly demands and materials consumption for the four products. Table 6 presents estimated and traditional cost per cubic meter of materials of the company's RMC products. The traditional on-floor costing method of the company takes into account today's materials' cost and adds a flat overhead cost of $6.00. Where, the unit cost of a material is obtained by dividing the total cost of that material over the total amount of material used to produce all product types over the year. To illustrate, the total weight of coarse aggregate used to produce the 90,000m^3 of RMC products equals 52,677,000 (18,000 × 593 + 45,000 × 574 + 18,000 × 559 + 9,000 × 679) kilograms. Hence, the average unit cost of coarse aggregate equals the per-year cost of coarse aggregate ($263,385) divided by the total weight of the material used during the year. This yields a unit cost of $0.005 per kilogram of coarse aggregate. Note that P250 cost more than P300 although it is offered to customers at a lower price. Obtained results illustrate that the RMC company over estimated their yearly production cost by more than $24,000 since no scraped mixes or penalties were reported over that year. On the other hand, a scrap level of more than 0.8% (about 720m^3) of RMC mixes at the average price of $33.457 may justify the difference.

Table 5: Yearly demand and consumption of materials for RMC products.

Products	Yearly Demand (m^3)	Cement (kg/m^3)	Fine Aggregate (kg/m^3)	Coarse Aggregate (kg/m^3)	Water (Lit/m^3)	Chemical Component (Lit/m^3)
P150	18,000	235	605	593	215	4.5
P200	45,000	300	585	574	215	5
P250	18,000	360	570	559	215	5
P300	9,000	340	607	679	202	5.5

Table 6: On-Floor Cost per m^3 of RMC products.

Products	**Proposed**			**Traditional**		
	Materials	**Overhead**	**On-Floor**	**Materials**	**Overhead**	**On-Floor**
P150	22.595	5.727	28.322	22.595	6.000	28.595
P200	26.725	5.727	32.452	26.725	6.000	32.725
P250	30.475	5.727	36.202	30.475	6.000	36.475
P300	30.034	5.727	35.761	30.034	6.000	36.034

For delivery operations, the company limits their maximum reach to customers' sites within an 80km radius to prevent cold joint. Deliveries are made using mixing trucks with a maximum capacity of 9m^3. Customers within the circle of 20km are charged $6 per trip. Beyond the 20km limit, the customer is charged an extra $0.25 – $0.30 per kilometer per trip depending on traffic conditions. For the purpose of this research, company experts estimated a markup percentage of 35% to estimate traditional delivery cost. Moreover, they estimated the cost for hauling and returning at $0.175 and $0.125 per kilometer per trip, respectively. Furthermore, they estimated the impact of traffic at w_h = 1.25 and w_r = 1.15. Table 7 illustrates examples of the delivery charges of volumes of RMC to various customers' locations. Note that the traditional system is not sensitive to distances within the 20km limit. Moreover, note that while the company over estimates their delivery costs for various scenarios, they largely under estimate it for the rest of the scenarios especially for long distance deliveries. Summing up on-floor and delivery cost yields the total cost of RMC products. Figure 4 shows the difference in total cost (Traditional – Proposed) per cubic meter of RMC for various combinations of demand, distance, and traffic conditions. Where, 5, 9, 12, 25, and 45 represent delivery volumes, and NT stands for "no traffic" and WT for "with traffic" conditions.

Table 7: Traditional vs. proposed delivery costing systems.

Volume (m^3)	# of km	Without Traffic		With Traffic	
		Traditional	Proposed	Traditional	Proposed
5	5	0.889	0.300	0.889	0.363
	14	0.889	0.840	0.889	1.015
	23	1.000	1.380	1.022	1.668
	48	1.926	2.880	2.133	3.480
9	5	0.494	0.167	0.494	0.201
	14	0.494	0.467	0.494	0.564
	23	0.556	0.767	0.568	0.926
	48	1.070	1.600	1.185	1.933
12	5	0.741	0.250	0.741	0.302
	14	0.741	0.700	0.741	0.846
	23	0.833	1.150	0.852	1.390
	48	1.605	2.400	1.778	2.900
25	5	0.533	0.180	0.533	0.218
	14	0.533	0.504	0.533	0.609
	23	0.600	0.828	0.613	1.001
	48	1.156	1.728	1.280	2.088
45	5	0.494	0.167	0.494	0.201
	14	0.494	0.467	0.494	0.564
	23	0.556	0.767	0.568	0.926
	48	1.070	1.600	1.185	1.933

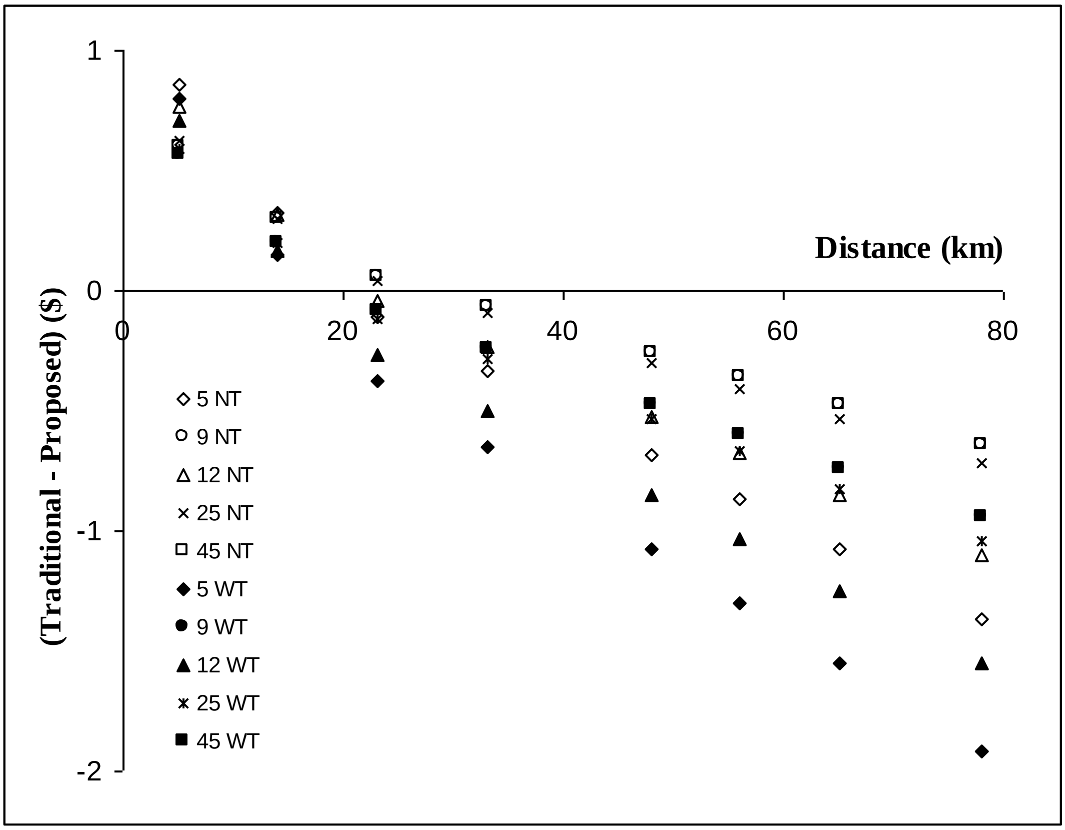

Figure 4: Differences between traditional and proposed costing systems.

To stay competitive, companies put efforts to reduce their expenses through the better management of their resources. Improvement efforts should take into account the value that the process/activity contributes to the final product. Hence, activities with no added value should be eliminated. Moreover, efforts should focus on simplifying value-added activities to save time, effort, and cost. The expense categories and their cost shown in Table 2 show that raw materials contribute to the maximum percentage of expenses and cannot be changed because of specifications. Hence, improvement efforts should focus on 1. Improving work schedules to reduce overtime, 2. Adapt preventive and predictive maintenance to ensure optimum levels of availability, enhance the performance of machines and vehicles, and decrease the rate of depreciation, and 3. Improve the costing practices adapted in the company.

5. Summary and Conclusions

The paper presents a model for costing RMC based on the type of mix and customer's information. The model divides the cost into on-floor, delivery, waste riding, and penalties related cost. The model utilizes ABC to identify activities and assign cost of resources products according to the actual consumption of each product from recourses. ABC helps management arrive at the true cost of a product to avoid under or over costing. Moreover, the analysis of expense categories and their cost help management set their improvement priorities. The model accounts for product and vehicle constraints including expected life of the mix during transportation and the capacity of the vehicle.

The proposed model is applied at a local RMC company where cost differences were recognized compared to the current costing model of the company. While on-floor and scrap management cost are similar and depend only on demand volumes and product type, delivery cost take into account distance and traffic conditions to customer location. This helps management distinguish among customers in charging delivery cost. Although materials account for the largest percentage of expenses, RMC management should investigate potentials to reduce or eliminate some elements for each expense. Among the many, savings associated with depreciation and maintenance can be easily obtained through applying maintenance best practices.

References

[1] Cooper, R., and Kaplan, R., 1988, Measure Cost Right: Make the Right Decisions. Harvard Business Review.

[2] O'Guin, M., 1991, The Complete Guide to Activity-Based Costing. Prentice Hall, NJ.

[3] Sullivan, W., 1992, A New Paradigm for Engineering Economy. The Engineering Economist, 36(3).

[4] Harsh, M., 1993, The Impact of Activity Based Costing on Managerial Decisions: An Empirical Analysis. Ph.D. Dissertation, Virginia Polytechnic Institute and State University, Blacksburg, VA.

[5] Liggett, H., Trevino, J., and Lavelle, J., 1992, Activity-Based Cost Management Systems in an Advanced Manufacturing Environment. Economic and Financial Justification of Advanced Manufacturing Technologies, H. R. Parsaei, ed., New York: Elsevier Science Publishers.

[6] Cooper, R., 1988a, The Rise of Activity-Based Costing- Part One: What is an Activity- Based Costing?. Journal of Cost Management, 7(3).

[7] Cooper, R., 1988b, The Rise of Activity-Based Costing- Part Two: When Do I Need an Activity Based Cost System?. Journal of Cost Management, 7(4).

[8] Nachtmann, H., and Al-Reifai, M, 2004, An Application of Activity Based Costing in the Air Conditioner Manufacturing Industry. The Engineering Economist, 49

[9] Baykasoglu, A., and Kaplanoglu, V., 2008, Application of Activity-Based Costing to a Land Transportation Company: A Case Study. International Journal of Industrial Economics, 116(2)

[10] Lee, T., and Kao, J., 2001, Application of Simulation Technique to Activity-Based Costing of Agricultural Systems: A Case Study. Agricultural Systems, 67(2)

[11] Lievens, Y., Van Den Bogaert, W., and Kesteloot, K., 2003, Activity-Based Costing: A Practical Model for Cost Calculation in Radiotherapy. International Journal of Radiation Oncology*Biology*Physics. 57(2)

[12] Grandlich, C., 2004, Using Activity-Based Costing in Surgery. AORN, 79(1)

[13] Johnson, H., and Kaplan, R., 1987, Relevance Lost: The Rise and Fall of Management Accounting. Harvard Business School Press, Boston.

[14] Cooper, R., 1987, Does Your Company Need a New Cost System?. Journal of Cost Management. 6(3).

[15] Holmen, J., 1995, ABC vs. TOC: It's a Matter of Time. Management Accounting.

[16] Kee, R., 1998, Integrating ABC and the Theory of Constraints to Evaluate Outsourcing Decisions. Journal of Cost Management, 12(1)

[17] Kaplan, R., 1989, Introduction to Activity Based Costing. NAA Conference, Global Solutions to Global Problems II, Boston, MA.

[18] Roztocki, N., Valenzuela, J., Porter, J., Monk, R., and Needy, K., 1999, A Procedure for Smooth Implementation of Activity Based Costing in Small Companies. ASEM National Conference Proceedings, Virginia Beach.

[19] Raffish, N., and Turney, P., 1991, The CAM-I Glossary of Activity-Based Management, Arlington: CAM-I.

[20] Roberts, M., and Silvester, K., 1996, Why ABC Failed and How It May Yet Succeed?. Journal of Cost Management, 9.

[21] Gunasekaran A., McNeil, R., and Singh, D., 2000, Activity – Based Management in a Small Company: A Case Study. Production Planning and Control, 11.

[22] Mindess, S., Young, J., and Darwin, D., 2003, Concrete, 2nd Edition. Prentice-Hall Inc., Upper Saddle River, NJ.

[23] Tommelein, I., and Li A., 1999, Just-in-time concrete delivery: mapping alternatives for vertical supply chain integration. University of California, Berkeley.

[24] Schmid, V., 2007, Trucks in movement: hybridization of exact approaches and variable neighborhood search for the delivery of ready-mixed concrete. PhD thesis, University of Vienna.

[25] Braeutigam, R., 1999, Learning about Transport Cost, Essay in Transportation Economics and Policy. Brooking Institution Press, Washington, D.C.

[26] Daniels, C., 1974, Vehicle operating cost in transport studies: With special reference to the work of the EIU in Africa. Economist Intelligence Unit, London.

[27] Watanatada, T., and Dhareshwar, A., 1987, Vehicles Speeds and Operating Cost, Washington, D.C., The World Bank.

[28] Barnes, G., and Langworthy, P., 2003, The Per-Mile Cost of Operating Automobiles and Trucks. Forthcoming report, Minnesota Department of Transportation.

[29] Hashami, M., 2004, Operating Cost for Commercial Vehicle Operators in Minnesota, Spring.

JJMIE

Volume 6, Number 2, April 2012
ISSN 1995-6665
Pages 175 - 181

Jordan Journal of Mechanical and Industrial Engineering

Effect of Direct Extrusion on the Microstructure, Microhardness, Surface Roughness and Mechanical Characteristics of Cu-Zn-Al Shape Memory Alloy, SMA.

S. M. Al-Qawabah[a,*]

[a]Tafila Technical University, Mechanical Engineering Department, Amman 11942, P.O.Box 13720, Jordan

Abstract

Shape memory alloys (SMA) are now widely used in many engineering applications especially in robotic, aerospace and vibration control area.The main problem arises from the weakness of their mechanical characteristics. Therefore, this study is directed towards enhancing the mechanical properties through severe plastic deformation. In this paper, the direct extrusion process was chosen to provide the required cold work for this purpose. A direct extrusion die was designed and manufactured to be used in this investigation for improving mechanical behavior of the Cu-Zn-Al shape memory alloy was. The general microstructure, microhardness, surface roughness, and compression tests were performed on specimens from the produced Cu-Zn-Al shape memory alloy both in the as cast and after extrusion conditions. It was found that a pronounced enhancement in the mechanical characteristics of the produced Cu-Zn-Al shape memory alloy, after extrusion was achieved. The microhardness increased by 105.2 %, the flow stress was enhanced by 100 % at 0.2 strain and finally the surface roughness was reduced by 81.8 %.

Keywords: Extrusion; Microstructure; Microhardness; Cu-Zn-Al shape memory alloy; Mechanical behavior; Surface roughness

1. Introduction

Shape memory alloy later referred to as SMA in this paper are alloys that can return to original shape by changing the temperature. Among a large number of SMA developed during the last two decades the Cu-based alloys serve as economic alternative to the Ti-Ni shape memory alloys due to their low cost, better electrical and thermal conductivities. The Cu-Zn-Al are now becoming the most popular Cu-based SMA. However, they suffer poor ductility problems, the martinisitic stability and the intergranular crack which are disadvantageous to their application. Many attempts have been made to improve their mechanical proprieties and the thermal stability of the martenstic transformation [1].

1.1. Properties of shape memory alloys:

Shape recovery is due to solid-to-solid phase transformation from martensite to austenite. Austenite crystalline structure is regained upon heating, returning to its original shape [2]. SMA deforms easily under stress due to twin boundaries propagating throughout the structure in the direction of stress [6]. Fig.1 shows the details of shape memory alloy transformation

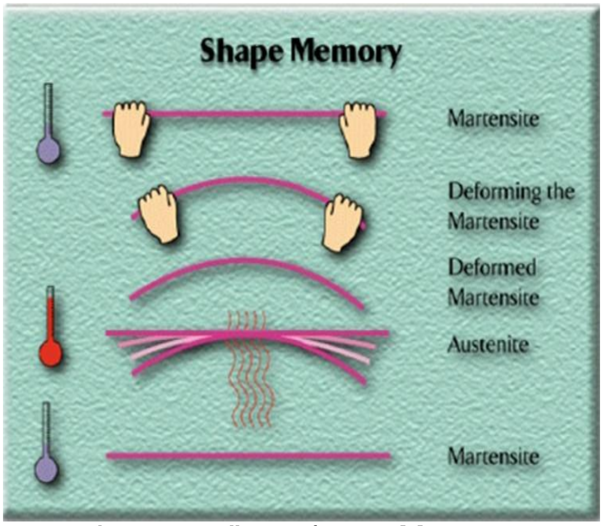

Figure 1: Shape memory alloy transformation [3].

The relationship between the applied loads and the temperature can be seen in Fig.2.

* Corresponding author. e-mail: safwan_q@yahoo.com

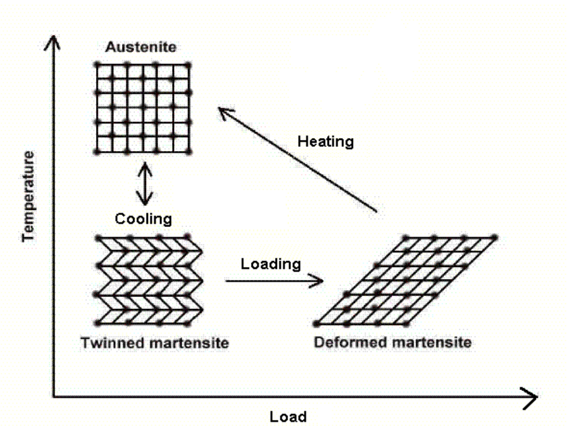

Figure 2: Load-temperature relationship of a shape memory alloy [1].

Copper–based SMA have the advantage of being made from relatively cheap materials using conventional metallurgical processes such as induction melting. Nitrogen or other inert gases should be used for shielding purposes over the melt and during pouring to prevent zinc evaporation. The handicap of these SMA is that martensitic phase is stabilized by long term aging at room temperatures. This causes an increase in transformation temperature over time [5,6]. These SMA are widely used in the engineering applications especially in the robotic, aerospace and vibration control areas. To design and optimize the applications of these alloys, a clear understanding of its behavior and characteristics is required. The phase temperatures for the shape memory alloys such as the austenite start (As), austenite finish (Af), martensite start (Ms) and martensite finish (Mf) are the basic temperatures that should be determined before designing the system. Unfortunately the properties provided by the manufacturer are normally not complete. So further investigation or testing are required.[7,8,9,10,11,12].

The main objective of this investigation is to enhance the mechanical characteristics of Cu-Zn-Al shape memory alloy.

2. Materials, Equipment and Experimental Procedures

2.1. Materials:

Mixing of three powder materials namely; pure copper, pure Zinc, and pure aluminum in approperate percentages are normally used to prepare the Cu-Zn-Al SMA. Its chemical composition by weight is shown in Table1.

Table 1: Chemical composition by weight of Cu-Zn-Al shape memory alloy.

Material	Cu	Zn	Al
wt. %	70 %	26 %	4%

2.2. Experimental procedures:

2.2.1. Preparation Cu-Zn-Al shape memory alloy:

The Cu-Zn-Al SMA was prepared by melting the precalculated amount of high purity copper powder at 1250 °C, then the pre-calculated amounts of pure Al and pure Zn were added to the melt in a graphite crucible. The melt was steered for 2 minutes then poured to solidify in steel mold, and cooled in air. The Cu-Zn-Al shape memory alloy was synthesized in the form of 14 mm diameter and 70 mm length cylindrical rods using melting and casting technique.

2.2.1.1. Recommended procedure to produce the Cu-Zn-Al shape memory alloy [1]:

To produce the shape memory alloy the following procedures as reported in [1] was adopted in the following sequence.

- Heating the cast (Cu- Zn- Al) to 820 ˚C for 10 min.
- Quenching the cast material by oil at 120 ˚C for 5 min.
- Cooling the cast in water at room temperature.

2.2.2. Metallurgical examination:

In this test the general microstructures Cu-Zn-Al SMA in the as cast and after extrusion condition were determined by mounting a specimen of each condition in baklite, ground, polished and etched using enchant made of 1.5% gm powder Fe Cl3, 96.5% wt., CH3COOH and 2% wt. HNO3 by weight. Photomicrographs were obtained using the NIKON 108 type microscope at magnification of 500x.

2.2.3. Determination of average grain size:

Line intercept method was used in determing the average grain size using digital microhardness tester (model HWDM-3) at 400x magnification.

2.2.4. Microhardness tests:

Microhardness measurements were taken on the surface of the polished specimens both in the as cast and after extrusion conditions at magnification 400x using HWDM-3 AT 300 gm load. Five microhardness readings were taken on the surface of each specimen from which the average microhardness was obtained.

2.2.5. Compression tests:

Cylindrical specimens of 10 mm diameter and 10 mm length of aspect ratio =1 were machined using Boxford CNC lathe machine at the same cutting conditions [depth of cut, spindle speed, feet rate]. Compression test was carried out at room temperature using (Quasar 100 Universal Testing Machine of 100 KN capacity) at 1*10-3s-1 strain rate. The load-deflection curve was obtained for each specimen, from which the true stress-true strain curve was determined. The compression test was repeated three times for each condition, and then the average of load-deflection curve was obtained.

2.2.6. Extrusion test:

The direct extrusion test was performed using the designhed and manufactured die on (Quasar 100 Universal Testing Machine of 100 KN capacity) at $1*10^{-3}s^{-1}$ strain rate as shown in the photographs of Fig.3 (a) and (b).

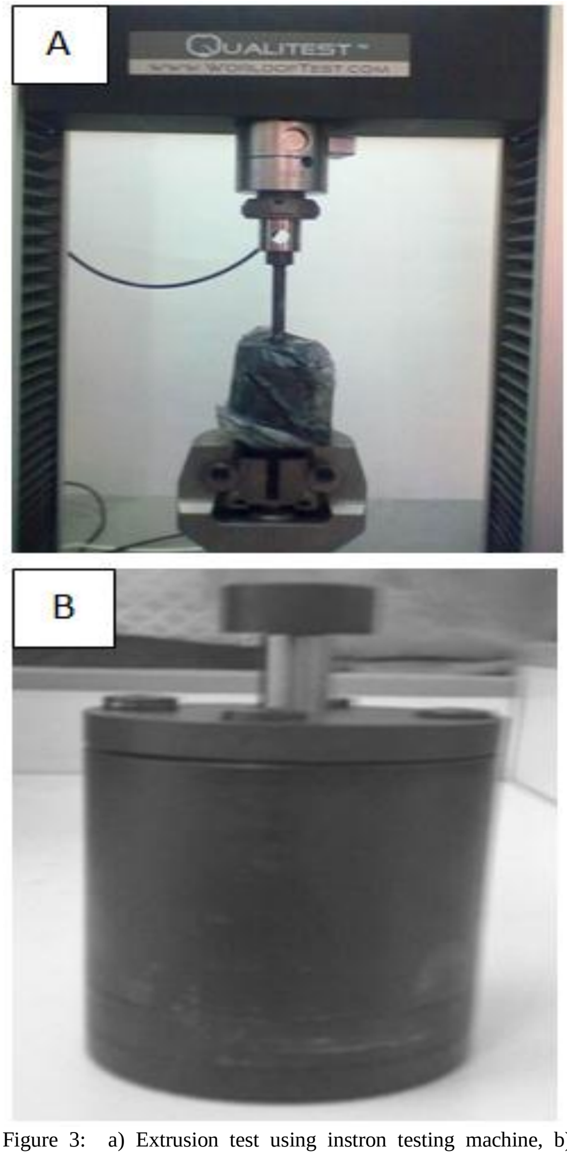

Figure 3: a) Extrusion test using instron testing machine, b) Forward extrusion die.

Fig.4 (a) and (b) shows photographs of the specimen in the as cast and after extrusion conditions. The diameter was reduced from 12 mm to 10 mm at extrusion ratio 1.44.

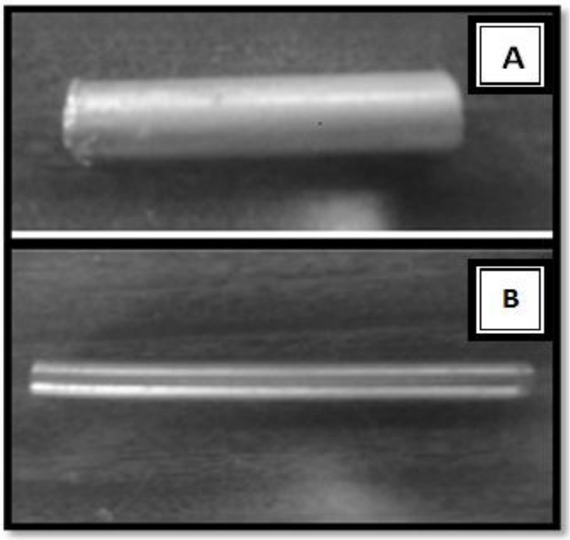

Figure 4: work part (a) as cast, (b) After extruded conditions.

3. Results and Discussion

In this section, the effect of the direct extrusion on the general microstructure, Vicker's microhardness, mechanical behavior, and surface roughness of Cu-Zn-Al shape memory alloy are presented and discussed.

3.1. Effect of Direct Extrusion on the Microstructure of Cu-Zn-Al SMA:

Figure 5 shows the general microstructure of Cu-Zn-Al SMA in the as cast condition, from which it can be seen the copper in the orange color and the Zn and Al in the dark color. The figure also indicates the uniform distribution of Zn and Al within the copper matrix. The average grain size of the Cu-Zn-Al SMA in the as cast conditions is 136 µm.

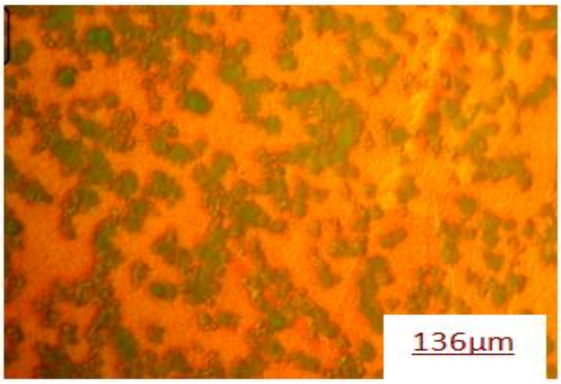

Figure 5: Photomicrograph of Cu-Zn-Al in the as cast at 200X.

The photomicrographs of Fig.6 (a-b-c-d) show the general shape of the grains in the as cast condition, which indicate an equiaxed grain type. Furthermore, It can also seen that there are square grains which indicates that the plastic deformation has occurred by twining, Fig. 6(c).

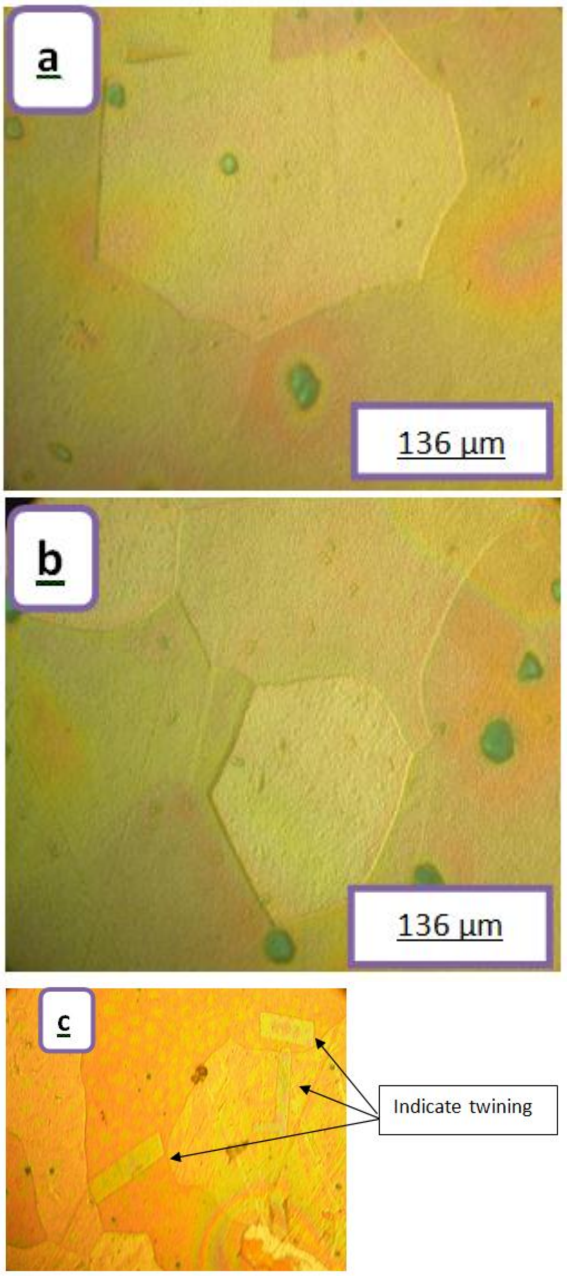

Figure 6: (a, b, c) photomicrographs showing the general microstructure of Cu-Zn-Al in the as cast condition at magnification of 500X.

Figure 7 shows the general microstructure of Cu-Zn-Al SMA after direct extrusion, from which it can be seen that the average grain size was reduced by 46.2 %. This may be explained by the enhancement in the mechanical characteristics of this alloy by the heavy plastic deformation.

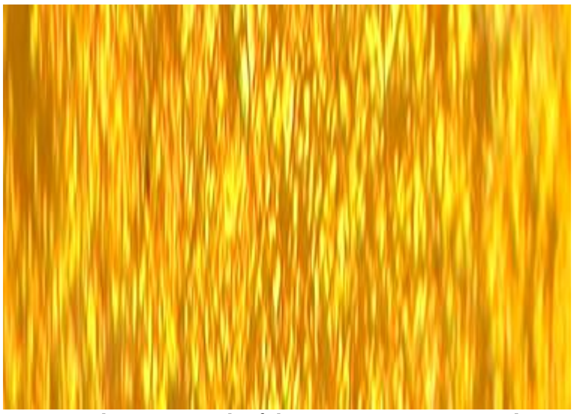

Figure 7: Photomicrograph of the microstructure Cu-Zn-Al SMA after direct extrusion, at magnification of 500X.

3.2. Effect of direct extrusion on the microhardness of Cu-Zn-Al SMA:

It is obvious from the histogram of Fig. 8 that the Vicker's microhardness of the Cu-Zn-Al SMA was greatly increased after the direct extrusion process where 105.2 % increase was achieved which is attributed to the heavy plastic deformation and the pronounced decrease in the grain size after extrusion process.

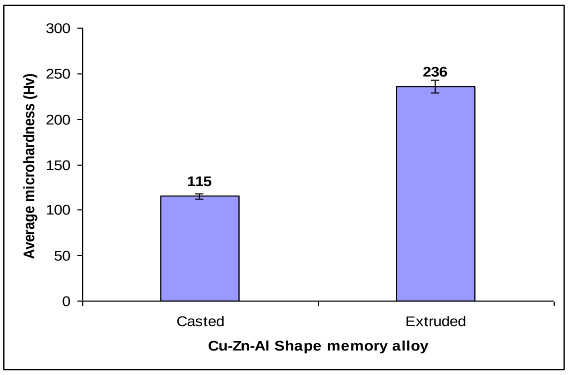

Figure 8: Average microhardness in the as cast and after extrusion conditions of Cu-Zn-Al shape memory alloy.

3.3. Effect of direct extrusion on the mechanical characteristics:

Fig.9 gives the mechanical behavior of Cu-Zn-Al SMA in the as cast and after extrusion presented by true stress-true strain curve as obtained from the autographic record of the compression test of the specimens test from the Cu-Zn-Al SMA before and after extrusion, Fig. 10(a) and (b). It can explicitly be seen from Fig.9 that the mechanical behavior is greatly enhanced by the extrusion process where about 100 % increase was achieved in the flow stress (from 200 MPa to 400 MPa). This is mainly attributed to heavy plastic deformation and the reduction in the grain size mentioned in the previous section.

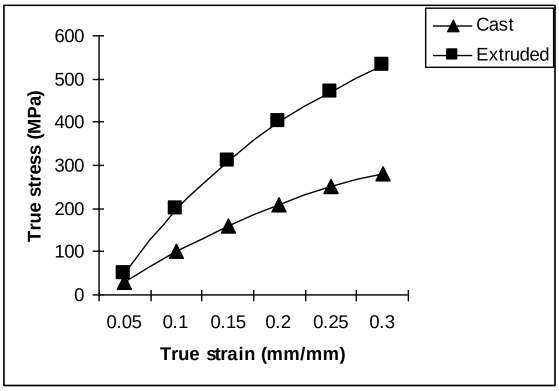

Figure 9: True stress-true strain of the as cast and after extrusion Conditions of Cu-Zn-Al shape memory alloy.

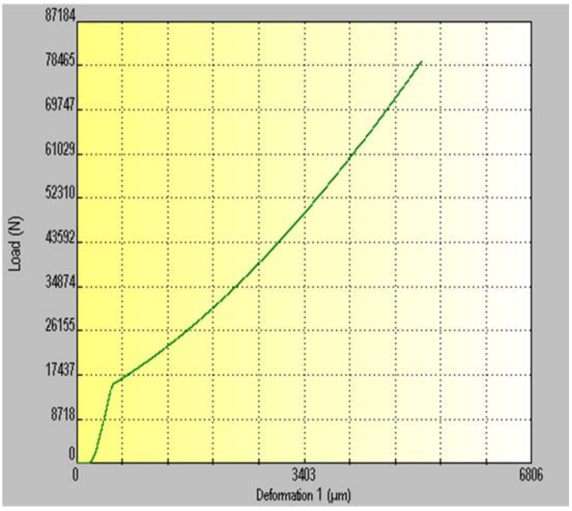

(a) In the as cast condition

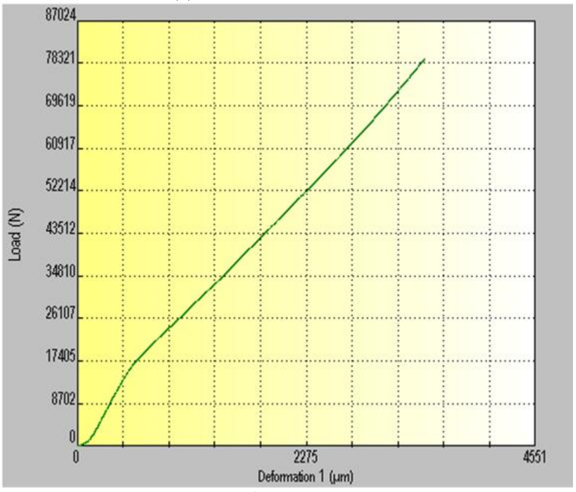

(b) After extrusion

Figure 10: Autographic records (punch-displacement) for compression test on specimens (a) in the as cast condition and (b) after extrusion test.

It is also worth noting from Fig.11 that the extrusion force is 29.84 KN at the extrusion ratio 1.44 in this experimental compared to 24.54 KN , the theoretical value as obtained from theoretical analysis shown in appendix 1. The difference which is 21 % is attributed to friction and redundant forces encountered in the extrusion process.

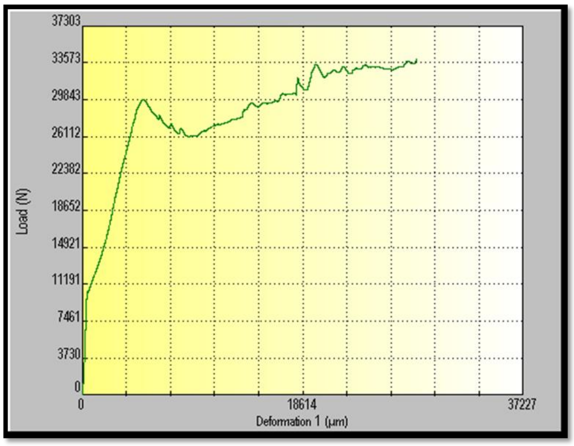

Figure 11: Plunger (force-displacement) of Cu-Zn-Al shape memory alloy.

3.4. Effect of direct extrusion on the surface roughness of Cu-Zn-Al SMA:

It can be seen from Fig.12 that there is a pronounced enhancement in the surface quality of Cu-Zn-Al shape memory alloy after extrusion, represented by 81.8 % reduction in surface roughness, Ra, was achieved.

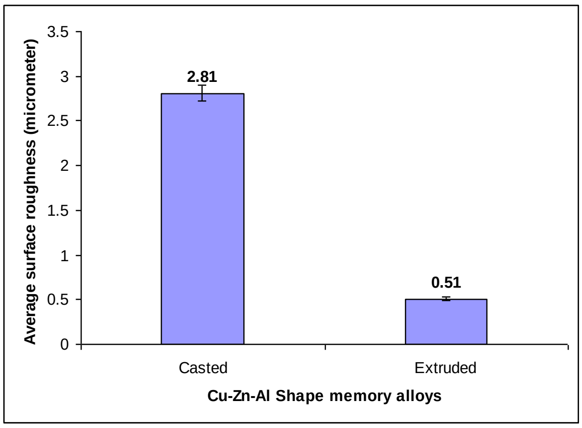

Figure 12: Average surface roughness Ra of the as cast and after extrusion Conditions of Cu-Zn-Al shape memory alloy.

4. Conclusions

The following points can be concluded:

- The average grain size of Cu-Zn-Al SMA was reduced by 46.2 % after direct extrusion process.
- There is a pronounced enhancement in the mechanical characteristics of Cu-Zn-Al shape memory alloy after forward extrusion; where the flow stress was increased by about 100 % at 0.2 strain.
- An enhancement of 105.2% was achieved in Vicker's microhardness of Cu-Zn-Al SMA after the direct extrusion process.
- The surface roughness of Cu-Zn-Al SMA was enhanced by 81. 8 % after direct extrusion process.

Acknowledgment

This work has been supported by King Abdullah II Fund for Development (KAFD) and King Abdullah II Design and Development Bureau (KADDB) which are acknowledged under grant number (8/2011). Author also would like to thank Eng. Emad Yard for his help and support, author also thank students Husam Mohammad, Mohammad Zaid, and Mohamad atah for their help in the experimental work.

References

[1] www.elsevier.com:locate:msea,journal of alloys and compounds 448(2008) 331-335, Effects of Gd addition on micro structure and shape memory effect of Cu-Zn-Al alloy, available online 18 January 2007.

[2] K. Worden, W.A Bullough, J. Haywood "Smart technologies", World Scientific 2003, 109–135.

[3] http://www.talkingelectronics.com/projects/Nitinol/images (7/6/2011).

[4] http://webdocs.cs.ualberta.ca/~database/MEMS/sma_mems/sma.html ((7/6/2011).

[5] "Shape-Memory Alloys – Metallurgical Solution Looking for a Problem", Metallurgia, Vol. 51, No. 1, January 1984, 26–29.

[6] D. E. Hodgson "Shape Memory Applications", Inc., Wu M. H., Memory Technologies, and Biermann R. J., Harrison Alloys,lnc.,http://web.archive.org/web/20030605085042/http://www.smainc.com/SMAPaper.html.

[7] Kiyohide Wada and Yong Liu, "Shape recovery of NiTi shape memory alloy under various pre-strain and constraint conditions". Smart Mater. Struct, Vol.14 2005, S273–S286.

[8] Antonio Vitiello, Giuseppe Giorleo and Renata Erica Morace, "Analysis of thermomechanical behaviour of Nitinol wires with high strain rates". Smart Mater. Struct. Vol.14, 2005, 215–221.

[9] Z.G. Wang, X.T. Zu, X.D. Feng, L.B. Lin, S. Zhu, L.P. You and, L.M. Wang, "Design of TiNi alloy two-way shape memory coil extension spring". Science and Technology of Advanced Materials, Vol. 6, 2005, 889–894.

[10] Z.G. Wang, X.T. Zu, X.D. Feng, S. Zhu, J.W. Bao and, L.M. Wang, "Characteristics of two-way shape memory TiNi springs driven by electrical current". Materials and Design, Vol. 25, 2004, 699–703.

[11] J. Rena, K.M. Liewa "Meshfree modelling and characterization of the mechanical behaviour of NiTi alloys". Engineering Analysis with Boundary Elements, Vol., 29,2005, 29–40.

[12] Mikell P.Groover. Fundamentals of modern manufacturing process and system. 3rd ed, ml, 416-430.

Appendix 1: Extrusion Calculations

In general: Force = stress * cross sectional area.

$$F_{max} = P_i * A_o \quad (1)$$

The billet dimension used is 12 mm diameter and the output diameter is 10 mm; the stress in equation (1) is the maximum of the material to be extruded.

The extrusion pressure is estimated from the Johnson equation [12].

$$P_i = Y_{extruded} (a + b \, Ln \, R) \quad (2)$$

Where;

F_{max}	:	Maximum extrusion force.
p_i	:	Extrusion Pressure or internal pressure.
$Y_{extruded}$	:	Yield stress of the extruded material.
R	:	Equal to A_o/A_f.
R	:	(Extrusion Ratio) = 1.44
A_o	:	Initial cross-sectional area of the billet.
A_f	:	Final cross-sectional area of the extruded part.
a & b	:	Are constants for the material to be extruded.

$$p_i = 160*(0.8+1.5*(0.3646)) = 215.504 MPa$$

$$F_{\max} = p_i * A_0 = 215.504*(\frac{\pi(12)^2}{4}) = 215.504*113.097 = 24.372 kN$$

Appendix 2: FEM Analysis

Licensed solidwork software is used in FEM investigation for punch, die, and extruded part.

1. Punch

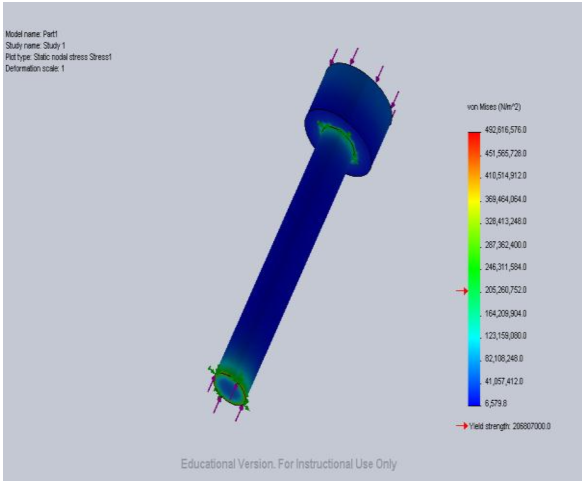

Figure A-1: Part1-Study 1-Stress-Stress.

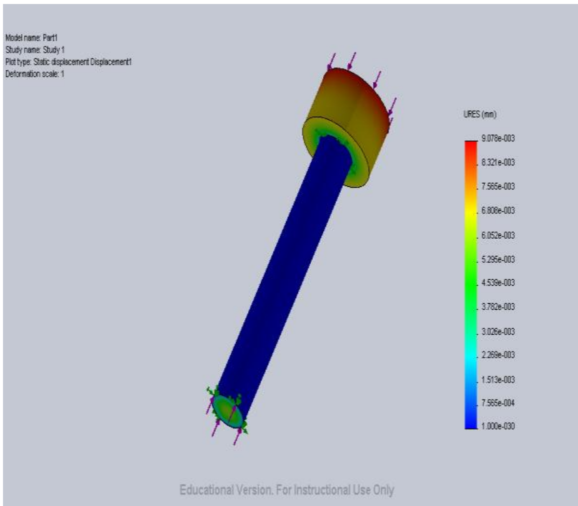

Figure A-2: Part1-Study 1-Displacement-Displacement.

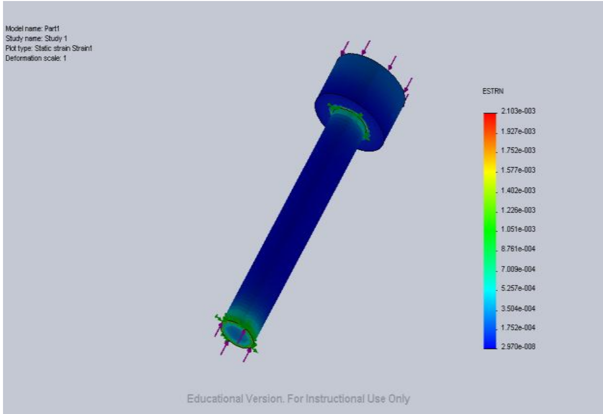

Figure A-3: Part1-Study 1-Strain-Strain.

2. Extruded work part

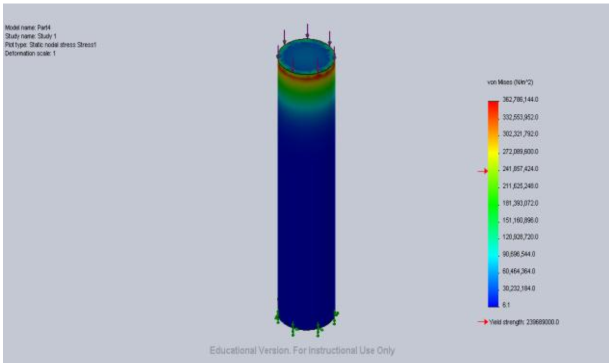

Figure A-4: Part4-Study 1-Stress-Stress.

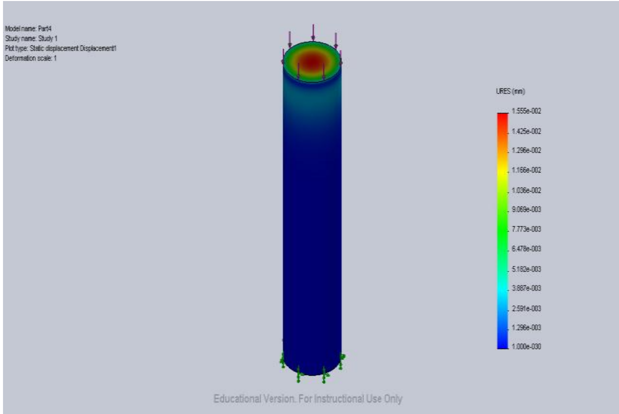

Figure A-5: Part4-Study 1-Displacement-Displacement.

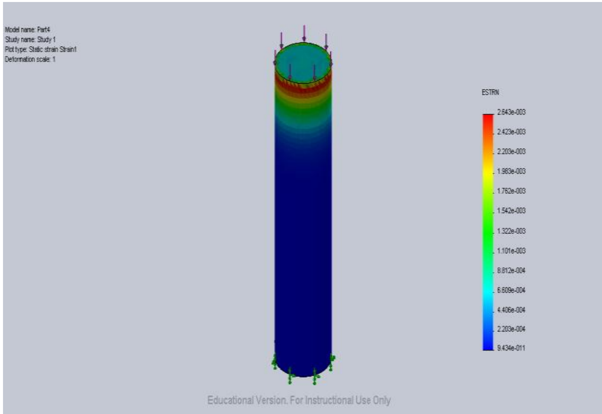

Figure A-6: Part4-Study 1-Strain-Strain.

JJMIE

Volume 6, Number 2, April 2012
ISSN 1995-6665
Pages 183 - 191

Jordan Journal of Mechanical and Industrial Engineering

Design Analysis and Modeling of a General Aviation Aircraft

F. H. Darwish[a,] * , G. M. Atmeh[b], Z. F. Hasan[c]

[a]Aeronautical Engineering Dept., Faculty of Engineering, Jordan University of Science and Technology, Irbid 22110, Jordan
[b]Mechanical and Aerospace Engineering Dept., University of Texas at Arlington, Arlington, Texas
[c]Mechanical Engineering Dept., Texas A&M University, College Station, Texas

Abstract

In the present study, design analysis is performed to accurately estimate the gross take-off weight, define the external geometry, and size the wings and tail of a general aviation aircraft by using the performance parameters associated with a pre-defined mission profile and a set of design goals. Three-dimensional layout and projections of the design airplane are created using conic lofting-based software. The airplane configuration, the estimated weight, and the real time airplane equations of motion are then introduced to a simulation environment in Matlab to visualize the take-off, climb and cruise segments of the mission profile. The simulation has proven the adherence of the design analysis and its results to the design goals. In addition, finite element software package COMSOL is implemented to perform static stress analysis on the selected wing configuration when subjected to the generated aerodynamic loads to examine its structural reliability. The finite element results have shown that the selected wing configuration is a safe candidate for the present general aviation airplane implementation.

Keywords: Aircraft Design; Flight Simulation; Finite Element Analysis

Nomenclature

a	airfoil lift slope
A_b	boom area
A_n	Fourier coefficient
AR	aspect ratio
b	span
c	chord length
$\bar{c}$	mean aerodynamic chord
c_d	drag coefficient per unit span
c_{do}	zero-lift drag coefficient per unit span
c_l	lift coefficient per unit span
c_m	pitching moment coefficient per unit span
c_r	chord length at the root
c_t	chord length at the tip
C_{HT}	volume coefficient of the horizontal tail
C_{VT}	volume coefficient of the vertical tail
D'	drag force per unit span
$D_{f,max}$	maximum diameter of the fuselage
F	external force
g	constant of gravity
$I_{m,yy}$	mass moment of inertia around the y-axis
I_{xx}	second moment of area around the x-axis
I_{zz}	second moment of area around the z-axis
I_{xz}	product moment of area
k	induced drag coefficient
L'	lift force per unit span
L_f	length of the fuselage
L_{HT}	distance between the horizontal tail and the wing
L_{VT}	distance between the vertical tail and the wing
m	mass of the aircraft
M	pitching moment
M_x	bending moment around the x-axis
M_z	bending moment around the z-axis
P	power
q	shear flow
Q	pitching rate
S	plan form area of the wing
S_{HT}	plan form area of the horizontal tail
S_{VT}	plan form area of the vertical tail
S_x	shear force in the x-axis
S_z	shear force in the z-axis
u	linear velocity in the x-direction
V_∞	free stream velocity
w	linear velocity in the z-direction
W	instantaneous weight of the aircraft
W_c	weight of the crew
W_e	empty weight of the aircraft
W_f	weight of the fuel
W_o	gross take-off weight of the aircraft
W_p	weight of the payload
X_B	body x-axis
X_I	inertial x-axis
y	span-wise distance
Y	general y-axis
$\bar{Y}$	distance of the mean aerodynamic chord
Z_B	body z-axis
Z_I	inertial z-axis
a_O	zero-lift angle of attack
a_G	geometric angle of attack
F	fineness ratio
G	vortex strength
l	taper ratio
q	pitching angle
r	air density
s	direct stress
y	angle of twist

* Corresponding author. e-mail: fhdarwish@just.edu.jo

1. Introduction

The design of an aircraft is a prolonged process that consists mainly of three design phases which are: the conceptual design, the preliminary design, and the detailed design. The phase of conceptual design, which is the umbrella of the present research, deals mainly with developing a layout of the aircraft's external geometry, major systems and components; and determining the gross weight and the performance characteristics that the airplane must have in order to achieve its design goals.

The area of structural analysis and modeling of major aircraft components and its relevance to the conceptual design of aircrafts has attracted researchers and structural engineers in the aircraft industry. Giles [1] introduced a design-oriented analysis capability for aircraft fuselage structure. The new analysis capability and an existing wing analysis procedure were combined to model the entire airframe. Saha et al [2] presented a design analysis study of a hypothetical lightweight combat aircraft through thermodynamical, aerodynamical, and performance considerations of predefined mission requirements. The authors concluded that their design has fulfilled the numerous mandatory requirements demanded for an interceptor aircraft. A flexible approach for multidisciplinary design analysis and optimization, and its application to aircraft wing design was presented by Kesseler and Vankan [3]. Their results have shown significant improvements of the wing performance for different design goals which in turns approved the effectiveness and flexibility of the proposed approach. Tarkian and Zaldivar Tessier [4] introduced a frame work which enables a holistic view of the aircraft systems through a multidisciplinary analysis approach. The connection between the tools for aerodynamic analysis and CAD modeling were made fully automatic. This approach put the designers one-step closer to a non-statistical holistic approach for aircraft conceptual design. A detailed structural and stress analysis on an aerodynamically loaded Cessna aircraft wing were performed by Al-Mawahra and Zaza [5]. They investigated the structural effectiveness of the wing constructing components when subjected to the various aerodynamic loads.

The main objective of the present paper is to introduce an environment for a real time simulation of the aircraft motion based on the specifications of the flight mission profile; performance parameters, the geometry and the weight of the airplane to verify the adherence of the conceptual design geometric product to the initial deign requirements. In addition, the structural capability of the selected wing and sub components to withstand the generated aerodynamic loads is examined through finite element modeling and analysis using the finite element software package COMSOL [6].

2. The Conceptual Design

2.1. Design approach:

As described in reference [7], a set of design goals or requirements along with a flight mission profile must be available to provide a baseline for the conceptual design process. Initially, a crude method of weight estimation based on an initial sketch of how the airplane is envisioned is conducted to achieve an initial estimate of the weight of the airplane. This step is not linked to any other steps of the design procedure. It is basically performed to obtain an initial estimate of the airplane weight that can be used later for comparison with the final weight estimation to validate the results. In order to obtain an accurate estimate of the airplane weight, the performance parameters; wing loading (W/S), and the power-to-weight ratio (P/W) must be first calculated for each segment of the flight mission profile. Subsequently, the minimum wing loading and the maximum power-to-weight ratio are selected in order to satisfy the performance requirements of the entire fight and to be used later in the gross weight calculation. The major dimensions of the external geometry of the aircraft such as the fuselage length and diameter; the wing span and plan form area; and the tail specifications can be obtained by using of the selected performance parameters and the estimated weight as will be shown in the following sections. Finally, the method of conic lofting is used to generate a three-dimensional layout of the airplane by using the RDS software of reference [7].

2.2. Design goals:

The conceptual design is commenced by defining a set of design goals. Based on the existing data of many different general aviation airplanes, the design goals of the present airplane are set as follows:

- Single engine airplane with a maximum velocity > 76 m/s.
- Stall velocity = 18 m/s
- Take-off ground roll distance < 305 m
- Landing distance < 427 m
- Range = 1000 km
- Service ceiling = 3962 m
- Maximum rate of climb = 6 m/s

This set of design goals is considered as a baseline for the conceptual design process.

2.3. Mission profile and initial sketch:

A simple mission profile that consists of five segments which are the take-off, climb, cruise, loiter and landing is considered for the present design analysis and is shown in figure 1.

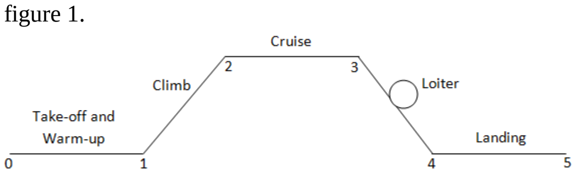

Figure 1: Mission profile.

Figure 2 shows the initial hand sketch of the aircraft. This basic sketch tentatively specifies the vertical location and geometry of the wings, the type and location of the tail, the landing gear, the engine and the cockpit locations.

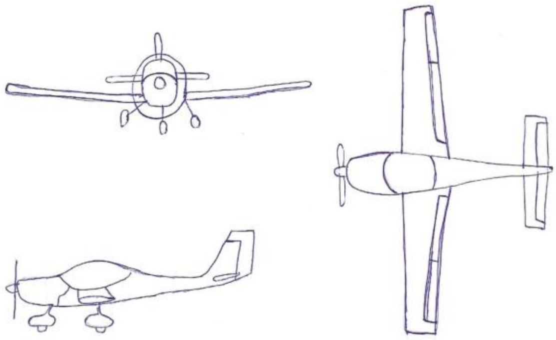

Figure 2: Initial sketch.

2.4. Weight estimation based on an initial sketch:

The airplane gross take-off weight is basically the sum of the weight of the crew, the weight of the payload, the weight of the fuel, and the empty weight of the airplane.

$$W_o = W_c + W_p + W_f + W_e \quad (1)$$

The terms of equation (1) are rearranged and the take-off gross weight is expressed in terms of the crew and payload weight; the fuel weight fraction and the empty weight fraction as in equation (2), [7].

$$W_o = \frac{W_c + W_p}{1 - (W_f/W_o) - (W_e/W_o)} \quad (2)$$

The crew and payload weights are normally prescribed in the design requirements. The fuel weight fraction primarily depends on the amounts of fuel burned during each segment of the mission profile or, in other words, on the weight fraction across each segment of the mission profile. The empty weight fraction however is unknown and is statistically a function of the take-off gross weight as in equation (3), [7].

$$\frac{W_e}{W_o} = AW_o^C \quad (3)$$

The parameters A and C in the above equation are statistical constants that depend on the shape of the airplane which is tentatively shown in the sketch of figure 2, and on the family of the airplane, for example, general aviation in the present study. Accordingly, the calculation of the gross weight through equation (2) is an iterative process that starts with an initial guess of the gross take-off weight. Based on this method, the crude estimate of the airplane gross weight is found to be 757.5 Kg. More details about the calculation of the fuel weight fraction and the empty weight fraction are provided in reference [7].

2.5. Weight estimation based on the performance parameters:

This method is more sophisticated than the one presented in the previous section and provides a better estimation of the gross weight of the airplane as the performance parameters are integrated in the gross weight equation. The difference between the two methods is basically in the calculation of the empty weight fraction. In this method the empty weight fraction is function of the wing loading, power-to-weight ratio, the wing aspect ratio (AR), the maximum cruising velocity, and the airplane gross weight as presented in equation (4), [7].

$$W_e/W_o = a + bW_o^{C1} AR^{C2} (W/S)^{C3} (P/W)^{C4} V_{max}^{C5} \quad (4)$$

Where a, b, C1, C2, C3, C4, and C5 are statistical constants that depend on the family of the airplane [7]. In the above equation, the wing loading and the power-to-weight ratio are the minimum and the maximum respectively, of all segments of the mission profile. Some equations that are used to calculate the wing loading and the power-to-weight ratio are mathematically interconnected which makes the analysis lengthy and complicated. In addition, some geometric and aerodynamic parameters such as the wing aspect ratio, taper ratio, airfoil type and characteristics, and the drag coefficient are needed for the analysis to prepare equation (4). These parameters are not prescribed in the design requirements but can be carefully selected to serve achieving the design goals. Table 1 lists all the selected parameters, their values, and the resulting minimum wing loading and maximum power-to-weight ratio.

Table 1: Minimum wing loading and maximum power-to-weight ratios along with the required geometric and aerodynamic parameters needed for their calculations.

Required Aerodynamic and Geometric Parameters	
Wing root airfoil	NACA 23018
Wing tip airfoil	NACA 23012
Wing maximum lift coefficient	2.34
Maximum lift-to-drag ratio	12.9
Oswald efficiency factor	0.8
Zero-lift drag coefficient	0.03
Taper ratio	0.5
Aspect ratio	8
Fuselage fineness ratio	5.5
Calculated Wing Loading and Power-to-Weight Ratio	
Minimum wing loading	78.1 Kg/m^2
Maximum power-to-weight ratio	0.15 hp/Kg

Now that the required performance parameters are available the gross-takeoff weight can be iteratively calculated by invoking equation (4) into equation (2). The converging solution of the gross weight of the airplane was found to be 952.5 Kg.

2.6. Geometry sizing:

The geometry of a trapezoidal wing can now be unveiled after having the gross weight of the airplane, the wing loading, the wing aspect ratio and taper ratio. The following equations can be used to calculate the wing plan form area, the wing span, the root chord, the tip chord, the length and the location of the aerodynamic chord respectively.

$$S = \frac{W_o}{(W/S)} \quad (5)$$

$$b = \sqrt{AR.S} \quad (6)$$

$$c_r = \frac{2S}{b(1+\lambda)} \tag{7}$$

$$c_t = c_r.\lambda \tag{8}$$

$$\bar{c} = \frac{(2/3)c_r(1+\lambda+\lambda^2)}{(1+\lambda)} \tag{9}$$

$$\bar{Y} = (b/6)\frac{(1+2\lambda)}{1+\lambda} \tag{10}$$

The fuselage main dimensions which are the length and maximum diameter can also be determined having available the airplane gross weight and the fineness ratio which represents the ratio between the fuselage length and maximum diameter. The length of the fuselage is related to the gross weight of the airplane and the statistical constants m and n as shown in equation (11), [7]. Subsequently, the maximum diameter can then be calculated from equation (12).

$$L_f = mW_o^n \tag{11}$$

$$\phi = \frac{L_f}{D_{f,\max}} \tag{12}$$

The results of equations 5 to 12 are presented in table 2.

Table 2: Wing and fuselage dimensions.

Wing area	12.2 m^2
Wing span	9.9 m
Wing root chord	1.65 m
Wing tip chord	0.8 m
Wing mean aerodynamic cord	1.3 m
Mean aerodynamic cord location along span	2.19 m
Fuselage length	7.7 m
Fuselage maximum diameter	1.4 m

The wing geometry and dimensions are shown in figure 3.

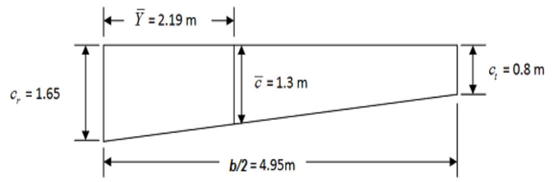

Figure 3: Wing geometry and dimensions.

The vertical and horizontal trapezoidal tails of the airplane are sized in a similar manner, however; depending on the volume coefficients of the vertical tail and the horizontal tail which express the effectiveness of the tail moments coefficients. Values of the horizontal and vertical tail coefficients vary according to the mission category of the aircraft [7]. The equations below allow for the calculation of the vertical and horizontal tail areas respectively.

$$S_{VT} = \frac{C_{VT}bS}{L_{VT}} \tag{13}$$

$$S_{HT} = \frac{C_{HT}\bar{c}S}{L_{HT}} \tag{14}$$

Accordingly, the plan form area, the span, the root and tip chords of the vertical and horizontal trapezoidal tails are found and summarized in table 3.

Table 3: Horizontal and vertical tails dimensions.

Horizontal Tail	
Span	3 m
Root cord	1 m
Tip cord	0.56 m
Mean aerodynamic cord	0.81 m
Mean aerodynamic cord location along span	0.68 m
Vertical Tail	
Span	1.2 m
Root cord	1.1 m
Tip cord	0.55 m
Mean aerodynamic cord	0.85 m
Mean aerodynamic cord location along span	0.27 m

2.7. Design layout:

As introduced, the main objective of the conceptual design is to provide lay-out drawings of the design airplane that feature its external geometry which has to be in general producible, aerodynamically smooth and credible. Conic lofting is a technique which incorporates a family of second degree curves to define the external geometry of airplanes and ships as well. In this study, the conic lofting technique is used to generate drawings of the designed airplane using the RDS software. Figures 4a and 4b show an isometric and three-view layout respectively of the airplane developed in RDS.

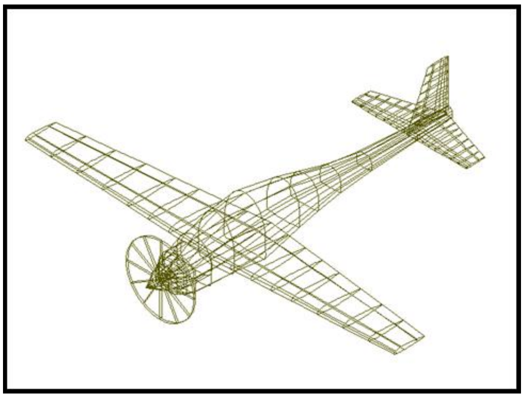

4a

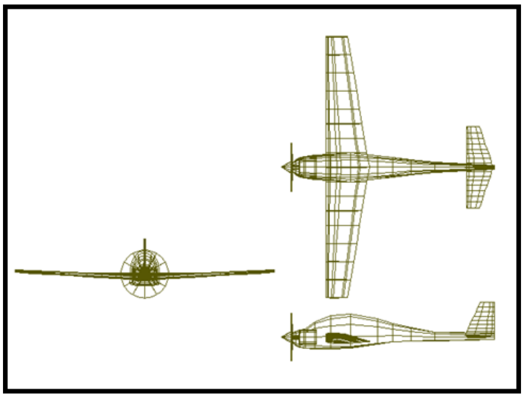

4b

Figure 4: a) Aircraft isometric layout, b) Aircraft three-view layout.

3. Takeoff Simulation

The next step after defining the external geometry of the airplane is to create a three-dimensional model using the V-realm Builder software [8] and place it in a simulation environment, as shown in figure 5, by incorporating Matlab's simulink [9].

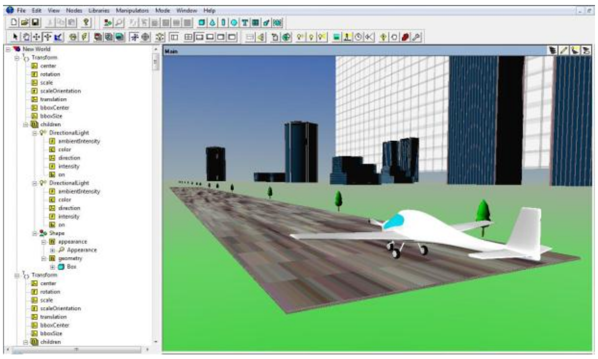

Figure 5: Simulation environment and three-dimensional model.

The intention of the simulation is to prove the ability of the design airplane to satisfy the predefined design goals. The simulation has considered three-degree-of-freedom motion of the airplane which includes the translation in the XI and ZI inertial directions and rotation in XI -ZI plane (perpendicular to the Y axis) as shown in figure 6. Equations 15, 16, and 17 represent the general governing equations of the airplane motion and are solved to obtain the displacement, velocity and acceleration in the body frame (XB -ZB) as functions of time.

$$\dot{u} = \frac{F_x}{m} - Qw - g\sin(\theta) \tag{15}$$

$$\dot{w} = \frac{F_z}{m} + Qu + g\cos(\theta) \tag{16}$$

$$\dot{Q} = \frac{M}{I_{m,yy}} \tag{17}$$

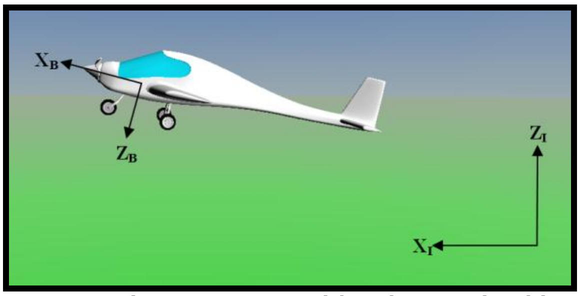

Figure 6: Simulation environment and three-dimensional model.

The solution of the governing equations was fed into the simulation environment instantaneously to simulate the airplane motion. The simulation started with the aircraft at rest on the runway, full thrust was applied and at a speed equal to $1.1V_{stall}$ the airplane was rotated to start climbing. It was observed that the simulation results, based on the designed aircraft parameters, were in full agreement with the design goals; for example, the ground roll was less than 300 m and the rate of climb was about 3 m/s. In general, the simulation results illustrated the design ability to meet the design requirements.

4. Wing Stress Analysis and Design

Structural analysis of the airplane wing is conducted to define the geometry of the wing spars and skin. The wing section is designed to have two spars, one at a quarter of the chord position and one at the three quarters of the chord. Angled spar flanges are used along with stringers to stiffen the skin. It is assumed that the stringers and spar flanges only carry the direct normal stresses while the skin and spar webs carry the shear stresses; this enables the idealization of the stringers and flanges areas into a concentrated area named booms to carry the direct normal stresses along with the thin skin to carry the shear stresses. Proper stress analysis is used to calculate the area of the booms and the thickness of the skin. The finite element software COMSOL is utilized to verify the results of the structural analysis by employing the finite element method to calculate the stresses in the wing due to the aerodynamic loading. A wing-local coordinate system shown in figure 7 is adopted for the structural analysis.

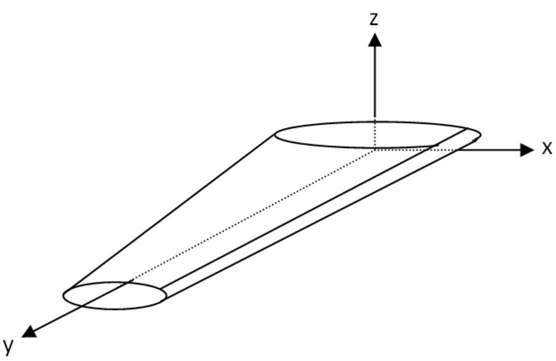

Figure 7: Wing-local coordinate system.

4.1. Aerodynamic loads and pitching moment:

The aerodynamic forces that affect aircraft wings are the lift and drag. In the present study the lifting line theory is applied to achieve the span wise load distributions on the wing. A code written in MATLAB is developed in order to generate the span-wise load distribution.

First the unknown vortex strength distribution is approximated by the following Fourier series expansion [5]:

$$\Gamma(\beta) = 2bV_\infty \sum_{n=1}^{N} A_n \sin(n\beta) \tag{18}$$

Where

$$\beta = \cos^{-1}\left(-\frac{2y}{b}\right) \tag{19}$$

and y is the location of any airfoil section along the span. In order to determine the Fourier coefficients An, the following lifting line equation is solved [5],

$$\frac{4b}{a(y)c(y)}\sum_{n=1}^{N} A_n \sin(n\beta) + \sum_{n=1}^{N} nA_n \frac{\sin(n\beta)}{\sin(\beta)} = \alpha_G(y) - \alpha_o(y) \tag{20}$$

By obtaining the Fourier coefficients, the airfoil lift coefficient at any span-wise location is calculated using the following equation:

$$c_l = \frac{(4b \times A_n \sin((2K-1)\times\beta))}{c(y)} \tag{21}$$

where K in the above equation is the number of sections along the wing considered in the analysis, and c(y) is the chord length at different sections and is shown in the following equation:

$$c(y) = c_r\left(1 - 2\frac{\lambda - 1}{b}y\right) = \frac{c_t}{\lambda}\left(1 - 2\frac{\lambda - 1}{b}y\right) \tag{22}$$

The drag coefficient is calculated from the drag polar equation.

$$c_d = c_{do} + kc_l^2 \tag{23}$$

The lift and drag forces are calculated at each span wise location by using equations 24 and 25. The lift and drag distributions along the span are shown in figures 8 and 9.

$$L' = \frac{1}{2}\rho V_\infty^{\ 2} c c_l \tag{24}$$

$$D' = \frac{1}{2}\rho V_\infty^{\ 2} c c_d \tag{25}$$

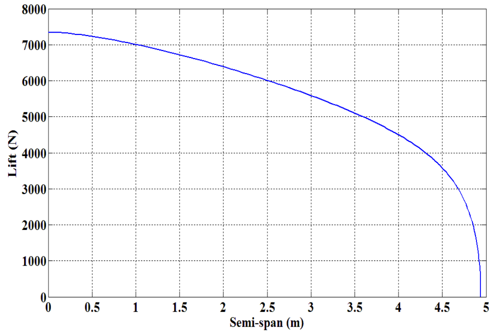

Figure 8: Lift distribution along the semi-span.

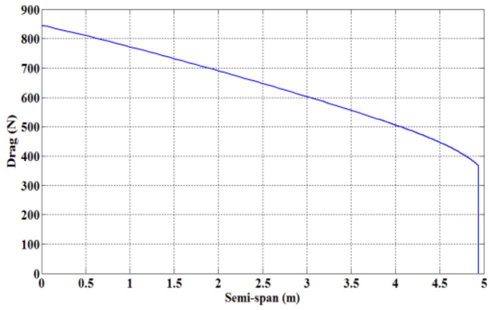

Figure 9: Drag distribution along the semi-span.

The pitching moment at each span-wise location is calculated by using the pitching moment coefficient and equation (26).

$$M = \frac{1}{2}\rho V_\infty^{\ 2} c^2 c_m \tag{26}$$

4.2. Shear force and bending moment distributions:

The presence of the lift and drag forces create two shear forces, S_x and S_z along with two bending moments, M_x and M_z. As shown in the section of the aerodynamic analysis the wing was divided into finite segments to obtain the aerodynamic forces, lift and drag. The corresponding shear forces are calculated by multiplying the force by the segment on which it is acting. The bending moments on the wing are calculated from the shear forces. The span-wise distribution of the shear forces and the moments are shown in figures 10-13.

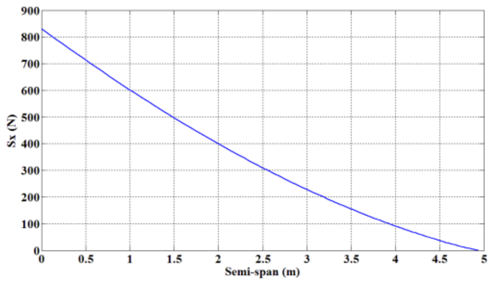

Figure 10: X-component shear stress distribution along the semi-span.

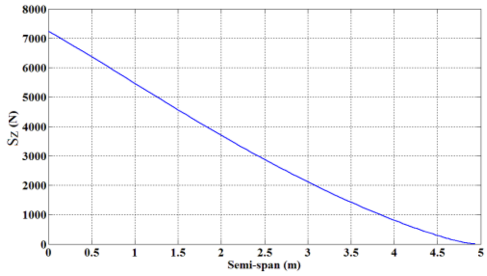

Figure 11: Z-component shear stress distribution along the semi-span.

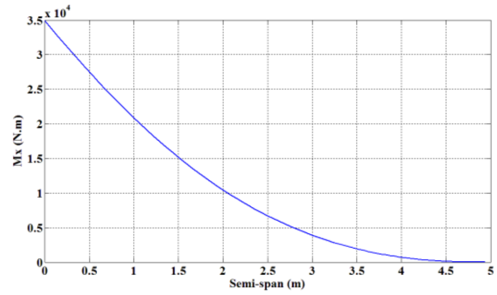

Figure 12: X-component bending moment distribution along the semi-span.

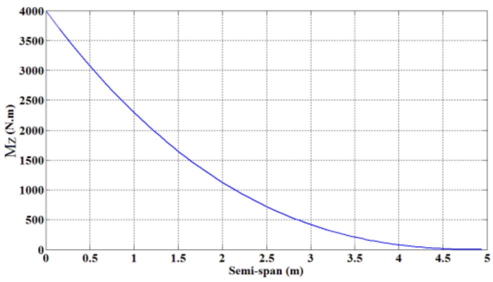

Figure 13: Z-component bending moment distribution along the semi-span.

4.3. Wing stress analysis:

As shown in figure 14, two idealized booms are placed at the quarter of the chord each having an area of A_b, and another two at three quarters of the chord each having an area of $0.8A_b$. The reason for a greater area at the quarter chord is due to the fact that the aerodynamic center is at that location requiring a larger area at that position. The following analysis calculates the area of the booms based on the bending stress analysis, and the thickness of the skin based on the shear flow in it, all at the root airfoil at which the loads are maximum.

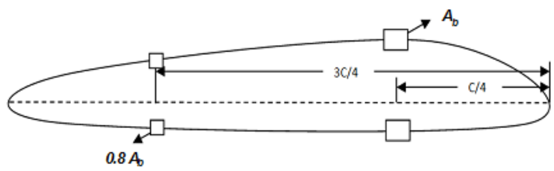

Figure 14: Schematic illustration of idealized booms and their location.

4.3.1. Boom area calculation:

The direct bending stresses are considered in the analysis to calculate the boom areas since the flanges of the spars and the stringers are the areas that carry the bending stresses. First the centroid location is found in order to calculate the second moments of area of the booms. Using equations (27-29), the areas of the booms, which are imbedded in the second moment of area, are calculated by substituting the yield strength of the annealed steel 4140 alloy, with a factor of safety of 1.25, into equation (27). The area, A_b, was found to be 0.0026 m^2.

$$\sigma_y = \frac{\overline{M}_x}{I_{xx}} z + \frac{\overline{M}_z}{I_{zz}} x \tag{27}$$

$$\frac{\overline{M}_x}{I_{xx}} = \frac{M_x I_{zz} - M_z I_{xz}}{I_{xx} I_{zz} - I_{xz}^2} \tag{28}$$

$$\frac{\overline{M}_z}{I_{zz}} = \frac{M_z I_{xx} - M_x I_{xz}}{I_{xx} I_{zz} - I_{xz}^2} \tag{29}$$

In equation (27), (x and z) represent the location of the boom areas with respect to the pre-determined location of the centroid of the airfoil.

4.3.2. Skin thickness calculation:

Calculating the skin thickness was done by determining the shear flow in it by utilizing the shear forces acting on the wing. The shear center was first determined by substituting a value of zero for S_x then for S_z in equations (30) and (31). The shear forces are assumed to act at the shear center of the span-wise sections of the wing [11].

$$\frac{\bar{S}_x}{I_z} = \frac{S_x I_{xx} - S_z I_{xz}}{I_{xx} I_{zz} - I_{xz}^2} \tag{30}$$

$$\frac{\bar{S}_z}{I_{xx}} = \frac{S_z I_{zz} - S_x I_{xz}}{I_{xx} I_{zz} - I_{xz}^2} \tag{31}$$

The shear flow is then calculated by using equation (32):

$$q = q_b + q_{s,o} \tag{32}$$

In which q is the total shear flow in a closed section, q_b is the basic shear flow of an equivalent open section with $q_{s,o}$ compensating for creating the open section. The open section is considered in order to simplify the determination of the shear flow. Having two spars in the wing creates a three-cell structure requiring three open sections. Accordingly, the shear flow of the open section q_b is calculated using equation (33).

$$q_b = -\left(\frac{S_x I_{xx} - S_z I_{xz}}{I_{xx} I_{zz} - I_{xz}^2}\right)\int_0^s tx ds - \left(\frac{S_z I_{zz} - S_x I_{xz}}{I_{xx} I_{zz} - I_{xz}^2}\right)\int_0^s tz ds \tag{33}$$

In which x and z are the coordinates within an airfoil section and s is the distance measured around the cross section. The value of $q_{s,o}$, which compensates for the cut in the closed structure, is calculated using equation (34) in which G is the modulus of rigidity; A_c is the area of each cell and $d\psi/dy$ is the gradient of twist.

$$\frac{d\psi}{dy} = \frac{1}{2A_c}\int \frac{q_{s,o}}{Gt}ds \qquad (34)$$

The three-cell structure requires three cuts, which produces three versions of equation 34. The value of $q_{s,o}$ for each cell is found by setting the rate of twist to zero at the shear center and solving the three equations simultaneously. The shear center is found by equating the summation of moments due to shear forces about the shear center to that produced from the shear flow. By determining the position of the shear center, the aero-loads are then applied at the aerodynamic center causing a rate of twist. The rate of twist for cells one and two form one equation and the rate of twist for cells two and three form another. Both equations have three variables q_1, q_2 and q_3 which are the shear flows of the three cells. Therefore, a third equation is required. Here, the relationship between the external torque generated by the lift and drag forces along with the pitching moment on the shear center and the shear flow can be used and is shown below [11],

$$T = \sum_{i=1}^{3} 2A_{ci}q_i \qquad (35)$$

Having the shear flow, the thickness of the skin of the wing can be computed by using equation (36) in which τ is the shear strength of the skin material. The thickness was found to be 0.5 mm.

$$q = t \times \tau \qquad (36)$$

5. Finite Element Implementation

In order to examine the designed wing and study its reliability, the commercial finite element software COMSOL was used in order to model and analyze the wing under the calculated aerodynamic loads. The aerodynamic loads are defined as load per unit area over the upper surface boundaries. The boundary condition was fixed at the root of the wing while the whole model is meshed as shown in figure 15. In order to verify that the proposed design is safe and reliable, the distortion energy theory was applied to ensure that Von Mises stress divided by a factor of safety of 1.25 does not exceed the yield strength of the material used in the wing structure [12]. The FE model for the wing is constructed of two steel spar flanges with square cross sections; the spar flanges do not show explicitly in the geometry because they are defined as beams on the edges of the spar webs. The skin is defined as a shell along with the spar webs. Based on the results of the analysis, it was found that the maximum Von Mises stress was 681 MPa. By comparing the obtained Von Mises stress divided by the factor of safety with the yield strength of steel AISI 4140 (655 MPa) [12], it can be stated that the designed wing can sustain the loads according to the distortion energy theory. Figure 16 shows the Von Mises stress distribution in the wing structure. A maximum deflection of 9.1 cm in the out of plane direction is inflicted on the wing due to the load as shown in figure 17.

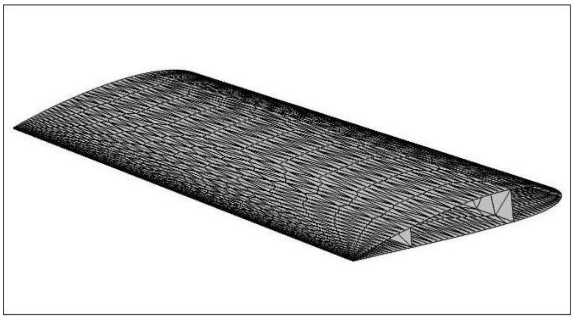

Figure 15: Wing model meshed using COMSOL commercial software.

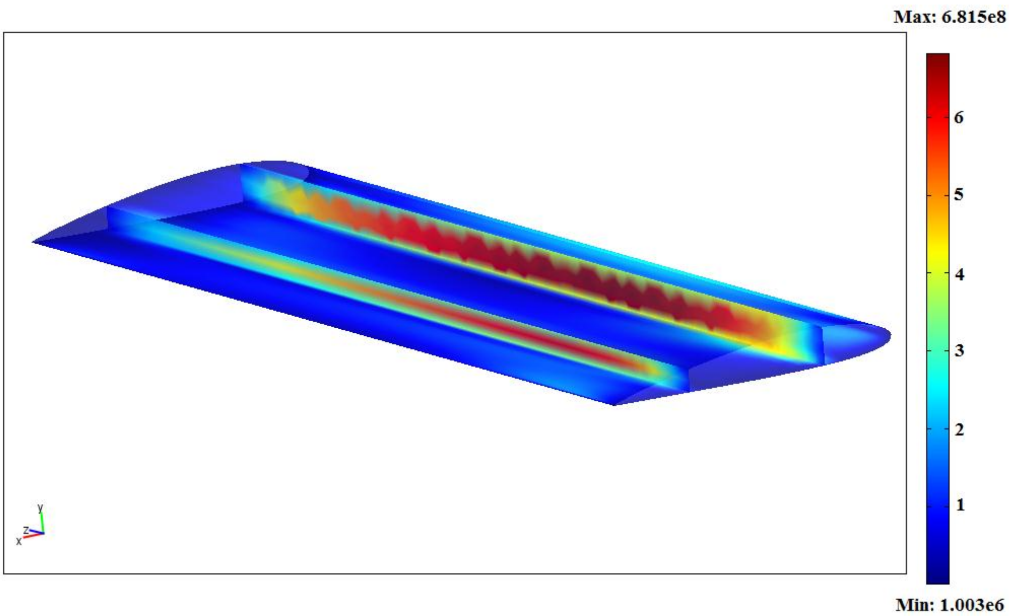

Figure 16: Von Mises stress distribution (Pa).

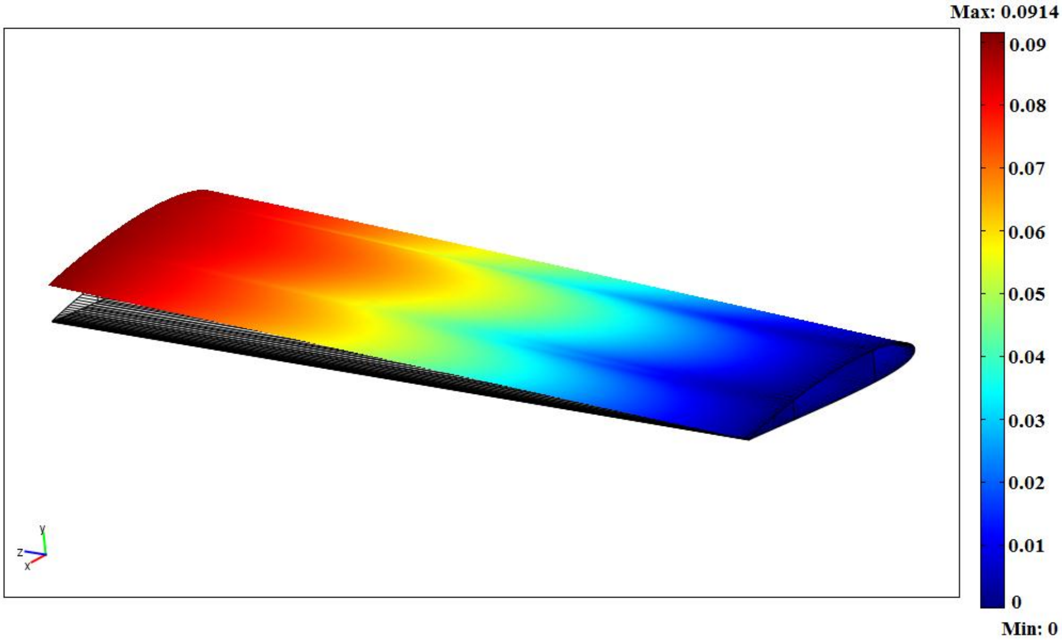

Figure 17: Wing deflection (m).

6. Conclusions

Conceptual design analysis of a general aviation aircraft was performed to estimate the gross take-off weight, the empty weight, the fuel weight and to size the major components of the aircraft based on a predefined set of design requirements. A design lay-out of the aircraft was also introduced by using conic lofting-based software. Subsequently, a simulation environment was created by using the Matlab Simulink to examine the performance of the designed aircraft during the take-off, climb, and cruise segments of the mission profile. The simulation has shown the adherence of the designed aircraft to the design requirements. The aerodynamic loads exerting on the wings and the resulting span-wise shear force and bending moment distributions were obtained. Structural analysis was performed on the selected wings to calculate the boom areas of the spars and the thickness of the skin that enable the wings to withstand the generated aerodynamic forces and moments. To examine the structural effectiveness of the designed wing, 3-D finite element analysis was performed using COMSOL metaphysics software to model the wings, to compute the critical stresses and to test the wings against Von Mises failure criterion. Based on the finite element results, it was found that the designed wing is a safe candidate for the airplane to perform its mission and to meet all the design requirements.

References

[1] Gary L. Giles, "Design –oriented analysis of aircraft fuselage structures", NASA technical document, AIAA-98-1749, 1998

[2] Saha, U K, Mitra, M, Menon, S J, John, N T, Gajapathi, S S, Behera, P, "Preliminary design analysis of a lightweight combat aircraft", Proceedings of the Institution of Mechanical Engineers, Part G, Journal of Aerospace Engineering, Vol. 222, No. 4, pp. 507-513, 2008.

[3] E. Kesseler and W.J. Vankan, "Multidisciplinary design analysis and multi-objective optimization applied to aircraft wing", National Aerospace Laboratory document, Netherland, 2006.

[4] Mehdi Tarkian and Francisco J. Zaldivar Tessier, "Aircraft parametric 3D modeling and panel code analysis for conceptual design", 26th International Congress of the Aeronautical Sciences, Alaska, USA, 2008.

[5] F., Al-Mawahra, O., Zaza, "Structural Analysis of an Aircraft Wing," Thesis submitted to the faculty of engineering, Jordan University of Science and Technology, June, 2009.

[6] COMSOL Multiphysics, COMSOL Inc.

[7] D.P., Raymer, Aircraft Design: A Conceptual Approach. American Institute of Aeronautics and Astronautics, Washington D.C, 1992.

[8] V – Realm Builder, version 2.0, Integrated Data Systems Inc., 1996.

[9] MATLAB, version 7.10.0.499 (R2010a), The MathWorks Inc., 2010.

[10] J.D., Anderson, Jr., Aircraft Performance and Design. McGraw-Hill, 1999.

[11] T.H.G., Megson, Aircraft Structures for Engineering Students", Elsevier Ltd, 2007.

[12] R.G., Budynas, J.K., Nissbett, Shigley's Mechanical Engineering Design, McGraw−Hill, 2008.

JJMIE

Volume 6, Number 2, April 2012
ISSN 1995-6665
Pages 193 - 198

Jordan Journal of Mechanical and Industrial Engineering

A Sharp-Interface Fluid-Structure Interaction Algorithm for Modeling Red Blood Cells

T. D. AlMomani*,[a], S. C. Vigmostad[b] and L. A. Alzube[a]

[a]Biomedical Engineering Department, The Hashemite University, P.O. Box 150459, Zarqa 13115, Jordan
[b]Biomedical Engineering Department, The University of Lowa, Iowa city, IA, USA 52242

Abstract

RBC deformation is thought to play a major role in both RBC dynamics and functionality. Due to the difficulty of experiments on real RBCs, researchers tend to perform computational simulations that can cover RBC dynamics and blood rheology. However, modeling of RBC with physiological conditions is still not completely well established. The current work utilized the immersed interface method and implements the fluid structure interaction technique to propose a new computational model of RBC as a biconcave fluid-filled cell. RBC is presented by a two dimensional hyperelastic massless membrane that surrounded by plasma and enclosed hemoglobin. The physiological viscosity ratio for the hemoglobin to that of plasma and their interactions with the cell membrane is considered. Pressure and velocity jump conditions are applied at the membrane, so that the influence of extracellular fluid can be transferred to the intracellular fluid. The model was applied to study the deformation of a single RBC as it flows in straight channels with geometries similar to that could find in capillaries with low Reynolds numbers that vary from 0.001 to 0.01. As Reynolds number increases, RBC shows higher levels of deformation. Flow fields through the cell membrane are appeared to be different and jumps in both velocity and pressure can be clearly seen.

Keywords: Red blood cell; Hyperelastic membrane; Jump conditions; Deformation; Capillaries

1. Introduction

The primary function of red blood cells (RBCs) or erythrocytes is delivering oxygen to different body organs and tissues. RBCs can be defined as nucleus-free deformable liquid capsules enclosed by a biological membrane that is nearly incompressible and exhibits a viscoelastic response to shearing and bending deformation [7]. Many researchers have described RBC as a capsule that consists of an elastic membrane that encloses a concentrated solution of hemoglobin [6]. RBCs are produced from bone marrow at a rate of 2 – 3 million cells per second, and have a lifespan of roughly 120 days. Adult humans have about 2–3 × 10^{13} red blood cells that circulate around their cardiovascular system. Hematocrit is defined as the volume percentage of RBCs in the whole blood; it's about 47% for adult men, and 43% for the adult women. RBCs have a distinctive biconcave shape, with 8μm diameter and 2 μm thickness. This shape gives RBCs a larger surface area, about 47% higher than a sphere of the same volume [3]. Additionally, this shape gives RBC the ability to exhibit high levels of deformation as it exposed to blood forces or flow in small diameter capillaries. Secomb 2003 has reported that RBCs can be folded and flow through a capillary with a diameter as small as 2.8 μm [17].

To date, many studies (both experimental and numerical) have been accomplished on RBC dynamics and their interaction with blood plasma, other blood constituents, vessel walls, and medical implants. The motivation of these studies would be among one of the following main reasons:

- At the microcirculatory level, the particulate nature of the RBC becomes important in determining blood properties and behavior, such as viscosity and non-Newtonian nature of the blood.
- Studying the biconcave shape of healthy RBCs helps in assessing cell membrane stress state .
- RBCs are proposed to have a major role in many cardiovascular diseases such as thrombosis (platelet activation) and atherosclerosis.

The small size, and high sensitivity to external conditions makes it difficult to perform *in vivo* experimentations on RBCs and other blood particles. Consequently, researchers tend to design experiments with single RBCs and employed simplified flow conditions [11]. Also due to these challenges, researchers took advantage of various numerical techniques to study the behavior of RBCs under different flow conditions and circumstances. They used different numerical methods such as finite element, immersed boundary, and boundary element techniques which can capture the deformation of

* Corresponding author. e-mail: thakir2000@hu.edu.jo

RBCs in different flow environments [11]. However, these numerical simulations have invoked significant assumptions in modeling the RBCs that are not physiologically correct [6].

Over the past few decades efforts to describe the micromechanics of the RBCs have led to several mathematical and computational models, the most popular RBC models are:

- Modeling RBCs as elliptical non-deformable particles [1].
- Modeling RBCs as elliptical deformable particles [10, 17].
- Modeling RBCs as fluid bubbles that resist flow by surface tension [25].
- Modeling RBCs as biconcave, assuming that the membrane is an elastic material that resists shearing, bending, or both [16].
- Modeling RBCs as biconcave, assuming that the membrane is a viscoelastic material that resists shearing and bending [4, 5].

The current work proposes a new model of the RBC as a biconcave, fluid-filled cell. This model considers a physiologically realistic viscosity ratio for the RBC intracellular fluid (primarily hemoglobin) to that of outer cellular fluid (or blood plasma) and the interactions with the cell membrane. Furthermore, RBCs are treated using an immersed interface approach similar to the one described in Lai and Li 2001 and Vigmostad et al. 2009 [12, 23].

The RBC membrane was modeled as a hyperelastic, massless membrane that separate two fluids, blood plasma outside and hemoglobin inside [2]. Membrane deformation was computed based on fluid forces on both sides of the membrane, where velocity and pressure jump conditions are imposed on the fluid based on the calculated membrane stresses.

2. Computational Approach

2.1. Governing Equation:

Continuity and momentum equations of incompressible flow with constant density were solved. The non-dimensionlized forms of these equations are given by:

$$\nabla \cdot \mathbf{u} = 0 \tag{1}$$

$$\frac{\partial \mathbf{u}}{\partial t} + \mathbf{u} \cdot \nabla \mathbf{u} = -\nabla p + \frac{1}{\mathrm{Re}} \nabla^2 \mathbf{u} + \mathbf{F} \tag{2}$$

Where $\mathrm{Re} = \rho_0 \mathbf{U}_0 D / \mu$, denotes the Reynolds number, **F** is a term that represent a singular force at the RBC membrane (this term will discuss later in details). The following variables are used as non-dimensionalzing groups:

$$\mathbf{u} = \frac{\mathbf{u}^*}{\mathbf{U}_0},\ L = \frac{L^*}{D_0},\ P = \frac{P^*}{\rho \mathbf{U}_0^2}$$

Where, **u** is the dimensional velocity field, $\mathbf{U}_0$ is the average axial velocity at the inlet, r_0 and m are the density and viscosity, and P^* is the dimensional pressure. The inlet gap width is denoted by D_0, and the characteristic pressure is $r_0 U_0^2$.

2.2. Flow solver and implicit representation of RBC:

The governing equations are discretized using a cell-centered collocated-variable semi-implicit approach. The solution is then advanced in time using the two-step fractional step method [24]. The embedded RBC is presented in the flow solver by using a sharp-interface method as used before in AlMomani et al 2008, Marella 2005, Marella and Udaykumar 2004 [1, 13, 14]. RBCs are represented implicitly on the mesh using a level-set approach [18, 19, 20]. The level-set (representing an embedded boundary – here an RBC) is represented by a scalar field denoted by ϕ_l, where l represents the l_{th} embedded interface or RBC. The normal distance from the l_{th} embedded interface at any point is representative of the value of ϕ_l. Values of ϕ_l less than zero (ϕ_l <0) represent the inside of the RBC, values of ϕ_l greater than zero (ϕ_l > 0) represent the outside of the RBC, the boundary (the membrane) of the RBC is presented by the zero ϕ_l values (i.e. ϕ_l = 0). Motion and deformation of the interface is computed based on the flow field and tracked using Lagrangian points describing the interface boundary, and employed to compute the RBC deformation.

2.3. Fluid structure interaction:

Fluid structure interaction (FSI) technique involves solving flow interacting with immersed structures. Generally, there are two FSI approaches that can be employed by the flow solver currently in use: The first approach is that in which the embedded object is treated as an immersed interface as described in Lai and Li 2001 and further outlined in Vigmostad et al. 2009 [12, 23]. Here, the assumption is that the surrounding is a massless membrane interface contributes singular stress fields [23]. In this approach the viscosity inside and outside of the membrane can be different, as is appropriate in the case of an RBC. The second approach is that which the embedded object is treated as a solid object that deforms as a result of the surrounding fluid forces. In this case, no-slip and no-penetration are used as boundary conditions on the solid surface [22]. The current work will utilize the first approach or FSI approach 1 to propose a new model of RBC as it expose to fluid forces.

2.3.1. Modeling of RBC using of FSI approach:

Here RBC is modeled as a hyperelastic massless membrane that separate two fluids, blood plasma outside and hemoglobin inside. The displacement and the deformation of this membrane are computed based on the fluid forces acting on this membrane as shown in Figure 1.

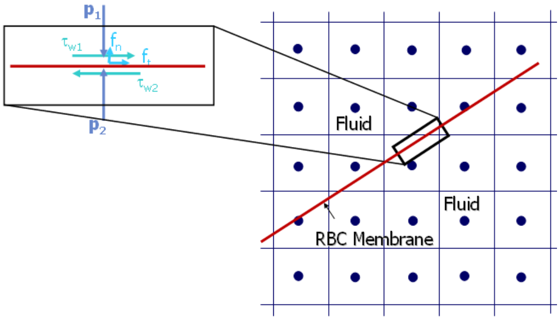

Figure 1: Force balance represented by a fluid-fluid interface separated by a membrane.

2.3.2. Approach to jump conditions using delta function:

Initially the singular force at the interface is presented by a delta function **f**, such that [12]:

$$\mathbf{f}(\mathbf{x},t)=\int_{\sigma}\mathbf{F}(r,s,t)\delta(\mathbf{x}-\mathbf{X}(r,s,t))drds \tag{3}$$

Where $\mathbf{f}(\mathbf{x},t)$ is the force density exerted by the membrane, and the membrane σ is represented by $\mathbf{X}(r,s,t)$ where *r*, *s* are parameters of a reference configuration where $0\le r\le L_r$ and $0\le s\le L_s$. The Dirac delta function is three-dimensional, and the membrane force, $\mathbf{F}(r,s,t)$ is a function of its configuration, where $\mathbf{F}(r,s,t)=\mathbf{S}(\mathbf{X}(r,s,t),t)$.

In other words, at any time, *t*, a region on the surface of the membrane is mapped onto a patch with area $L_r\times L_s$ and all calculations are performed in this reference space [22].

These calculations could also be performed in the current space, with $\mathbf{F}(\sigma,t)$ instead of mapping it back to a reference configuration. In this way, the above equation would change to:

$$\mathbf{f}(\mathbf{x},t)=\int_{\sigma}\mathbf{F}(l,m,t)\delta(\mathbf{x}-\mathbf{X}(\sigma,t))dldm \tag{4}$$

Where *l*, *m* are parameterized curves acting in the two *local* tangent directions, τ_1,τ_2. Consequently, by introducing the force f as a source term to the momentum equation, the governing equations of the fluid became as:

$$\nabla\cdot\mathbf{u}=0 \tag{5}$$

$$\frac{\partial\mathbf{u}}{\partial t}+\mathbf{u}\cdot\nabla\mathbf{u}=-\nabla p+\frac{1}{\mathrm{Re}}\nabla^2\mathbf{u}+\mathbf{f} \tag{6}$$

A summary of the jumps in pressure and velocities, and their derivatives, in the normal and two tangential directions are shown below:

- $[u]=[v]=[w]=0$ (from continuity/no-slip)
- $\left[u_x+v_y+w_z\right]=0$ (from incompressibility)
- $\left[\frac{\partial\mathbf{u}}{\partial\mathbf{n}}\right]\cdot\mathbf{n}=0$ (from incompressibility + continuity)
- $[\mathbf{u}_t]+[\nabla\mathbf{u}]\cdot\mathbf{u}=\mathbf{0}$ (from incompressibility)
- $[\nabla u\cdot\tau_1]=[\nabla v\cdot\tau_1]=[\nabla w\cdot\tau_1]=0$ (from continuity)
- $[\nabla u\cdot\tau_2]=[\nabla v\cdot\tau_2]=[\nabla w\cdot\tau_2]=0$ (from continuity)
- $[p]=[m]\frac{\partial\mathbf{u}}{\partial\mathbf{n}}\cdot\mathbf{n}+\mathbf{F}\cdot\mathbf{n}$
- $\left[\mu\frac{\partial\mathbf{u}}{\partial\mathbf{n}}\right]=[\mu]\left(\frac{\partial\hat{\mathbf{u}}}{\partial\mathbf{n}}\cdot\mathbf{n}\right)\mathbf{n}+(\mathbf{F}\cdot\mathbf{n})\mathbf{n}-\mathbf{F}$
- $\left[\frac{\partial p}{\partial\mathbf{n}}\right]=\frac{\partial}{\partial\boldsymbol{\tau}_1}\mathbf{F}\cdot\boldsymbol{\tau}_1+\frac{\partial}{\partial\boldsymbol{\tau}_2}\mathbf{F}\cdot\boldsymbol{\tau}_2$
- $\left[\frac{\partial p}{\partial\boldsymbol{\tau}_1}\right]=\frac{\partial}{\partial\boldsymbol{\tau}_1}\left([\mu]\left(\frac{\partial\hat{\mathbf{u}}}{\partial\mathbf{n}}\cdot\mathbf{n}\right)+(\mathbf{F}\cdot\mathbf{n})\right)$
- $\left[\frac{\partial p}{\partial\boldsymbol{\tau}_2}\right]=\frac{\partial}{\partial\boldsymbol{\tau}_2}\left([\mu]\left(\frac{\partial\hat{\mathbf{u}}}{\partial\mathbf{n}}\cdot\mathbf{n}\right)+(\mathbf{F}\cdot\mathbf{n})\right)$

Finally the FSI algorithm in approach 1 can be summarized in the following main steps:

For any new time step (n+1):

A. Compute the intermediate velocity, $\vec{\mathbf{u}}_f^{*n+1}$

B. Iterate until pressure and stress are converged, iteration (k+1):

- Solve for $p^{n+1,k+1}$
- Correct velocity, such that $\vec{u}_f^{\,n+1,k+1}$
- move interface, $\vec{u}_s^{\,n+1,k+1}=\vec{u}_f^{\,n+1,k+1}$
- compute interface stresses $\sigma^{n+1,k+1}$

3. Computational Results

The above algorithm has been applied to investigate the deformation of a single RBC as it flows in a microchannel with flow conditions similar to what can be found in capillaries. A straight tube with diameter of 12 µm (equivalent to 1.5 RBC major diameters) and length of 120 µm was used. Reynolds numbers of 0.001, 0.002, 0.004, and 0.01 were used in the current computations. Initially, the two dimensional (2D) unstressed biconcave shape of RBC, shown in Figure 2, is assumed. This shape is described by the following parametric equations [15]:

$$y=a\frac{\alpha}{2}(0.207+2.003\sin^2\chi-1.123\sin^4\chi)\cos\chi, \qquad x=a\alpha\sin \tag{10}$$

Where, a is the equivalent cell radius and equal to 2.8 µm, α = 1.38581894 is the ratio between the maximum radius of the biconcave disk (b in Figure 2), and the equivalent radius a, and finally, the parameter χ ranges from -π/2 to π/2.

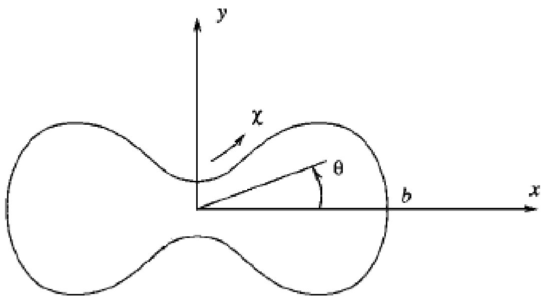

Figure 2: Biconcave shape of RBC.

3.1. Boundary and initial conditions:

At the inlet, the following parabolic velocity profile was used,

$$\mathbf{u}(y) = 4\mathbf{u}_{\max}(d_i y - y^2)/d_i^2 \tag{11}$$

Where u(y) is the velocity at y-location, u_{max} is the maximum inlet velocity, and di is the inlet diameter of the geometry. At the outlet, the velocities were linearly extrapolated and corrected to be consistent with global mass conservation and a Neumann condition was applied on the pressure [13, 14]. Finally, a no-slip (or wall) boundary condition was applied on the top and the bottom of the geometry.

3.2. Physiological assumptions:

In the current computations, the plasma (the external fluid) is assumed to behave as a Newtonian homogenous fluid, with a viscosity coefficient of 1.2 cP and the internal fluid is hemoglobin which was treated as a homogenous Newtonian fluid, as well, with a viscosity coefficient that is equivalent to five times the plasma viscosity (i.e. 6 cP). It is also assumed that only viscous and inertial forces affect the deformation of the RBC membrane and the effect of gravity is neglected. RBC is initially arranged in a vertical position in which the major axis of the RBC is parallel to the y-axis (90 degrees). The computations were performed for enough time so steady state of RBC deformation is reached as show in the result section.

3.3. Deformation of single RBC:

The biconcave shape of the RBC is initially assumed as stress free shape; i.e. the membrane is initially constructed such that no stresses and no strains can be found in this membrane. The fluid and membrane are fully coupled, so that the stress in the membrane affects the fluid as well as the fluid motion and forces affect the membrane behavior and deformation. Since the membrane moves with the fluid velocity, then no-slip is enforced at the interface implicitly. Membrane stress is computed assuming a hyperelastic material model as:

$$\boldsymbol{\sigma} = \mu\ (\mathbf{F}\mathbf{F}^T - \mathbf{I}) \tag{12}$$

Where, F is the deformation gradient, $\boldsymbol{\sigma}$ is the Cauchy stress, and μ is the Neo-Hookean elastic modulus, in the current computation a value of 0.005 dyn/cm is used [21].

The deformation profiles of a single RBC for Reynolds number values of 0.001, 0.002, 0.004, and 0.01 are presented in figure 3. The short axis of the RBC was coincided along the central axis of the capillary (or the straight tube). In all cases, RBC undergoes different levels of deformations. For Re = 0.001 (figure 3.a), RBC showed slight deformation and reached a steady state shape (starting at x = 5) allowing the deformed shape to be maintained as the RBC moves through the channel. Higher deformation levels are observed by increasing the Reynolds number (Figure 3: b, c, and d).

Finally, and for all Reynolds numbers, the RBC appeared to fold (with different degrees) in response to the fluid forces and reach the steady state shape while it moves with the fluid across the channel. As the Reynolds number increases (i.e. higher inertia forces), RBC folds more. In the case of Re =0.01, the steady state deformed shape of the RBC was more like a parachute shape.

3.4. Flow fields:

Figures 3 shows the velocity contours of flow at different time step for a Re = 0.001, Re = 0.002, Re = 0.004, and Re =0.01 respectively. This figure is also showing different deformation profiles of a single RBC as it exposed to a channel flow conditions, with flow values close enough or similar to the flow conditions that could find in the capillaries. RBC appeared to have major influence on both velocity and pressure fields. As can be observed in figure 4, that represent the pressure and velocity contours for deformed RBC with Re = 0.001, both velocity and pressure contours seem to jump at the area of the RBC membrane, also the pressure and velocity contours inside the RBC seem to be different form those out of the RBC. However, no discontinuity is observed between the two flow fields. This agrees with the idea of jump conditions which aims at transferring the influence of the outer fluid to the inner fluid through the RBC membrane without discontinuity. On the other hand, the differences between the two flow fields can be explained by the fact that these two fields have two different fluids with different viscosity values, which means that fluid forces are expected to be different in these two regions. Furthermore, the membrane of the RBC is expected to have a major contribution in the flow field through the membrane forces (or tension) that are applied to the fluids through the membrane forces or **F** term that imposed in the momentum equation.

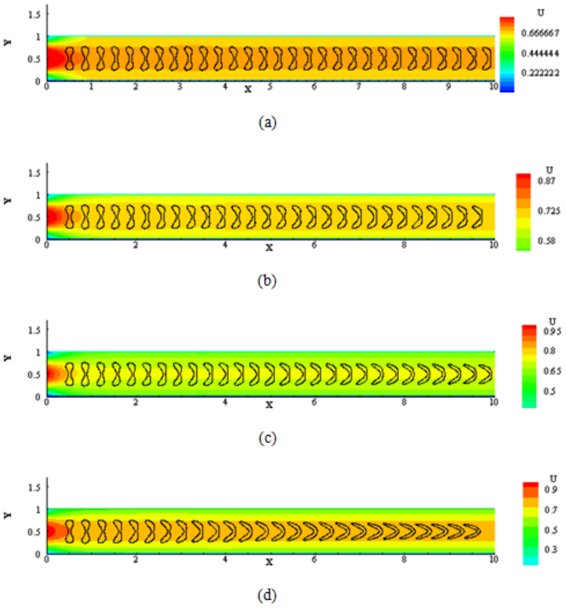

Figure 3: Velocity contours and the deformation profile of a single RBC as it flows through a straight channel with: a) Re = 0.001, b) Re = 0.002, c) Re = 0.004, d) Re = 0.01.

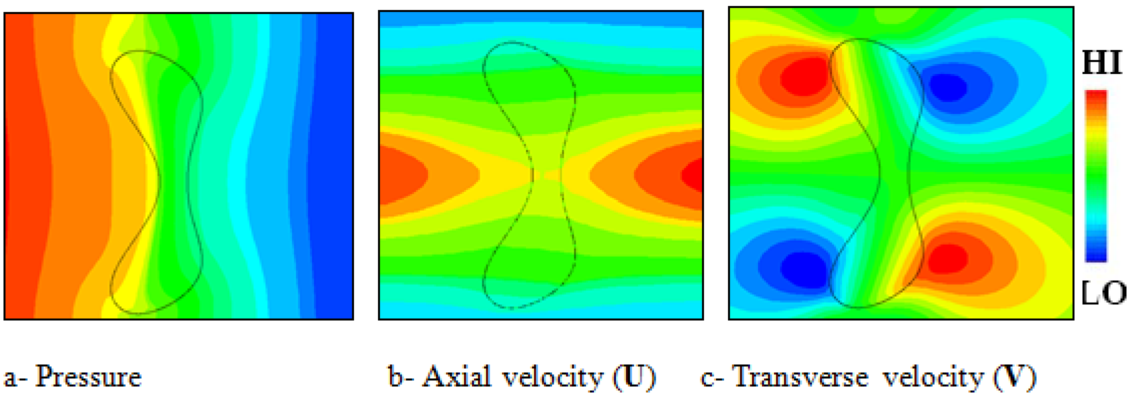

Figure 4: Pressure, axial velocity, and transverse velocity contours in the focused in the region surrounding a single RBC. Applied Reynolds number = 0.001.

4. Discussion and Conclusion

A fluid-structure interaction (FSI) algorithm has been developed and used to study the behavior of deformable RBC as it flow in a microchannel with dimensions similar to that could find in capillaries. In this algorithm, RBC was presented as a biconcave, hyperelastic, massless membrane that enclosed a Newtonian fluid (representing hemoglobin). Two-dimensional simulations are used to study the effect of intracellular and extracellular fluids on the cell membrane. Physiological viscosity values of plasma (or extracellular fluid) and hemoglobin (intracellular fluid) are used in the current computations. The membrane was modeled as a Neo-hookean elastic material that deform as a result of net fluid forces acting on the membrane from both inner and outer sides. Pressure and velocity jump conditions are applied to transfer the influence of the external fluid through the membrane to the internal fluid.

Reynolds number was defined based on the average axial flow velocity and using the diameter of the microchannel. At low Reynolds number of 0.001, RBC showed negligible deformation and it kept its un-deformed biconcave shape (Figure 3.a). This behavior changed as the Reynolds number increased resulting in higher levels of deformation. In all cases, RBC appeared to take a butterfly shape and fold more as the fluid inertia forces increases (higher Reynolds number) (Figure 3.b, c, and d). Furthermore, velocity and pressure contours were plotted to inspect the influence of the used jump conditions on both the extracellular and intracellular flows (Figure 4). Pressure and velocity contours seemed to change critically across the cell membrane. This change can be observed through the changes in the contour levels and gradients. Still, no discontinuity was observed between both sides of the membrane, which can be explained due to the use of proper pressure and velocity jump conditions. As mentioned earlier, the objective of using jump conditions is to transfer the influence and changes happening in the extracellular flow to the intercellular flow through the interaction and the deformation of the cell membrane. In the current approach, this goal has been achieved through the application of the membrane forces as a source term in the Navier-Stokes equations. This source term reflects the interaction between the elastic nature of the membrane itself and both intracellular and extracellular flow regimes.

In conclusion, this work proposed a new technique to simulate physiological behavior of RBC using simplified flow condition. The agreement between the results of the current study and those found in the previous experimental and numerical studies improve that the new approach can be easily expanded to more realistic physiological flow conditions. Computations handle larger numbers of RBCs in the same domain as well as higher Reynold's numbers are being currently investigated. These computations will include the interaction of deformable RBCs with other blood cells, artificial walls, and vessel walls. Furthermore, the current computations will be extended to involve 3D simulations of single and multi RBCs.

References

[1] AlMomani T, UdayKumar S H, Marshall J, Krishnan B C (2008) Micro-scale dynamics of erythrocytes-platelet interaction in blood flow. Annals of Biomedical Engineering 36 (6): 905-920.

[2] AlMomani T, Vigmostad S, UdayKumar S, Krishnan B C (2010) Modeling of red blood cell dynamics using fluid structure interface (FSI) technique. Proceedings of ASME 2010 Summer Bioengineering Conference. FL, USA, June, 2010.

[3] Chandran KB, Rittgers SE, Yoganathan AP (2007) Biofluid Mechanics: The Human Circulation. CRC/Taylor & Francis: Boca Raton, 2007; 419.

[4] Chang K S and Olbrecht W L (1993) Experimental studies of the deformation of a synthetic capsule in extensional flow. J. Fluid Mech. 250: 587-993.

[5] Chang K.S. and Olbrecht W L (1993) Experimental studies of the deformation and breakup of a synthetic capsule in steady and unsteady simple shear flow. J. Fluid Mech. 250: 609-1993.

[6] Cristini, V and Kassab G S (2005) Computer modeling of red blood cell rheology in the microcirculation: a brief overview. Annals of Biomedical Engineering. 33(12): 1724–1727.

[7] Eggleton, C D and Popel A S (1998) Large deformation of red blood cell ghosts in a simple shear flow. Phys. Fluids. 10: 1834–1845.

[8] Fishcer T M, Cees W M, Haest Stohr-Liesen M, and Schmid-schobein H (1981) The stress-free shape of the red blood cell membrane. Biophys. J. 34: 409 – 422.

[9] Gong X, Sugiyama K, Takagi S, and Matsumoto Y (2009) The Deformation Behavior of Multiple Red Blood Cells in a Capillary Vessel. J. of Biomechanical Engineering. 131: 074504-074511.

[10] Keller Stuart R and Skalak Richard (1982) Motion of a tank-treading ellipsoidal particle in a shear flow. J. Fluid Mech.. 120: 27-47.

[11] Korin N, Bransky A, and Uri Dinnar (2007) Theoretical model and experimental study of red blood cell (RBC) deformation in microchannels. Journal of Biomechanics. 40: 2088–2095.

[12] Lai, M C, and Li Z (2001) A Remark on Jump Conditions for the Three-Dimensional Navier-Stokes Equations Involving an Immersed Moving Membrane, Applied Mathematics Letters. 14: 149-154.

[13] Marella S, Krishnan S, Liu H, Udaykumar HS (2005) Sharp interface cartesian grid method I: an easily implemented technique for 3D moving boundary computations. Journal of Computational Physics. 210(1):1-31.

[14] Marella S., and Udaykumar H (2005) Computational analysis of the deformability of leukocytes modeled with viscous and elastic structural components. Phys. Fluids. 16: 244–264.

[15] Pozrikidis C (2003) Numerical simulation of the flow-induced deformation of red blood cells. Annals of Biomedical Engineering. 31: 1194–1205.

[16] Pozrikidis C (2001) Effect of membrane bending stiffness on the deformation of capsules in simple shear flow. J. Fluid Mech. 440: 269-291.

[17] Secomb T W (2003) Mechanics of red blood cells and blood flow in narrow tubes', In: C. Pozrikidis, ed. Modeling and Simulation of Capsules and Biological Cells. CRC Mathematical Biology and Medicine Series, Chapman & Hall, Boca Raton. 163–190.

[18] Sethian, J A (2001) Evolution, implementation, and application of levelset and fast marching methods for advancing fronts. J. Comp. Phys. 169:503–555.

[19] Sussman M. and Fatemi E (1999). An efficient, interface-preserving levelset redistancing algorithm and its applications to interface incompressible fluid flow. SIAM J. Sci. Comput. 20:1165–1191.

[20] Sussman M, Fatemi E, Smereka P, and Osher S (1998) An improved levelset methods for incompressible two-phase flows. Comput. Fluids. 27:663–680.

[21] Takagi S, Yamada T, Gong X, and Matsumoto Y (2009) The Deformation of a Vesicle in a Linear Shear Flow. Journal of Applied Mechanics. 76:021207

[22] Vigmostad S (2008) A sharp interface fluid-structure interaction model for bioprosthetic heart valve dynamics, University of Iowa, PhD thesis.

[23] Vigmostad S, Udaykumar S, Lu J, and Chandran K B (2009) Fluid–structure interaction methods in biological flows with special emphasis on heart valve dynamics. International Journal for Numerical Method in Biomedical Engineering, 26: 435 – 470.

[24] Zang Y, Street R L, and Koseff J R (1994) A non-staggered grid, fractional step method for time dependent incompressible Navier–Stokes equations in curvilinear coordinates. J. Comp. Phys. 114:18–33.

[25] Zhou H and Pozrikidis C (1995) Deformation of liquid capsules with incompressible interfaces in simple shear flow. Journal of Fluid Mechanics. 283: 175–200.

JJMIE

Volume 6, Number 2, April 2012
ISSN 1995-6665
Pages 199 - 203

Jordan Journal of Mechanical and Industrial Engineering

Cooling of Superheated Refrigerants Flowing Inside Mini and Micro Tubes, Study of Heat Transfer and Pressure Drop, CO_2 Case Study

A. ALShqirate[a], M. Hammad[b] and M. Tarawneh[c,*]

[a]Al-Balqa' Applied University, Alshoubak University College, Jordan
[b]Department of Mechanical Engineering, University of Jordan, Jordan
[c]Mechanical Engineering Department, The Hashemite University, Jordan

Abstract

Superheated Carbon dioxide gas was subjected to a cooling process. Experimental investigation along with an analytical study was carried out in this work. This work is intended to be part of the super critical Gustav Lorentzen refrigeration cycle of CO2. Experimental and analytical works concentrated on heat transfer and pressure drop for single phase flow during gas cooling inside mini and micro tubes. Empirical correlations were formulated analytically for the coefficient of convectional heat transfer and for the pressure drop in the following forms:

$Nu = 0.24\ (Re)^{0.53}\ (Pr)^{0.43}$

And

$Eu = 1.1*10^{-4}\ (ReD)^{-0.26}\ (L/D)^{1.06}$

Correlations were validated against some experimental results and compared to all experimental results and other literature correlations; an agreement of more than 90% was noticed. This work can enhance the calculations of heat flux and pressure drop of gases flow inside mini and micro tubes. It can also help in the design procedure of heat exchangers and cooling processes.

Keywords: Cooling refrigerants; Inside flow; Mini and micro tubes; Heat transfer; Pressure drop; R477

Nomenclature

Eu	Euler Number, (ΔP/ ρ V2)
ReD	Reynolds Number,(ρVD/μ)
L/D	length/diameter for tubes.
Pr	Prandtl number, (Cp μ/K)
Ra D	Ralighs number, (β g ΔT D3/υα)
T	Temperature, K or oC.
P	Pressure, kPa.
m	Mass flow rate, kg/s
h	Heat transfer coefficient, kJ/m2.k

Latin

Δ	Delta
ρ	Density, kg/m3
μ	Dynamic viscosity, m.s

Superscript

m,n	Exponents constants

Subscript

LMTD	Log. mean temperature difference
i	Inner
o	Outer

* Corresponding author. e-mail: mtar413@yahoo.com

1. Introduction

Heat transfer and fluid flow inside tubes have many applications. Heat exchangers, condensers, evaporators and boilers are examples of these applications. Literature shows many recent studies of heat transfer for single phase flow inside tube two of them are: Gopenath, [1] and Kim, [2].

Equations and correlations were formulated and validated by experimental work. Different correlations are now in use to calculate heat transfer coefficients and pressure drop. These correlations can be found in text books and papers of heat transfer, for example, Bejan [3], Incropera [4], and Liao [5].

The experimental and analytical work in this study covered a domain of independent parameters as follows; the inner tube diameter ranged from 0.6 mm up to 1.6 mm, the saturation temperature ranged from -15 ^{o}C up to 15 ^{o}C, the mass rate of flow ranged from 2.5 $*10^{-5}$ kg/s up to 17 $*\ 10^{-5}$ kg/s and the pressure ranged from 30 bars up to 50 bars.

Table 1 shows correlations for heat transfer Nu and pressure drop friction factor, *f*, during flow inside tubes. These are just examples of the published literature works, with all variables involved presented. These studies showed an acceptable agreement between experimental values of heat transfer coefficient and those calculated using the correlations predicted.

Table 1: Literature correlation formulae for single phase flow inside tubes.

No	Reference	Correlation	Case
1.	Incropera and Dewitt [2]	$Nu_D = 0.023 (Re_D)^{4/5} (Pr)^{1/3}$	Colburn equation.
		$f = (0.790 \ln Re_D - 1.64)^{-2}$ and $\Delta P/\Delta X = f\,(\rho V^2/2)/D$	Petukhov equation for pressure drop.
2.	Bejan [3]	$Nu_D = 0.027 (Re_D)^{4/5} (Pr)^{0.3}$	Cooling, Dittus-Boelter equation.
		$f = 0.079\, Re_D^{-0.25}$ and $\Delta P/\Delta X = f\,(\rho V^2/2)/D$	$2{*}10^3 < Re_D < 2{*}10^4$

2. Experimental

Figure 1 shows a schematic diagram of the used test apparatus. Cooling and condensation occurred inside a chest freezer with lowest possible air temperature of -28°C. The Data Acquisition System (DAS) of model SCX14, made by National Instruments was used with LAB VIEW software for processing. Visual and printed reports were the output of the experiments. Fifteen temperature readings were sensed by K – type thermocouples and fed to the DAS simultaneously.

The pressure was read in two points at steady state conditions and they were before cooling and at condensation. Volumetric rate of flow in m^3/s was read at the end outlet flow by a gas flow meter calibrated for CO_2 at room temperature and local pressure conditions.

1- Carbon dioxide gas cylinder, 2-Regulating valve, 3- Chest freezer, 4- Condenser, 5- Cut off valve, (4 units), 6- Pressure gauges, (3 units), 7- Sight glass, (2 units), 8- Evaporator, 9- Data Acquisition System, (DAS), 10- Volume flow meter.

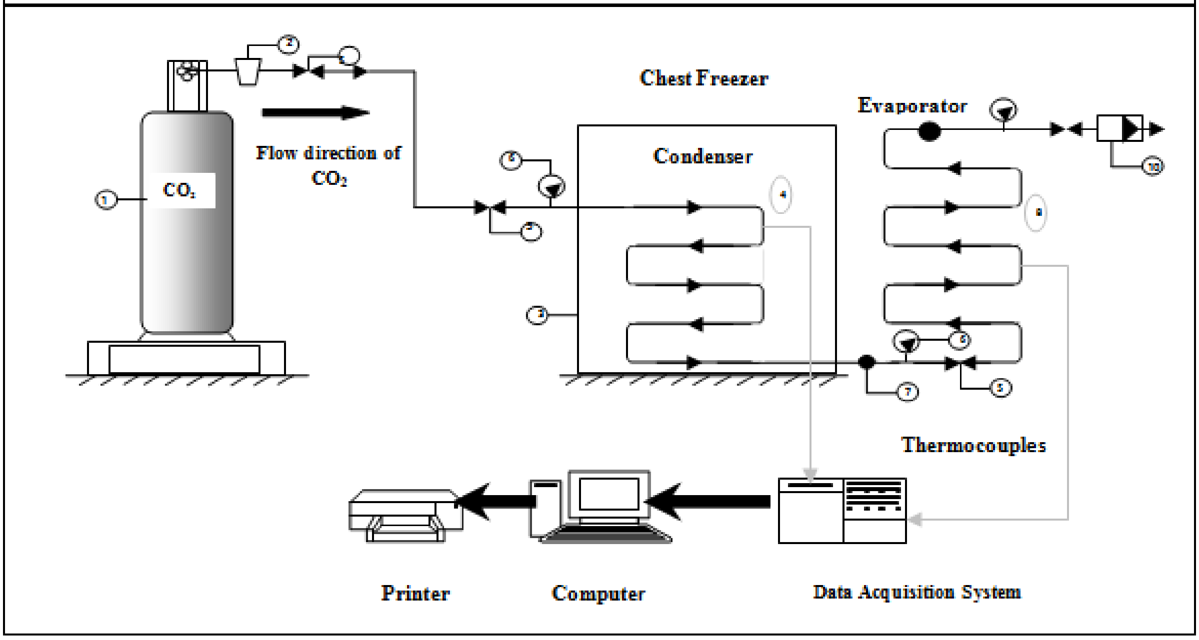

Figure1: Schematic diagram of the experimental unit.

2.1. Heat Transfer:

The tube outside surface temperatures at 15 points along the whole test sections (about 15 m), were measured by thermocouples fixed on the outer surface of the tube and covered with an insulation spot glue at longitudinal locations. These temperatures were tabulated along with the test section length. Two pressure values and volumetric rate of flow were tabulated also. Different experiments were carried out by changing independent variables; the pipe diameter, D, (three different values), test section inlet pressure, Pin, (four different values), and rate of flow, V, (four different values).

The total length of the cooling and condensation portion was about 15 meters. This study is concerned only with the first line which shows the process of cooling only.

Figure 2 shows the pipe longitudinal distribution of the tube outer surface temperatures of a typical cooling experiment. The figure shows a gas cooling part and a condensation part. The two lines are with different slopes.

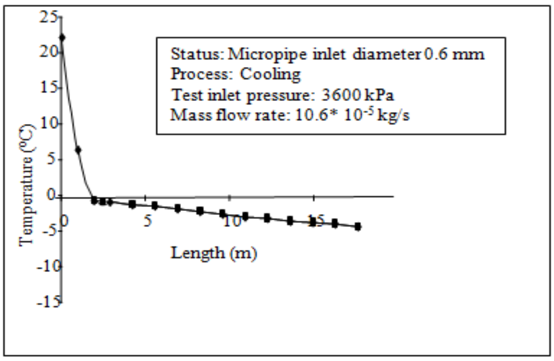

Figure 2: Tube outside wall surface temperatures measured points in °C versus test section length during cooling and condensation process inside the chest freezer of – 28 °C.

Heat released by the gas while cooling formed a radial heat flux. Convection and conduction heat transfer occurred. Heat balance for the heat transfer inside the chest freezer was modeled by the following equations:

$Q_{CO2} = h_o A_o \Delta T_{lmo}$ (1)

$Q_{CO2} = C_p (T_1^{/} - T_2^{/})$ (2)

$Q_{CO2} = h_i A_i \Delta T_{lmi}$ (3)

Where the outer logarithmic mean temperature difference equals:

$\Delta T_{lmo} = [(T_1 - T_a) - (T_2 - T_a)] / \ln [(T_1 - T_a) / (T_2 - T_a)]$ (4)

And the inner logarithmic mean temperature difference equals:

$\Delta T_{lmi} = [(T_1^{/} - T_1) - (T_2^{/} - T_2)] / \ln [(T_1^{/} - T_1) / (T_2^{/} - T_2)]$ (5)

Where T_1 and T_2 are the first and last temperatures of the wall outside surface, $T_1^{/}$ and $T_2^{/}$ are the gas inlet and outlet mean temperatures and T_a is the deep freezer air temperature around the tube.

Where, also A_o and A_i are the outer surface tube area and the inner surface tube area respectively.

The h_o and the h_i are the outer and inner heat transfer coefficient respectively.

Equation 1 will be used to calculate the heat quantity using Churchill and Chue formula to calculate h_o, the formula is [4]:

$Nu_D = \{0.60 + ((0.387 R_{aD}^{1/6}) / [1 + (0.559/P_r)^{9/16}]^{8/27})\}^2$ (6)

Equation 2 will be used to calculate the mean gas flow temperature at inlet, $(T_1^{/})$ as the gas temperature at exit is known to equal saturation temperature at measured pressure.

Then equation 3 will be used to calculate the mean heat transfer coefficient of CO_2 at the inner surface flow of the tube. In this step conduction heat transfer through the tube wall was neglected.

This will be the experimental heat transfer coefficient, (h_{exp}.) for cooling gaseous CO_2. This was calculated and abulated.

2.2. Pressure Drop:

To determine the pressure drop, it was convenient to work with the Moody (or Darcy) friction factor, which is a dimensionless parameter defined as [4]:

$$f = \frac{-(dP/dx)D_i}{\rho u_m^2 / 2} \quad (8)$$

Where, *f* is the friction factor, which can be either extracted from Moodies chart, or calculated using Petukhov equation as [4]:

$f = (0.790 \ln Re_D - 1.64)^{-2}$, $3000 < Re_D < 5*10^6$

(For turbulent flow) (9)

The length of the cooling region (L) was 1.9 meters as mentioned before.

Pressure drop, ΔP was calculated using equation 8 mentioned before and the value of *f* was extracted from Moodies chart. This data was tabulated and will be used later as experimental pressure drop values, $\Delta P_{exp.}$

2.3. Uncertainty Analysis for Experimental Work:

The uncertainty in the experimental calculated result is computed using the known Kline and McClintock following relation:

$$W_r = [(\frac{\partial R}{\partial X_1} W_{X1})^2 + (\frac{\partial R}{\partial X_2} W_{X2})^2 + ... + (\frac{\partial R}{\partial X_j} W_{Xj})^2]^{1/2} \quad (10)$$

Where: W_r is the uncertainty in the results; W_j is the uncertainty in each basic measurement, and the Partial derivatives $\frac{\partial R}{\partial X_j}$ are the sensitivities.

Calculations gave the following value:

$W h_{exp} = \pm$ 1.28 W/ m^2.K

This is less than 1%, of the original value.

And

$W \Delta P_{exp} = \pm$ 1.0 kPa.

This is around 6.5% of the original value.

3. Analytical Work

3.1. Convection Heat Transfer:

The Reynolds numbers of the experimental carried out in this work ranged from 3000 up to 15,000. Turbulent flow could be assumed and Colburn equation was used as a basic equation to calculate the convectional heat transfer coefficient. Colburn equation is in the form of Incropera, [4]:

$Nu_D = C\, Re_D^{m}\ Pr^{n}$ (11)

Where C is a constant, m and n are exponent constants.

Over the range of the Re_D and Pr values considered within this work domain, the values of the constants: C; m; and n were evaluated: 0.24; 0.53; and 0.43 respectively. The correlation for heat transfer relation between Nu_D, Re_D and Pr for CO_2 cooling super heated gas was formulated in the form:

$Nu_D = 0.24\, Re_D^{0.53}\, Pr^{0.43}$ (12)

3.2. Pressure Drop:

All references in the literature deal with pressure drop (ΔP) inside tube gas flow as a function of many variables shown in the following equation:

$\Delta P = f(Re_D, V, L, D, \rho)$ (13)

Analytical work manipulating equation 11 with non-dimensional terms revealed the following correlation in the form:

$$Eu = f\,(Re_D, L/D) \tag{14}$$

And this may be written as:

$$Eu = C\, Re_D^{\,m}\, (L/D)^{\,n} \tag{15}$$

The values of the constants: C; m; and n were evaluated: $1.1*10^{-4}$; -0.26 and 1.06 respectively. The pressure drop correlation for CO_2 can be put in the form:

$$Eu = 1.1 * 10^{-4}\, (Re_D)^{-0.26}\, (L/D)^{1.06} \tag{16}$$

4. Results Discussion

Figure 3 shows comparison between the experimental and correlation results of heat transfer coefficient, h_i. Two correlations were considered and each was compared with the experimental results: Colburn equation and this study correlation.

It is clear from the figure that h values of this work agrees with both the experimental results and those calculated using Colburn equation [4]. The agreement reached more than 0.98 with the experimental results and about 0.95 with Colburn results.

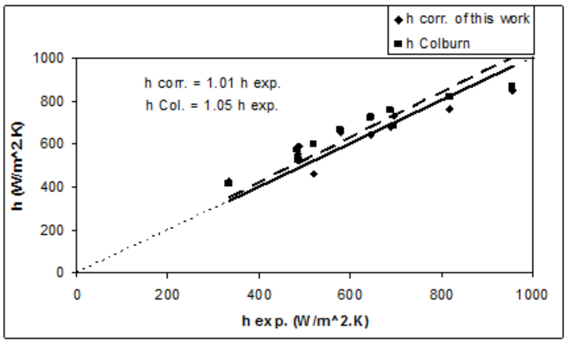

Figure 3: Experimental heat transfer coefficient Vs two correlation calculated values a) Using Colburn equation, b) Using this study correlation.

Figure 4 shows comparison between the experimental and correlation results of Nusselt number, Nu. Both Colburn equation and this study correlation were compared with the experimental results.

It is clear from the Figure that Nu values of this work agree with both the experimental results and those calculated using Colburn equation. The agreement of each one of the correlation with the experimental results reached about 0.92 for this study results and about 0.91 for Colburn results.

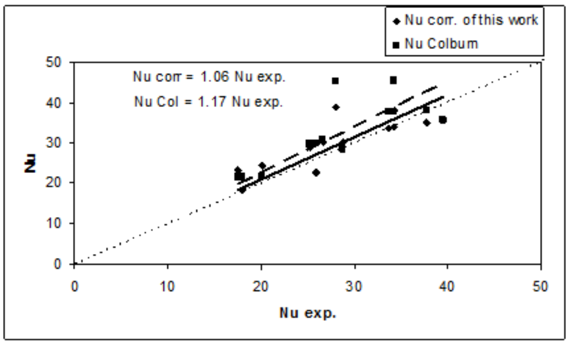

Figure 4: Experimental Nusselt number, Nu Vs two correlations calculated values a) Using Colburn equation, b) Using this study correlation.

Figure 5 represents comparison between experimental results of pressure drop, ΔP and that calculated using correlations. Two correlations were considered: Petukhov correlation [4] and this study correlation.

It is clear from the Figure that ΔP values of this study correlation agree with both the experimental results and those calculated using Petukhovs correlation. The agreement of each one of the correlation with the experimental results reached about 0.92 for this study results and about 0.91 for Colburn results.

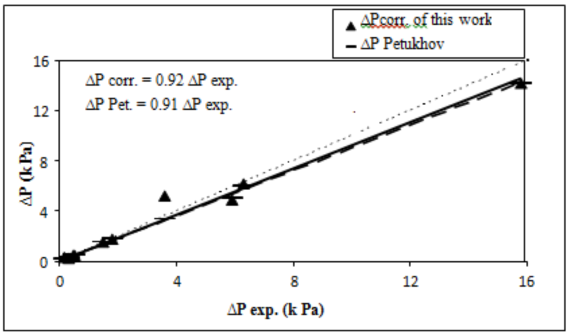

Figure 5: Experimental pressure drop, ΔP exp.Vs two correlation calculated values a) Using Petukhovs correlation, b) Using this work correlation.

Figure 6 represents comparison between experimental results of Euler number, Eu and that calculated for the correlations. Two correlations were considered: Petukhov correlation and this study correlation. Petukhov published a correlation for the friction factor, f, which relates f with Re. (equation 8), while this work formulated a correlation that connected Eu, ($\Delta P/\rho V^2$) to Re, and L/D, (equation 14).

It is clear from the Figure that Eu values of this study correlation agree with both the experimental results and those calculated using Petukhovs correlation. The agreement of each one of the correlation with the experimental results reached about 0.97 for this study results and about 0.94 for Colburn results.

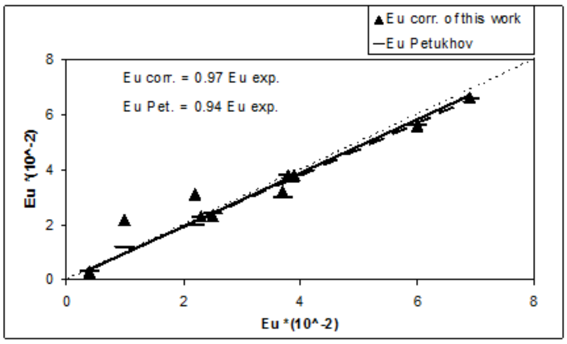

Figure 6: Experimental Euler number, Eu exp.Vs two correlation calculated values a) Using Petukhovs correlation, b) Using this work correlation.

5. Conclusions

- Simple and easy to use correlations were formulated in this study; one is related to the Nusselt number for convection heat transfer coefficient calculations. The other is related to Euler number for pressure drop calculations.
- For both h_{in} and Nu, the values of this work correlation agree with both the experimental results and those calculated using literature correlation of Colburn [4]. The agreement reaches around 0.94 with the experimental results and around 0.9 with Colburn results.
- The agreement of this work correlation in h_{in} is about 9% better than that of Colburn.
- For both ΔP and Eu, the values of this work correlation agree with both the experimental results and those calculated using Petukhovs correlation [4]. The agreement exceeds 95% in most cases.
- Petukhov correlation was for the friction factor, *f*, which relates *f* with Re. (equation 8), while this study formulated a correlation that connected Eu, ($\Delta P/\rho V^2$) to Re, and L/D, (equation 14), It is clear that this study correlation is in more agreement to the experimental results of at least 3%."
- Table 5 shows the resulting correlations for calculating heat transfer coefficient and pressure drop for single phase flow inside mini and micro tubes.

Table 5: The resulted correlations.

No.	conditions	General form, correlation	CO_2 correlation.
1-	Heat transfer	$Nu = C\, Re_D^{m}\, Pr^{n}$	$Nu = 0.24\, Re_D^{0.53}\, Pr^{0.43}$
2-	Pressure drop	$Eu = C\, (ReD^{m}\, (L/D)^{n}$	$Eu = 1.1 * 10^{-4}\, (Re_D)^{-0.26}\, (L/D)^{1.06}$

Acknowledgment

The authors would like to thank the University of Jordan for the support.

References

[1] Gopinath, R. Vijay K. and Leslie M., 2002, Heat transfer and pressure drop in narrow rectangular channels, J. experimental thermal and fluid science. 26, 53-64.

[2] Kim, M., Patterson, J., and Bullard, K., 2003 " Fundamental Process and System Design Issues in CO2 Vapour Compression Systems." Progress in energy and combustion science, 30, 119 – 174.

[3] Bejan A., 1993, " Heat transfer" J. Wiley.

[4] Incropera F., Dewitt D., Bergman T and Lavine A. 2007, Fundamentals of heat and mass transfer, 6th. Edition,J. Wiley.

[5] Liao S.M. and Zhao T.S. 2002. An experimental investigation of convection heat transfer to supercritical carbon dioxide in miniature tubes. International Journal of Heat and Mass Transfer, 45, 5025–5034.

المملكة الأردنية الهاشمية

الجامعة الهاشمية

المجلة الأردنية
للهندسة الميكانيكية والصناعية

JJMIE

مجلة علمية عالمية محكمة

http://jjmie.hu.edu.jo/

ISSN 1995-6665

المجلة الأردنية للهندسة الميكانيكية والصناعية

مجلة علمية عالمية محكمة

المجلة الأردنية للهندسة الميكانيكية والصناعية: مجلة علمية عالمية محكمة تصدر عن عمادة البحث العلمي و الدراسات العليا في الجامعة الهاشمية بالتعاون مع صندوق دعم البحث العلمي في الأردن.

ترسل البحوث إلى العنوان التالي:

رئيس تحرير المجلة الأردنية للهندسة الميكانيكية والصناعية

عمادة البحث العلمي والدراسات العليا

الجامعة الهاشمية

الزرقاء - الأردن

هاتف : 3903333 5 00962 فرعي 4147

Email: jjmie@hu.edu.jo

Website: www.jjmie.hu.edu.jo